Novel ZnO nanostructures: synthesis, growth mechanism, and applications.

By

Fokotsa Victor Molefe

(B.Sc. Hons)

This thesis is submitted in fulfillment of the requirements for the degree

Magister Scientiae (Nanoscience)

In the

Faculty of Natural and Agricultural Sciences

Department of Physics

Qwaqwa Campus

At the

University of the Free State

Promoter: Dr. L.F. Koao

Co – Promoters: Prof. B.F Dejene & Prof. H.C. Swart

05 December 2014

Dedications

In memory of my Uncle Malakoane Koena Joseph and Grandfather Molefe Letsa who left this world same day after encouraging me to pursue my studies to postgraduate level, I hope they are up there with God saying that's our son. I owe them and they would always live in my heart.

"To God Be the Glory"

Declaration – Plagiarism

I (Fokotsa Victor Molefe) declare that the thesis hereby submitted by me for the *Magister Scientiae* degree at the University of the Free State is my own independent work and has not previously been submitted by me at another university/faculty. I furthermore, cede copyright of the thesis in favor of the University of the Free State.

1. This thesis does not contain other person's data, pictures, graphs or other information.
2. This dissertation does not contain other person's writing, unless specially acknowledged as being sources from other researches.

   Where other written sources have been quoted, then:

(a) Their words have been rewritten but the general information attributed to them has been referenced.

(b) Where their exact words have been used, then their writing has been placed in italics and inside quotation marks, and referenced.

Acknowledgements

It was a great reward to be amongst several researchers who blessed my life in several ways and shaped my research aptitude. I am sending sincere gratitude to:

- Almighty **God** for life and wisdom he gave to me "For nothing is impossible with **God –** Luke 1:37".
- First of all, I would like to offer my sincerest gratitude and condolence to my late supervisor Dr Dolo J.J for welcoming me into the world of research.
- Big thanks to my supervisor Dr Koao L.F for his supervision, patience, knowledge, inspiration and great support during the period of my M.Sc studies.
- The good advice, support and friendship of Prof. Dejene B.F have been invaluable on both the academic and personal levels, for which I am extremely grateful.
- Prof. Swart for the opportunity to be part of his research group and introducing me into nanoscience program. His continuous support and encouragement in all matters of physics including personal dedication to the wellbeing and development of his students and research assistances.
- Special thanks go to my family (Mafokotsa, Dineo, Lehlohonolo, Qamo and Ntatemoholo Dingaka), words alone can never begin to express how grateful I am for all the sacrifices they made on my behalf and most importantly for their emotional and spiritual support which has helped sustain me throughout my career.
- Kentse kesa lebale motjhana waka **Dimpho**, one day you would understand why I have been away from you and family for a long period.
- National Research Foundation (NRF), Department of Science and Technology (DST) and the University of the Free State (UFS) for financial support. Furthermore I am grateful to the M.Sc nanoscience program in South Africa (NNPTTP) for collaboration research between UJ, UFS, UWC and NMMU.
- I would like to thank the cheerful and friendly staff members of Physics department UFS (Qwaqwa campus) - (Tshabalala K.G, Ocaya R.O, Motloung S.V and Motloung S.J.
- Nanophysics students who were good friends and made my M.Sc not only successful but also very enjoyable. Thank you! (Lotha T.L, Malevu T.D, Ogugua S.N and Kokwe N.N)

- ♥ Many thanks to my fellow physics research mates (Sithole T.M and his fiancé Mokoena P, Tebele A.S, Foka K.E, Lephoto M.A (Dunkie), Mokoena M.S, Ungula J, Mlotshwa D.V, Ali Wako, Ali A.G, Mphuthi M, Mabuya B and Magubane T).
- ♥ Collective and individual acknowledgments are also owed to my friends outside physics for their support and encouragement (Tsotetsi Edward Ramotse and Maboya Sunnyboy Chale).
- ♥ Last but not least, my fiancée **Tshabalala Noma Princess** who supported and incented me to strive for my goal. She witnessed and she can attest on my hard work.

Abstracts

The ZnO nanostructures were successfully synthesized by chemical bath deposition method (CBD) to study the influence of parameters such as reaction temperature, time, precursor concentration and the annealing temperature respectively. The main motivation for this thesis is to successfully synthesise novel ZnO nanostructures and understand the growth mechanism. In this work, the thermal, structural, morphology, optical, and luminescence properties of ZnO were investigated in details by means of thermogravimetric analysis (TGA), differential scanning calorimetry (DSC), x-ray diffraction (XRD), scanning electron microscopy (SEM), energy dispersive spectrometer (EDS), x-ray photoelectron spectroscopy (XPS), ultraviolet visible (UV-vis) spectroscopy and photoluminescence (PL) spectroscopy techniques.

From TGA results when increasing both reaction and annealing temperature we observed the increase in thermal stability of ZnO due to the removal of adsorbed species in the material. The melting temperatures (as determined through DSC) decreased due to crystallization of ZnO with the increase in both reaction and annealing temperature.

X-ray diffraction (XRD) indicated that all the ZnO nanostructures prepared at 80 ℃ crystallizes in the wurtzite structure with the mean lattice parameters a = b = 3.25 Å and c = 5.18 Å and there is an increment in the particle size resulting into the improvement of crystallinity of the material. In materials prepared at lower reaction temperature, reaction time, and precursor concentration, traces of zinc hydroxide $Zn(OH)_2$ were observed. When $Zn(OH)_2$ decomposes into ZnO, the entire surface morphology through the study of ZnO consisted of agglomerated nanoflakes. The EDS results confirmed the presence of Zinc (Zn) and Oxygen (O) as the major product, and the ratio of Zn to O increased as ZnO becomes more crystalline.

The UV-Vis reflectance spectra showed that the absorption band edges shift to the higher wavelength with an increase in reaction time, temperature, molar concentration precursors, and annealing temperature. As a result the band gap energy of ZnO nanostructures determined using Kubelka Munk's equation was found to decrease due to quantum confinement effects and the increase in particle size.

In general, the photoluminescence (PL) analysis showed that ZnO nanoflakes prepared at different parameters have almost the same characteristics. PL measurements revealed broad emission that extends from UV region to the visible region. The luminescence intensity of this emission was quenched when increasing parameters mentioned above, and these quenching is attributed to the decrease in concentration of defect related emissions. It is well known that when using chemical reaction methods such as CBD the emission intensity quenches as $Zn(OH)_2$ dehydrates into ZnO. The slight red-shift in the emission band is also observed which is attributed to band gap narrowing.

Keywords: ZnO, Chemical bath deposition, Growth mechanism, Nanoflakes, Band gap

Acronyms

CBD	–	Chemical Bath Deposition
XRD	–	X-ray Diffraction
TGA	–	Thermo Gravimetric Analysis
DSC	–	Differential Scanning Calorimetry
SEM	–	Scanning Electron Microscopy
EDS	–	Energy Dispersive Spectrometer
UV-Vis	–	Ultraviolet – Visible Spectroscopy
PL	–	Photoluminescence
XPS	–	X-ray Photoelectron Spectroscopy
JCPDS	–	Joint Committee on Powder Diffraction Standards
FWHM	-	Full Width at Half Maximum

Table of Contents

Table of Figures

1

Definition of the research work

1.1 Overview

A research project in nanoscience can be driven by two major motivations. The first and important most is when there is a well-defined application as the final goal. The second is when the research may be effective in several applications and the project deals with basic properties. The research work presented in this thesis is motivated by a mix of both of the above through manipulation of matter at the nanoscale.

On daily basis we use computers, vehicles and various kinds of machines due to improvements in nanoscience and nanotechnology. The creation and utilization of new materials, devices and systems at the molecular level is believed to be one of the biggest driving forces in the research of nanoscience in the 21st century [1]. The entire world is seeking for material that possesses inherent properties like larger band gap, higher electron mobility as well as higher breakdown field strength. So when making investigations about such a material the name "Zinc Oxide (ZnO)" comes out, this is a wide band gap semiconductor material capable of satisfying the above required properties. Not only has this ZnO possessed many versatile properties for UV electronics, spintronic devices and sensor applications [2]. Also ZnO has been commonly used in its polycrystalline form over hundred years in a wide range of applications. As a result many research groups all over the world are motivated to develop proper growth and processing techniques for the synthesis of ZnO [3 – 4]. Much research on ZnO has been done right from the beginning of 1950, with much focus on electrical and optical properties such as N-type conductivity, absorption spectra and electroluminescence decay parameters [5]. With the emerging possibilities to grow and handle nanometer sized particles, there are still much more to discover both regarding fundamental properties and applications.

In this study, the main focus is on ZnO phosphor particles that are in the nano-scale. A phosphor can be defined as any material that will emit light when an external excitation source such as electron beam or photons is applied [6]. These phosphors may either be in the

powder or thin film form. The phosphor materials can be doped intentionally with certain impurities to tune their properties [7]. These phosphor powders and thin films are critical in the development and improvement of display technologies. In order to obtain high-resolution images, phosphor particles with very small size must be produced. Achievement in the production of small phosphor production can lead to development of phosphor fine particles with stronger emission intensities [8]. Phosphor particles that have sub-micrometer size, narrow particle distribution and spherical morphology give higher particle packing densities than commercial products (3-5 μm in size) and are therefore effective in the enhancement of luminescence efficiency [9].

1.2 **Research Motivation and Rationale**

The present work is motivated by the study of materials at the nanoscale and aimed at obtaining optimized growth conditions for ZnO nanostructures fabrication by chemical bath deposition and the investigation of the photoluminescence properties of these nanostructures. The project involves systematically investigation of the experimental parameters that leads to different morphologies and affected the structure property relationship of ZnO nanostructures. The main focus of the research will be on ZnO, with the bulk of the research being conducted on engineering its sizes and the corresponding band gap due to quantum confinement. This material is chosen for its potential for extensive research, their possible applications in optoelectronics, biological luminescence coding, and the potential generalization of results to other nanomaterials. Therefore, the primary focus of this thesis will be on the morphology, growth, and structure of nanomaterials. The goal is to understand the mechanisms that determine the different growth factors of the nanostructures and use that understanding for a rational design and growth of useful nanomaterials. Controlling the morphology of the nanoparticles is important to controlling the structural, optical and luminescence properties of materials.

1.3 Problem Statement

The implementation of new forms of high resolution and high efficiency displays created a vacancy for phosphors with enhanced properties. High efficiency materials with fine particles are found to allow further development of these new displays [10]. These nano-sized

phosphors display interesting properties such as ultra-fast recombination time, an increase in the band gap due to the decrease in particle size and high quantum efficiency for photoluminescence [11]. ZnO is of considerable interest as a phosphor for luminescent displays [12]. It has a wide band gap of 3.37 eV and a small Bohr radius of ~ 3 nm. This makes it a good phosphor for display devices and development of this phosphor can have a huge impact on the technology of the future.

Even though a range of interesting properties are associated with ZnO nanostructures, there are still significant challenges that have to be overcome in order to produce efficient ZnO devices. These include:

- ✓ Developing synthesis methods with the ability to control its surface morphology and self-assembly into complex structures or device architectures.
- ✓ Demonstrate radically new applications for ZnO nanostructures.
- ✓ Controlling native defects and possible compensation processes.
- ✓ To understand the residual n-type conductivity in unintentionally doped ZnO.
- ✓ To succeed in growing of stable and repeatable p-type nanostructures.

In my opinion, there is a lot to be discovered about ZnO. Several fabrication techniques have been reported for the preparation of ZnO, which can be classified as gas-phase and aqueous solution-based methods. Amongst gas-phase methods, we have vapour-phase transport [13 – 14], pulsed laser deposition (PLD) [15], metal-organic chemical vapour deposition (MOCVD) [16 – 17], and molecular beam epitaxy (MBE) [18]. Although these methods are very helpful, they require complex processes and involve sophisticated equipment and high temperatures. Thus, aqueous solution-based method like chemical bath deposition (CBD), hydrothermal growth and sol-gel methods, are simple, requires no catalyst and is economical. Hence CBD is commercially feasible for large-scale production with good uniformity and can be operated at significantly lower temperatures [19].

The high concentration of native donor defects with low formation energies (resulting from non-stoichiometry of ZnO [20 – 21]) and the ever-presence of H (and related complexes) [22] are believed to be capable for the n-type conductivity of this material. It can be introduced unintentionally in most growth methods (either from the precursors, a carrier gas or residual gas), by laser ablation and by sputtering, or by annealing in H_2 atmosphere [23].

The other main obstacle for the commercialization of ZnO based homojunction devices is the absence of stable and reproducible p-type doping with high hole concentrations and large

carrier mobility. The major problems associated with this are the low solubility of most acceptor-type dopants, difficulties of substituting on the host atom sites, the relative deepness of the acceptor states and the spontaneous formation of compensating donor-like defects [24]. As a result, p-doping of ZnO remains unsolved problem.

The consistency on growth of nanostructures is another issue which has attracted considerable attention. It is well understood that the morphology of ZnO nanostructures is highly sensitive to the growth environment (i.e. temperature, pressure, precursors and their concentrations, the VI/II ratio or pH, etc.). As a result it is very difficult to control the growth process for the reproducible formation of a desired morphology over large areas [25].

1.4 Aim and Objective of the Research

The main aim for this research is to use cheap and effective method to prepare ZnO nanostructures and to compare ZnO prepared at different concentrations of zinc acetate precursor, effect of synthesis time, temperature and annealing temperature.

The overall objectives of this study are summarized as follows:

i. To investigate the influence of reaction temperature on luminescence properties of ZnO nanopowders prepared by chemical bath deposition method.
ii. To study the effect of reaction time on structural, morphology and optical properties of ZnO nanoflakes prepared by chemical bath deposition method.
iii. To optimize with the aid to obtain moderate zinc acetate concentration for the preparation of ZnO using chemical bath deposition method.
iv. To investigate the influence of annealing temperature on luminescence properties of ZnO nanopowders prepared by chemical bath deposition method.

1.5 Thesis Outline

The current thesis is composed of eight chapters.

Chapter 1: The current chapter focused on the factors that brought motivation to conduct research, the main aim and how the rest of the thesis is laid out.

Chapter 2: Reviews the existing literature related to the properties of ZnO nanoparticles, determination of crystallite size of semiconductors, background of nanoscience/nanotechnology and theory of Luminescence.

Chapter 3: Provides an overview of characterization techniques used to analyze the results.

Chapter 4: Monitors the best low reaction temperature for the preparation of ZnO controlled using chemical bath deposition technique

Chapter 5: Investigates the role played by the reaction time on structural, morphology and optical properties of ZnO

Chapter 6: Presents the results obtained during preparation of ZnO at various concentrations of zinc acetate.

Chapter 7: Thoroughly investigates the influence of annealing temperature on the as-prepared ZnO nanopowders.

Chapter 8: Summarizes the goal of the thesis and presents recommendations for future work in the light of obtained results. Lastly it provides list of publications resulting from this work and the conferences presentations.

1.6 References

[1] A.L. Rogach, A. Eychmuller, S.G Hickey and S.V Kershaw, *Reviews; Infrared emission*, www.small-journal.com, **3** (2007) 536

[2] R. Brayner, S.A Dahoumane, C. Yéprémian, C. Djediat, M. Meyer, A. Couté and F. Fiévet, *Langmuir* **26** (2010) 6522 – 6528

[3] A. Bakin, A. El-Shaer, A. Che Mofor, M. Kreye, A. Waag, F. Bertram, *J. Cryst. Growth.* **287** (2006) 7 – 11

[4] L.L. Yang, Q. X. Zhao, M. Willander *J. Alloys. compd.* **469** (2009) 623

[5] A.R. Hutson, *Phys. Rev.* **108** (1957) 222 – 230

[6] R.S. Fontenot, K.N. Bhat, C.A. Owens, W.A. Hollerman, M.D. Aggarwal, *J. Lumin.* **158** (2015) 428 – 434

[7] G. Heiland, E. Mollwo and F Stockmann, *Solid State Phys.* **8** (1959) 193 – 196

[8] C.R Ronda 2008 *Willy-VCH*, Germany, (2008) 3

[9] T. Hirai, Y. Asada and I Komasawa, 2004 *J. Colloid Interface Sci.* **276** 339

[10] L. Sun, C. Qiang, C. Liao, X. Wang and C. Yan 2001 *Solid State Commun.* **119** 393

[11] M.S. Dhlamini *PhD Thesis*, University of the Free State, South Africa (2008) 4 – 5

[12] B.S.R. Devi, R. Raveendran and A.V. Vaidyan *Pramana – J. Phys.* **68** (2007) 679

[13] J.S. Lee, K. Park, M.I. Kang, I.W. Park, S.W. Kim, W.K. Chom, H.S. Han and S. Kim, *J. Cryst. Growth* **254 (**2003) 423

[14] Q.X. Zhao, P. Klason and M. Willander, *Appl. Phys. A* **88** (2007) 27

[15] M.H. Huang, Y. Wu, H. Feick, N. Tran, E. Weber and P. Yang, *Adv. Mater.* **13** (2001) 113

[16] Y. Sun, G.M. Fuge and M.N.R. Ashfold, 2004 *Chem. Phys. Lett*. **396** 21

[17] J. Wu, S.C. Liu, *Adv. Mater.* **14** (2002) 215

[18] A. Bakin, A. El-Shaer, A.C. Mofor, M. Kreye, A. Waag and F. Bertram, *J. Cryst. Growth* **287** (2006) 7 – 11

[19] L.L. Yang, Q.X. Zhao and M. Willander, *J. Alloys. Compd.* **469** (2009) 623

[20] A.F. Kohan, G. Ceder, D. Morgan and C.G. Van de Walle, *Phys. Rev. B* **61** (2000) 15019

[21] B.K. Meyer, H. Alves, D.M. Hofmann, W. Kriegseis, D. Forster, F. Bertram, J. Christen, A. Hoffmann, M. Straßburg, M.A. Dworzak, U. Haboeck and A.V. Rodina *Phys. Stat. Sol. (B)* **241** (2004) 231– 260

[22] G.A. Shi, M. Saboktakin, M. Stavola and S.J. Pearton, *Appl. Phys. Lett*. **85** (2004) 5601

[23] C. Jagadish and S.J. Pearton, *Austeralia*: Elsevier Limited (2006)

[24] U. Uzgur, Y.I. Alivov, C. Liu, A. Teke, M.A. Reshchikov, S. Dogan, V. Avrutin, S.J. Cho and H. Morkoc, *J. Appl. Phys.* **98** (2005) 04130

[25] Z.N. Urgessa *PhD thesis* Nelson Mandela Metropolitan University (2012) 2 – 4

2

Chemical and Physical Properties of ZnO

2.1 Introduction

Zinc oxide is an inorganic compound produced from group (II) and (IV) elements with the formula ZnO. ZnO has been under extreme focus since 1935 due to its outstanding properties [1]. It has wide range of applications that includes numerous materials and products such as rubbers, plastics, ceramics, glass, cement, lubricants wherein it acts as an additive [2]. Mostly ZnO is produced synthetically using different preparation methods, but it occurs naturally as the zincite mineral [3]. Thus, in this chapter we start first by introducing some basic properties of ZnO semiconductor.

2.1.1 Chemical Properties

The pure ZnO as indicated above is found to be a white powder, and it is found rarely in nature as the mineral zincite which usually contains manganese and other impurities that confer a yellow to red color [4]. ZnO in the crystalline form is said to be thermochromics, which means its color changes from white to yellow under heat treatment but when exposed to air or cooled it changes back to the original color [5]. The color change is mainly due to small loss of oxygen to the environment at high temperatures to form the non-stoichiometric $Zn_{1+x}O$, where at 800 °C, x = 0.00007 [5]. It is said to be amphoteric oxide, meaning it is capable of reacting as acid or water, but it is nearly insoluble in water and it is soluble in most acids [6]. The reaction of ZnO with acids can be explained by the chemical reaction in equation (2.1) where it reacts with hydrochloric acid,

$$ZnO + 2\ HCl \rightarrow ZnCl_2 + H_2O \qquad (2.1)$$

2.1.2 Physical Properties

ZnO has two main structures hexagonal wurtzite and cubic zinc blend [7]. The structure wurtzite was the focus of the study because it is the most stable at ambient conditions and thus most common [8]. The wurtzite structure has lattice parameters a = 0.3296 and c = 0.52065 nm. The structure of ZnO can be simply described as a number of alternating planes composed of tetrahedral coordinated O^{2-} and Zn^{2-} ions, stacked alternately along the c-axis as shown in **Figure 2.1**. This tetrahedral coordination gives rise to polar symmetry along the hexagonal axis. This polarity is responsible for a number of the properties of ZnO, including its piezoelectricity and spontaneous polarization, and is also a key factor in crystal growth, etching and defect generation [9].

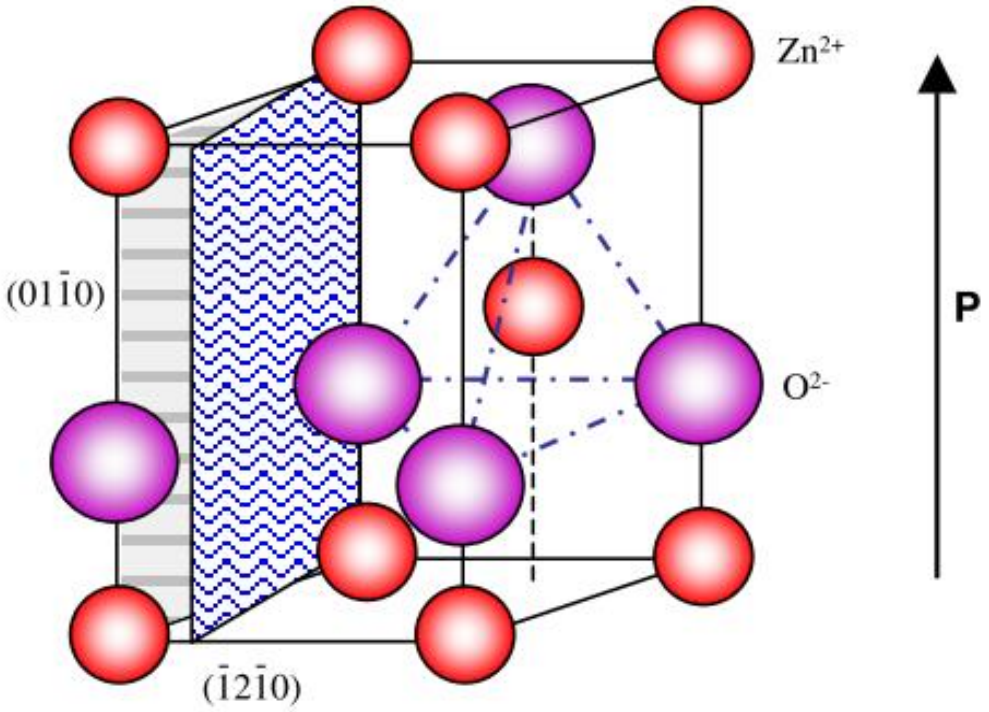

Figure 2.1 The wurtzite structure of ZnO, tetrahedral coordination of Zn–O is shown [10].

2.1.3 Optical Properties

ZnO has many defect centres as shown in **Figure 2.2**, some of which are attributed to oxygen vacancies and zinc interstitials but other luminescence mechanisms are not really understood [11]. ZnO consists of wide and direct band gap energy of 3.36 eV at room temperature [12].

The bandgap of ZnO can thus be tuned to ~3 – 4 eV by introducing some impurities through the doping process. Furthermore it consists of large exciton binding energy of 60 meV which indicates that efficient excitonic emission in ZnO can persist at room temperature and higher [13]. Because the oscillator strength of excitons is typically much larger than that of direct electron–hole transitions in direct gap semiconductors [14], the large exciton binding energy makes ZnO a promising material for optical devices that are based on excitonic effects.

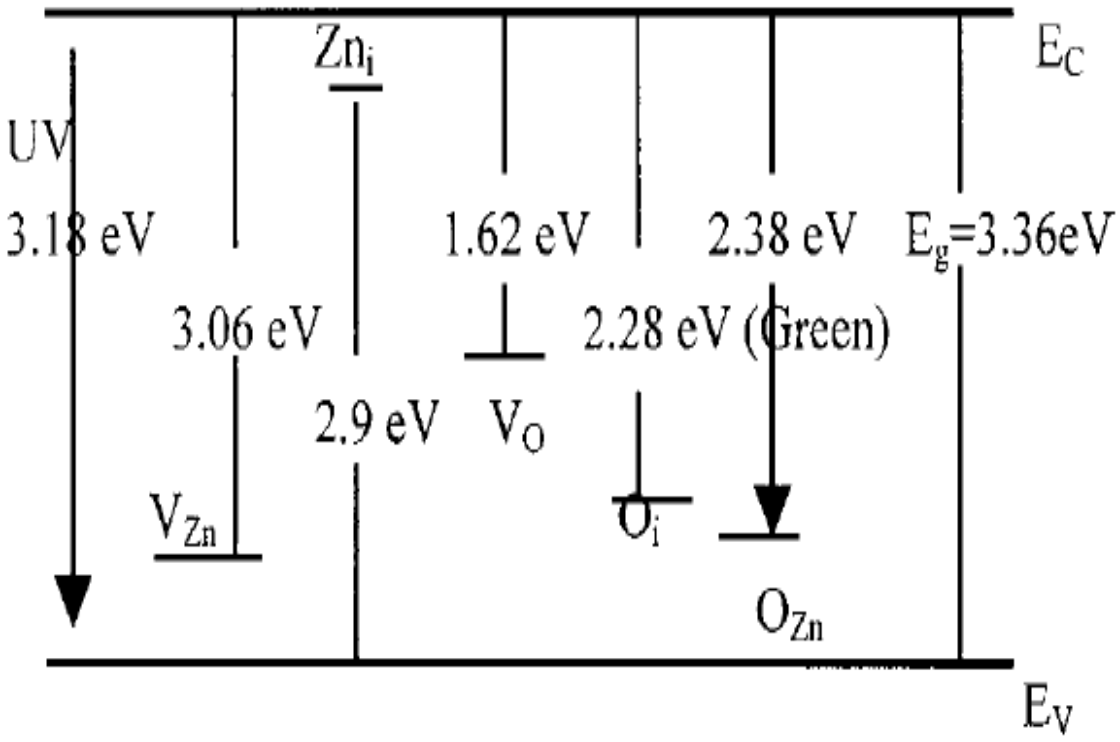

Figure 2.2 Schematic diagram of the position of various intrinsic defect levels emission within ZnO [12].

2.2 Nanoscience and Nanotechnology

Lately, nanoscience and nanotechnology research in South Africa (S.A) is receiving much attention [15] and there is a recently implemented master's programme named National Nanoscience Postgraduate Teaching and Training Programme. Not only in S.A but worldwide a lot of research is conducted in the nano scale, and the European Union declare nanotechnology as the field of highest priority [16]. Most recently the year 1912 has been proposed as the birth of modern field of nanotechnology, this coincide with the invention of the immersion ultramicroscope by Zsigmondy [17]. But it is well known that the history of

nanotechnology came along with physicist Richard Feynman [18]. This Nobel Laureate winner for Physics in 1965 gave the speech "There's Plenty of Room at the Bottom". It happened at the American Physical Society annual meeting in 1959 at the California Institute of Technology where he pointed out the potential of nanotechnology. Furthermore, he said there is a possibility to manufacture nano-sized products using atoms as building particles. In 1974, at the international conference on industrial production in Tokyo, the word "nanotechnology" was first used by Norio Taniguchi to describe ion sputtering process for creation of nano-sized particles [19]. He outlined "Nanotechnology" by saying it mainly consists of the processing of separation, consolidation, and deformation of materials by one atom or one molecule.

Nanoscience/nanotechnology is a field that includes biomedical sciences, chemistry and physics as well as applied technologies. It has attracted the attention of researches in a way that lot of funding has been pumped into this field over the last two decades. An extreme way to explain what is nanoscience is to consider everything that has one dimension smaller than one hundred nanometers. Hence, tiny particles with typical sizes in the range (1 – 100 nm) and atomic size (approximately 0.2 nm) are considered nano. The word nano is Latin from Greek – that means "dwarf" and it is used in the metric system to mean 10^{-9} or one billionth (1/1,000,000,000) [20]. It is at this scale that the properties of materials become very different from bulk materials at large scale. Thus many things which cannot be achieved with big and bulky can easily be accomplished with very small (nano). Nanoscience is a very promising field with rapid advances across many areas of science and engineering that are more important for the development of the entire society.

2.2.1 Nanotechnology can be subdivided into three distinct nanotechnologies.

"Wet" nanotechnology

This technology mainly focuses on biological systems that are often found in wet environments such as water [21]. The active interest of this field that is functional at the nanometer scale deals with structures found in genetic materials, membranes, enzymes and other cellular components like the one shown in **Figure 2.3**. Due to high surface area to volume ratio and unique properties of nanoscale materials novel antimicrobial agents are produced [22 – 23]. Availability of living organisms whose form, function and evolution are

governed by the interactions of nanometer structures proves that “wet” nanotechnology is growing big.

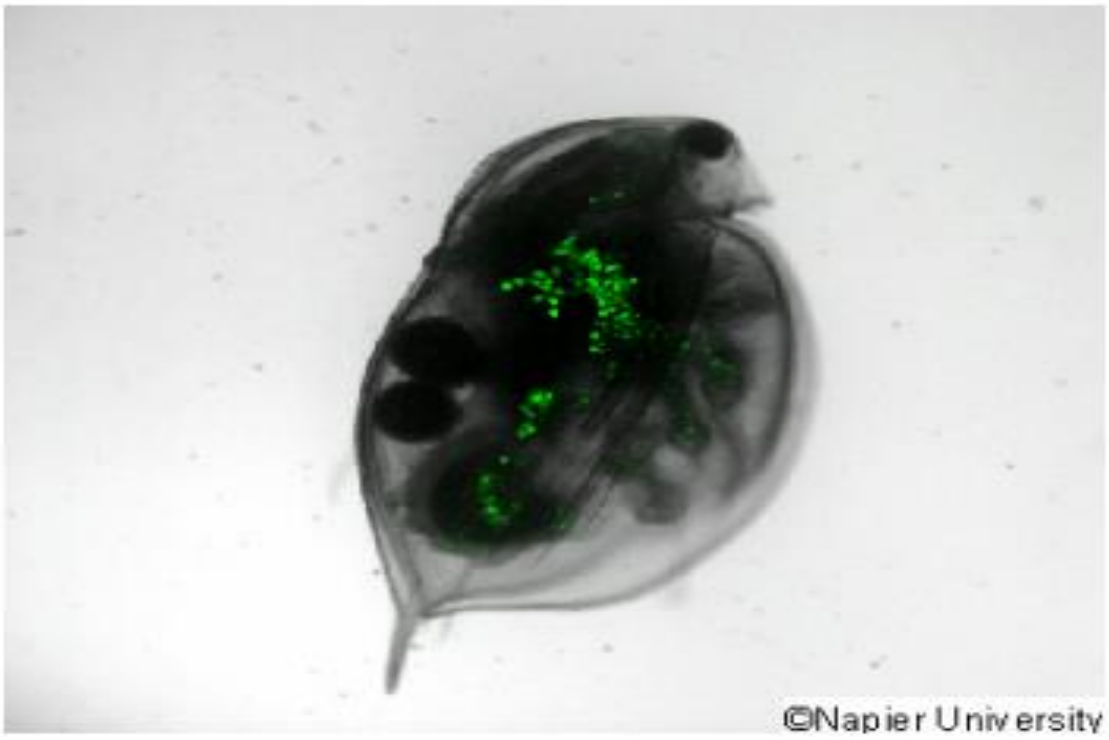

Figure 2.3 Fluorescent nanoparticles in water flea (Daphnia magna) [24].

“Dry” nanotechnology

This technology is deduced from the study of surface science and physical chemistry; it mainly focuses on the manufacturing of structures in carbon (e.g. graphene, fullerenes and nanotubes), silicon and other inorganic materials indicated in **Figure 2.4**. In comparison to “wet” technology the “dry” techniques makes use of metals and semiconductors. The excited electrons to move onto the conduction band for semiconductor materials becomes too reactive operation in a “wet” environment, and the same electrons provide the physical properties that make “dry” nanostructures promising as electronic, magnetic, and optical devices. In this technology there is implementation of “dry” structures that possess some of the properties that can be obtained through “wet” technology.

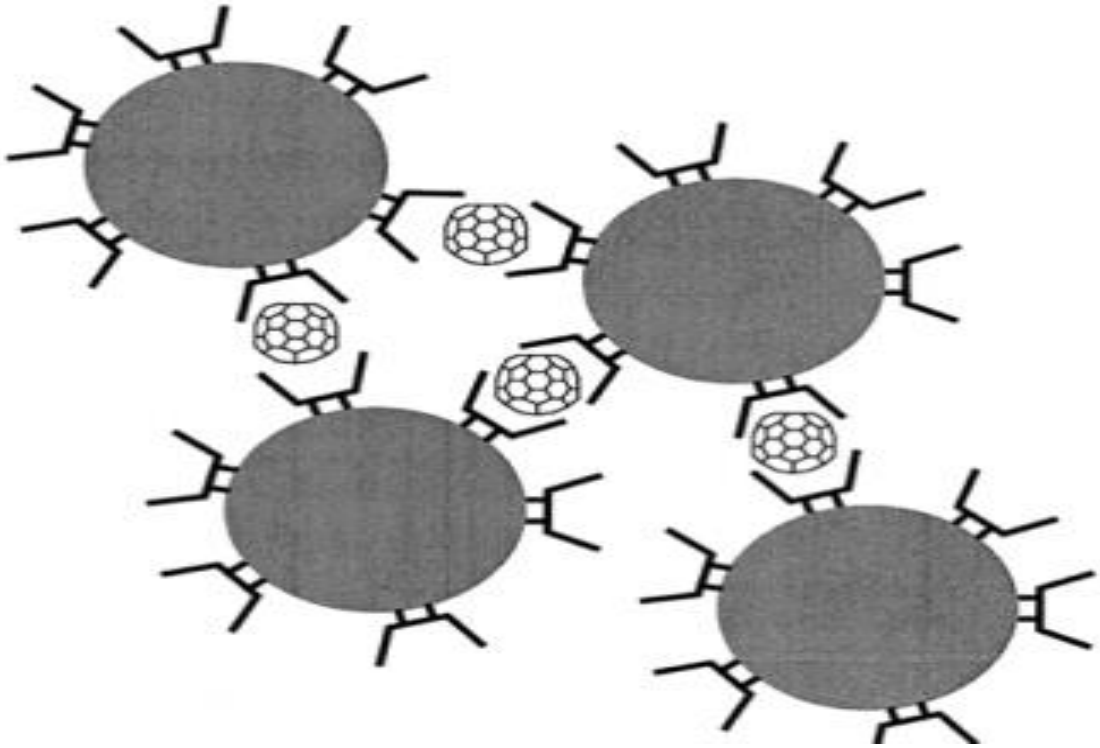

Figure 2.4 Fullerenes induced network of γ-cyclodextrin [25].

“Computational” nanotechnology

This technology deals with computer modelling and simulation of complex nanostructures similar to the one indicated in **Figure 2.5**. The predictive and analytical power of computation is vital for development of nanotechnology. It took couple of hundred million years to naturally evolve a functional “wet” nanotechnology. The core implemented by computation should allow us to reduce the development time of a working “dry” nanotechnology to a few decades, and it will have a major impact on the "wet" side as well.

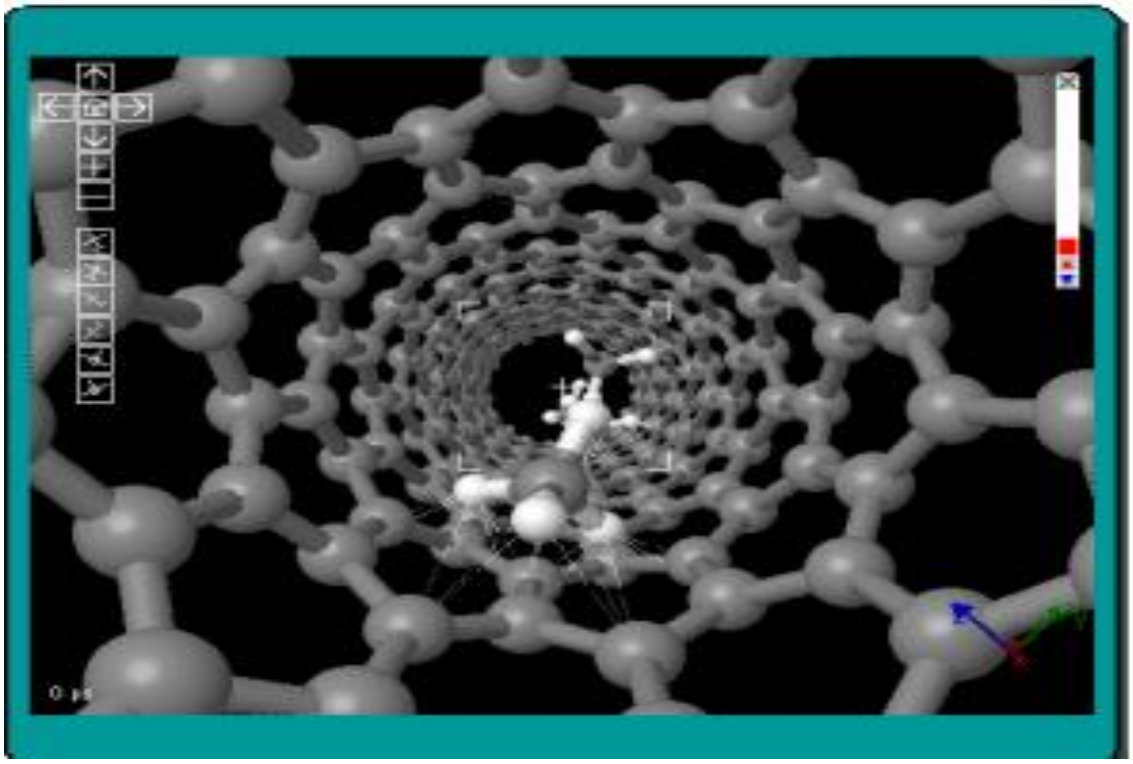

Figure 2.5 All-atom molecular dynamics simulation of motion of methane molecules in a carbon nanotube [26].

The above mentioned nanotechnologies are highly interdependent. The major advances in each have often come from application of techniques or adaptation of information gathered from each one or both.

Many different structures can be considered nano whenever their size is so small that the length scale depends on material and system. Nanostructured particles of ZnO come in different shapes and the small selection is shown in **Figure 2.6**. This includes dots, rods, flowers, rings, spheres, spirals and needles etc. This variety of structures for ZnO offers wide range of applications.

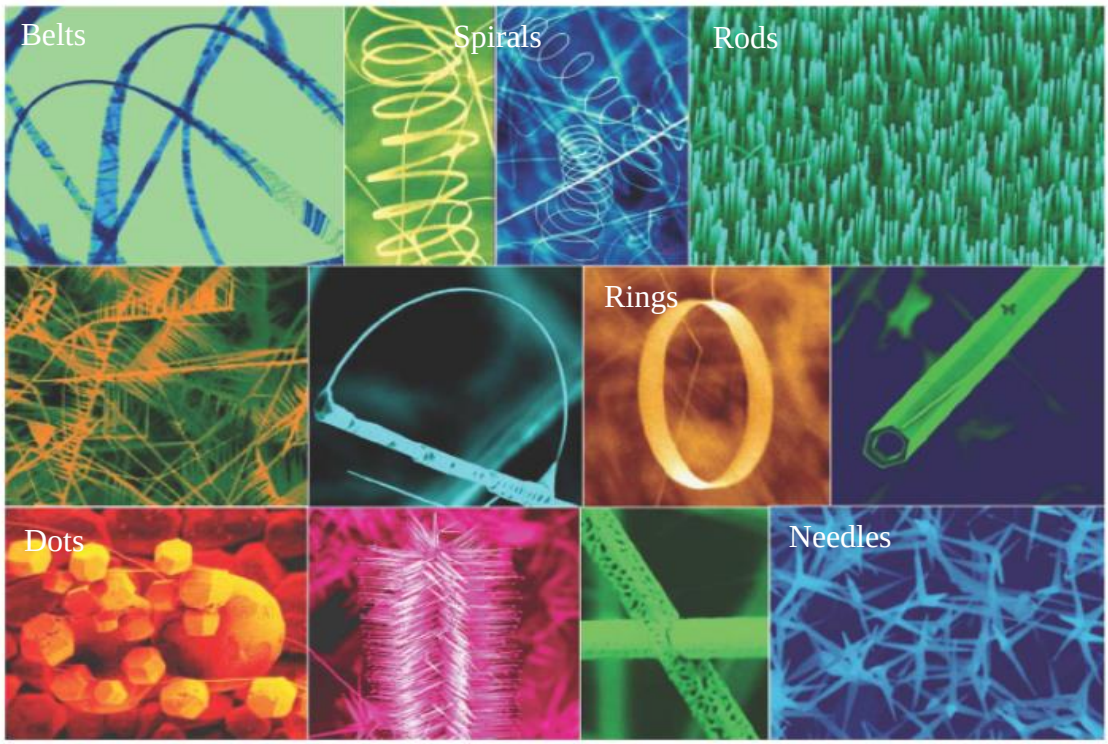

Figure 2.6 Examples of ZnO structures [27].

2.3 Theory of Luminescence

Luminescence is a process of emission of electromagnetic radiation by a physical system through excitation of electrons/photons [28]. This physical system can be a phosphor material converting energy from one state to another. Phosphor is a Latin name from Greek which simply means light carrier [29]. The phosphor material can be a compound on its own as a host or it can be composed of host and dopant. Phosphors were discovered in the 16th century by Vincenzo Casciarolo of Bologna [30 – 31]. This guy fired the stone presented in **Figure 2.7** intending to produce metal unfortunately the stone was found to emit red light after being exposed to sunlight. In general phosphor appears as powder with a particle size ranging from micro to nanometer but they can also be thin films [32].

Phosphors are materials that give out luminescence and they are mainly solid materials under solid state physics. Again luminescence is a common term among inorganic and organic as well as in semi-conductors. The luminescence materials can be fluorescence or phosphorescence. In order for luminescence to take place an amount of energy from an excitation source kicks an electron from its stable sate into an excited state. The electron will relax from the excited state to the ground state by releasing that energy in the form of light [33].

Figure 2.7 A piece of Bolognian Stone, $BaSO_4$ (barite), with a maximum diameter of about 12 cm, found on Monte Paderno, Bologna. Part of the private collection of Aldo Roda [34].

2.3.1 Fluorescence and Phosphorescence

Fluorescence is the emission of light which take place from an excited singlet state with a characteristic time $t_c < 10^{-8}$ s. In phosphorescence, on the other hand, emission originate from excited triplet state with a characteristics time $t_c > 10^{-8}$ s. To clarify between fluorescence and phosphorescence is to study the effect of temperature upon the decay of the luminescence. Fluorescence is essentially independent of temperature; whereas the decay of phosphorescence exhibits strong temperature dependence [36]. Fluorescence is part of luminescence which involves emission of light from any substance in the excited state. The absorption and emission process for fluorescence is shown in the Jablonski diagram **Figure 2.8** where an electron is excited from the ground to a higher electronic and vibrational state. In this process the excited electrons can relax at the low vibrational state because of vibrational relaxation, and then continue to the ground state giving fluorescence emission. In fluorescent materials electrons are located at certain energies in the impurity state band for a very short time (10^{-9} to 10^{-6} seconds). Furthermore, they emit light as their energy levels changes to energy in the valence band. As a result, fluorescent materials will give emission only when light of sufficient energy is used to excite electrons.

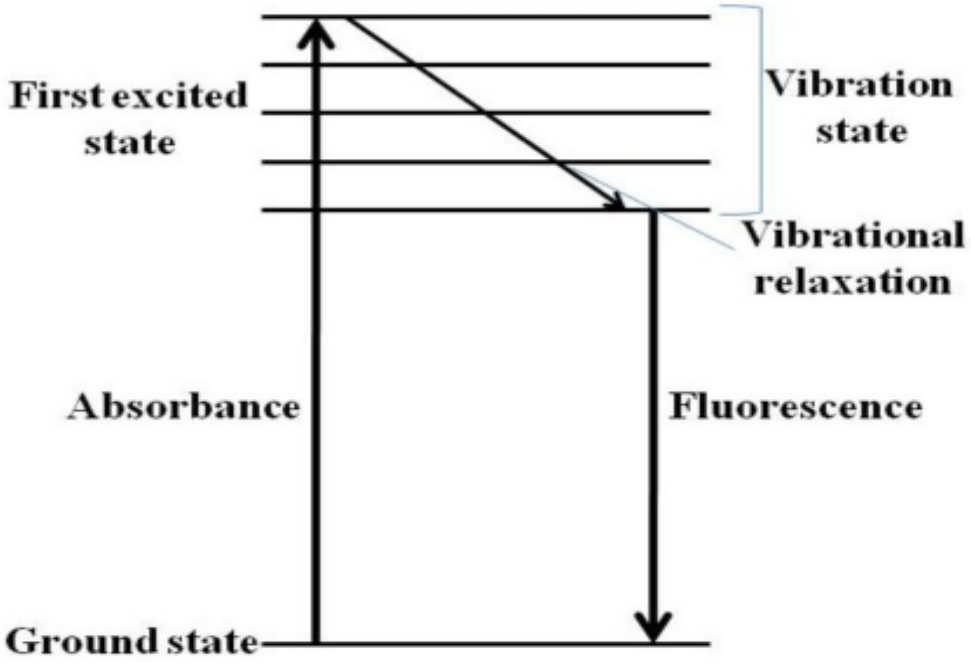

Figure 2.8 Jablonski diagram of fluorescence [35].

Figure 2.9 White and other colours of organic light emitting diode OLED used in car lighting [39].

In some materials, electrons excited by the original radiation can take some time to decay back to their ground states. The decays can take as long as few hours to few days. This type of fluorescence is called phosphorescence and the material continues to emit visible light for a while after the original radiation has been switched off [37]. If the duration is very short, around 10^{-4} s, then the material is a short persistence phosphor. If it lasts for seconds or longer it is a long persistence phosphor [38]. Objects similar to the one presented in **Figure 2.9** which display phosphorescence are sometimes said to be luminous. In phosphorescent materials the excited electrons stays in the impurity state, then as their energy changes they emit light in the form of photons. The emission of light may be attained using various forms of luminescence discussed below [25].

Photoluminescence

During photoluminescence absorption of an ultraviolet or visible photon promotes a valence electron from its ground state to an excited state with conservation of the electron spin. In this process, pair of electrons with opposite spins occupying the same electronic ground state are said to be in a singlet spin state. When a photon is absorbed one electron gets promoted to a singlet excited state.

Thermoluminescence

It is a form of light emission that occurs when the temperature of the object is increased after exposure to some form of energy excitation (heat) which is obtained in the form of phosphorescence.

Cathodoluminescence

It is the process that uses electrons as excitation source to impact on luminescent material such as phosphor to attain the light emission. This process mostly takes place in the surface of the screen of a television that uses a cathode ray tube coated with phosphoric material [40].

Electroluminescence

This is the form of luminescence developed after exciting the material using electric field/electric current as the source of excitation and material emits light in response.

Radio luminescence

It is the phenomenon in which light emission is developed in a material due to excitation with ionizing radiation such as beta particles and X-rays.

2.4 Literature survey of size determination of semiconductor nanoparticles

Due to improvements in science the modern semiconductor technology generates a way to fabricate particles of metals which are few hundred angstroms in size [41]. Such small particles are called nanoparticles and their size can be determined in many different ways. The mean size of nanoparticles can be evaluated using various measurement techniques such as X-ray diffraction (XRD), UV-Vis spectroscopy, transmission electron microscopy (TEM) and direct light scattering (DLS) [42]. The crystalline size is the measure of the size of coherently diffracting domains. And the crystalline size of particles is not generally the same as the particle size due to the formation of polycrystalline aggregates [43]. It is very important to know the description of the particles because they become increasingly significant as the size decreases.

2.4.1 UV – Vis Absorption

UV – Vis absorption is a very first characterization method for the nanoparticles because the absorption features give information about the nanoparticles formation, the band gap energy and the size distribution of the nanoparticles. However, it is an indirect method for determining the crystallite size. The band gap of the particles can be calculated from the excitonic peak position which is used to determine the crystallite size as shown in **Figure 2.10**. In the most recent years, nano-scientists research mainly focused on various interesting properties of semiconductor particles [44 – 45]. It has been discovered that when semiconducting nanoparticles are in the range 1 – 10 nm, energy level splitting takes place hence these particles are called quantum state particles/Q-particles. The radius of particles in the wavelength range mentioned above can be calculated because Q-particle has different characteristics compared to bulk state. Thus to predict the quantum confinement, effective mass approximation model based on ‘Particle in the box Model’ is used. The model was first proposed by Efros and Efros [46] in the year 1982 and later modified by Brus [47]. Brus

formulated the popular effective mass model that relates crystallite size (neglecting spatial correlation effects) to the bandgap energy of a semiconductor Q-particles [48 – 49],

$$\Delta E_g(r) = E_g(bulk) + \frac{h^2}{8r^2}\left(\frac{1}{m_e^*} + \frac{1}{m_h^*}\right) - \frac{1.8e^2}{4\pi\varepsilon_0\varepsilon r} \qquad (2.2)$$

where $\Delta E_g(r)$ is the energy band gap of the emission depending on particle radius *r*, $E_g(bulk)$ is the energy band gap of bulk solid, *h* is the Planck's constant, m_e^* is the effective mass of excited electron in the solid, and m_h^* is the effective mass of excited hole in the solid, ε_0 is the vacuum permittivity and ε is the dielectric constant of the solid. The middle term on the right-hand side of the equation is a particle-in-a-box-like term for the exciton, while the third term on the right-hand side of the equation represents the electron–hole pair Coulombic attraction, mediated by the solid [50]. Many experimental studies proved that the predicted value for $\Delta E_g(r)$ and crystallite size cannot be quantitatively accurate for very small particles [51], in the case of semiconductors small particles are those with size smaller than exciton Bohr radius such as ~ 3 nm for ZnO [52]. This happens because for small particles the eigenvalues of the lowest excited states are located in a region of the energy band that is no longer parabolic [51]. But, there are many theoretical approximations that are accurate in predicting experimental band gap energies and crystallite sizes [53 – 54].

The Brus equation can be used to determine the effect of quantum confinement on semiconductor materials such as GaAs, ZnS and ZnO at different confinement radii. For particles with large sizes (> 3 nm Bohr radius of ZnO) the electron and hole are both confined in a spherical well. This quantum confinement increases the band gap as the size of the bulk particles decreases and it gives the dominant effect in this size regime. In these large particles (> 3 nm Bohr radius of ZnO), the negatively charged electron and the positively charged hole are separated and hence the coulomb attraction between them can be neglected. However, in small particles (< 3 nm Bohr radius of ZnO) the coulomb attraction energy between the electron-hole pair cannot be neglected. While the band gap still increases with decreasing crystallite size, in small particles this increase can be overcome by the coulomb energy that the spectra shift to lower energies. When the size of nanoparticles approaches that of the Bohr radius 3 nm of ZnO for instance, quantum confinement effects result in the blue shifting of the band gap [55 – 56].

In order to compute emission energy states, the overall Brus equation depicted in equation (2.2) can be employed. The most important features of semiconductor nanoparticles are the size evolution of the optical absorption spectra. Hence the crystallite size of these particles is computed from absorption edge in UV–visible absorption spectroscopy which is powerful tool to monitor the optical properties of quantum-sized particles. Different sized nanoparticles absorb at different wavelengths and provide varying band gap energy and optical properties. When calculating the crystallite size the wavelength corresponding to the absorption edge maximum in the experimentally determined data is measured as indicated in **Figure 2.10**.

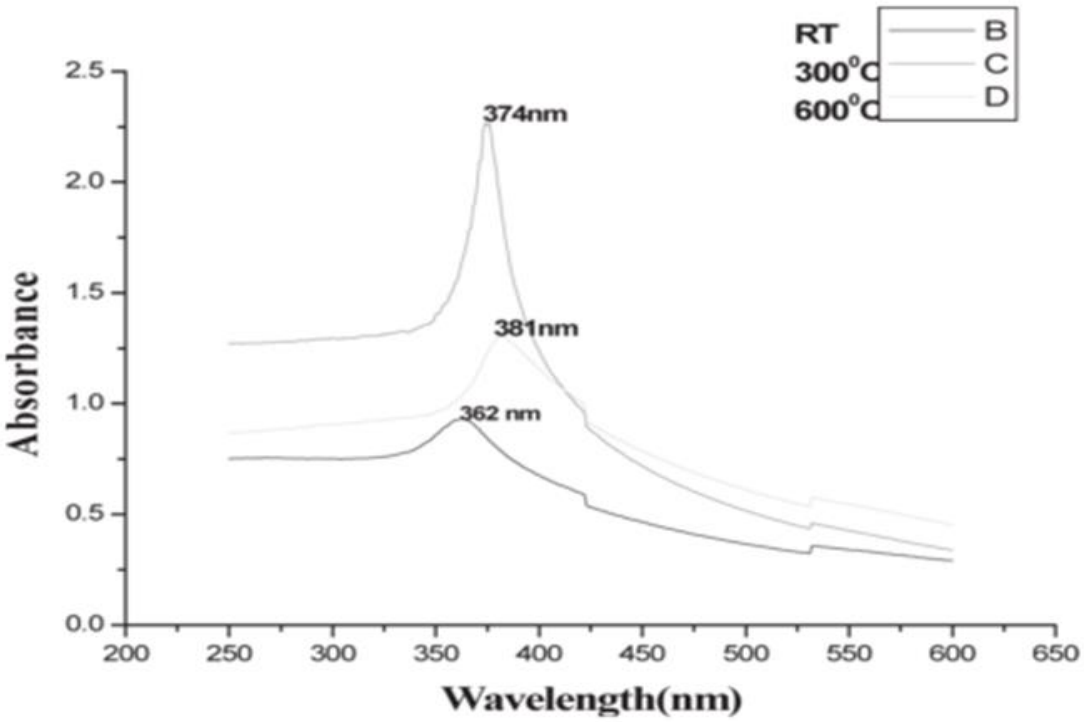

Figure 2.10 Absorption spectrum of ZnO nanoparticles [59].

Mostly, these wavelengths of the maximum exciton absorption decreases as the crystallite size increases due to quantum confinement of the photo-generated electron–hole pairs [51]. As a result the energy levels in the nanoparticles (< 3 nm Bohr radius ZnO) becomes discrete compared to continuous energy levels in bulk particles. Thus, the crystallite radius can be calculated using **equation** (2.3) after performing some small mathematical simplifications on the effective mass model equation (2.2) [48],

$$r(nm) = \frac{-0.3049 + \sqrt{-26.23012 + 10240.72/\lambda_p(nm)}}{-6.3829 + 2483.2/\lambda_p(nm)} \quad (2.3)$$

where λ_p is the peak absorbance wavelength in nm. Because of the small effective masses for ZnO semiconductor (m_e^* = 0.26 and m_h^* = 0.59), band gap enlargement is expected for crystallite radii relatively less than about 4 nm [57 – 58].

Figure 2.11 shows the energy difference between states and band gap for nanoparticles and bulk materials. It can be seen that ΔE_{nano} is greater than ΔE_{bulk} and this is believed to be caused by the reduction in dimensions of the quantum dot (QD) which increases the confinement energy in the dot (nanoparticles) [49]. The width of QD band gap energy depends on its size and chemical composition hence it is easy to tune absorption and emission of nanoparticles.

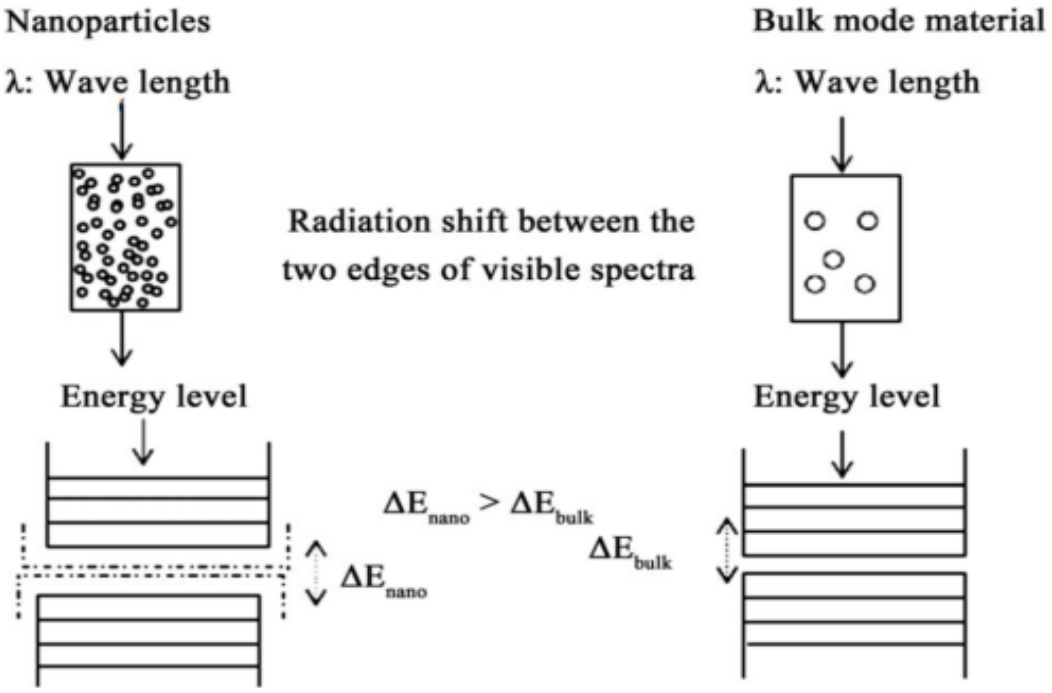

Figure 2.11 Energy difference between energy states and band gap for nanoparticles and bulk [60].

2.4.2 Xray Diffraction (XRD)

X-ray powder diffraction was used for structure and size determination by many groups [61 – 62]. The crystallite size can be obtained either by direct computer simulation of the X-ray diffraction pattern or from the full width at half maximum (FWHM) of the diffraction peaks using the Debye-Scherer formula [63 – 64]. The line width depends on the crystalline regions within the particles. When the particles are not perfectly crystalline a problem arises in the size estimation. Particles smaller than 2.5 nm lead to significant broadening of the line width, this is due to their extremely small dimensions [65]. X-ray profile analysis is the averaging method and it still holds a dominant position in crystallite size determination.

Scherrer's equation was established in 1918 by scientist Paul Scherrer for calculating crystallite size [66]. This crystallite size is determined from the width of X-ray diffraction data. The Scherrer equation is a convenient method to predict crystallite size if crystals are smaller than 100 nm [67]. Thus, the average crystallite size can be estimated using the well-known Scherrer formula,

$$D = \frac{K\lambda}{\beta_{hkl} Cos\theta} \qquad (2.4)$$

where D is the diameter of the crystallite in nanometres, λ is the wavelength of the incident X-ray (λ = 0.1540 nm) for CuK_{α} radiation, K is a constant related to crystallite shape equal to 0.90, β_{hkl} is the integral peak width at half-maximum intensity (FWHM) in radians and θ is the peak position in degrees.

When using equation (2.4), the crystallite size depends on X-ray diffraction patterns, and it is advisable to do the analysis using all reflections in the entire diffraction pattern to minimize errors. With no doubt the crystallite size depends on the width of the diffraction peak, the crystallite size is expected to decrease if the diffraction peak is broadened and vice-versa. Again XRD can be employed to evaluate peak broadening with crystallite size and lattice strain due to dislocations in material [68]. The FWHM or β_{hkl}, deserves to be corrected for the instrumental broadening which is done using equation (2.5), $\beta_{measured}$ is the measured FWHM and $\beta_{instrument}$ is the peak broadening due to the instrument which is the measured FWHM for a bulk sample. To separate the measured and instrument broadening, it is

essential to collect a diffraction pattern from the line broadening of a standard material to determine the instrumental broadening. The instrument – corrected broadening [69] β_{hkl} corresponding to the diffraction peak can be estimated using the relation,

$$\beta_{hkl} = \sqrt{\beta^2_{measured} - \beta^2_{instrument}} \tag{2.5}$$

The derivation of Scherrer equation is done by Alexander in Klug and Alexander "X-ray Diffraction" [70]. The derivation is done by taking the Bragg's Law,

$$\lambda = 2dSin\theta \tag{2.6}$$

This proceeds by keeping the wavelength λ constant and allowing the diffraction angle to broaden from a sharp diffraction peak, which start from the infinite single crystal with perfect three dimensional (3-D) structures. In a single crystal, the diffraction from a set of planes with the distance d^* occurs at a precisely θ^*, so that equation (2.6) can be written as follows,

$$\lambda = 2d^* Sin\theta^* \tag{2.7}$$

In polycrystalline nanoparticles, the diffraction from lots of tiny crystals deviates by $\pm\Delta\theta$ from θ^*. This implies $2\Delta\theta$ term on the 2θ axis of diffraction pattern and the value of $\Delta\theta$ correspond to FWHM or β_{hkl}, which is approximately half of $2\Delta\theta$. Simply because $\Delta\theta$ can be positive or negative, we need to take the absolute value which reflects the half width of the shape line deviation in 2θ axis. The derivative in d and θ of Bragg's Law with constant λ gives,

$$\lambda = 2\Delta d.Cos\theta.\Delta\theta \tag{2.8}$$

Thus the thickness $\Delta d = D$ can be written as follows,

$$D = \Delta d = \frac{\lambda}{2Cos\theta.\Delta\theta} = \frac{\lambda}{Cos\theta.\beta_{hkl}} \tag{2.9}$$

Finally we apply the shape factor K on equation (2.4), which is equal to 0.9 for CuK_α radiation, and this gives the Scherrer equation presented in equation (2.9).

2.5 References

[1] C.W. Bunn *Proc. Phys. Soc.* London **47** (1935) 835

[2] A. Hernandezbattez, R. Gonzalez, J. Viesca, J. Fernandez, J. Diazfernandez, A. MacHado, R. Chou and J. Riba, *Wear* **265 (**2008) 3 – 4

[3] M.D. Liedekerke, *Ullmann's Encyclopdia of Industrial Chemistry* Wiley-VCH, Weinheim (2006)

[4] C. Klingshirn, *Chem. Phys. Chem.* **8** (2007) 782 – 803

[5] E. Wiberg and A.F Holleman, *Inorganic Chemistry. Elsevier.* ISBN 0-12-352651-5 (2001)

[6] E. Alan *Chemistry of the Elements* (2nd ed.). Butterworth-Heinemann. ISBN 0080379419 (1997)

[7] K. Yuan, X. Yin, J. Li, J. Wu, Y. Wang, F. Huang, *J. Alloys Compd*. **489** (2010) 694 – 699

[8] Ü. Özgür, Y.I. Alivov, C. Liu, A. Teke, M.A. Reshchikov, S. Do˘gan, V. Avrutin, S.-J. Cho, H. Morkoc, *J. Appl. Phys.* **98** (2005) 041301

[9] O. Dulub, L.A. Boatner and U. Diebold, *Surf. Sci.* **519** (2002) 201

[10] Z.L. Wang, *J. Phys. Condens. Matter* **16** (2004) R829 – R858

[11] S. Shionoya and W.H. Yen, *Phosphor Handbook By Phosphor Research Society* (Boca Raton, FL: CRC Press) (1997)

[12] A. Mang, K. Reimann and St. R¨ubenacke, Solid State Commun. **94** (1995) 251

[13] A. Janotti and C.G. Van de Walle, *Rep. Prog. Phys.***72** (2009) 126501

[14] B.M. Junaid and V. Gopakumar, *J. Optelect and Biomed Mater*, **4** (2012) 1 – 7

[15] Kroon R.E *S. Afr. J. Sci.* **109** (2013) 1 – 2

[16] Jacobsson T.J [Online] *Mat. Chem.* (2009) 1 – 73 Accessed 28 November 2014

[17] T. Mappes, N. Jahr, A. Csaki, N. Vogler, J. Popp and W. Fritzsche, *Angew Chem. Int. Ed.* **51** (2012) 11208 – 11212

[18] R. Feynman, There's Plenty of Room at the Bottom. *Speech given at American Physical Society Meeting*, California Institute of Technology (1959)

[19] N. Taniguchi Proc. Intl. Conf. Prod. Eng. Tokyo, Part II, *J. S. Prec. Eng.* (1974) 18 – 23

[20] S. Gullapalli and A.R. Barron *http://creativecommons.org/licenses* **3.0** 580 – 588

[21] A. Shirley, B. Dayanand, Sreedhar and S.G. Dastager *Dig. J. Nanomater. Bios.* **5** 447 – 451

[22] J.R. Morones, J.L. Elechiguerra, A. Camacho and J.T. Ramirez, *Nanotechnol.* **1** (2005) 2346 – 2353

[23] J.S. Kim, E. Kulk, K.N. Yu, J.H. Kim, S. J. Park, H.J. Lee, *Nanomed. Nantechnol. Biol. Med.* **3** (2007) 95 – 101

[24] S.B. Lovern and R. Klaper, *Environ. Toxicol. Chem.* **25** (2006) 1132 – 1137

[25] M-C. Daniel and D. Astruc, *Chem. Rev.* **104** (2004) 293 – 346

[26] C. Xie and H-S.A Lee *Int. J. Eng. Educat.* **28** (2012) 1006 – 1018

[27] G.C. Yi, C. Wang and W. Park, *Semiconductor Science and Technology.* **20** (2005) 22 – 34

[28] D.R. Vij and N. Singh, *Nova Publishers, New York.* (1997) 169

[29] M.A. Lephoto, *M.Sc thesis* University of the Free State, RSA (2011)

[30] E.N. Harvey, *American Philosophical Society*: Philadelphia, PA, USA (1957)

[31] E.K. Van den, D. Poelman and P.F. Smet *Materials* **6** (2013) 2798 – 2818

[32] J.J. Dolo, *PhD thesis* University of the Free State, RSA (2011)

[33] G. Zimmerer, *J. Lumin.* **119 – 120** (2006) 1 – 7

[34] The Discovery of Luminescence: "The Bolognian Stone", [Online]. Available from https://www.fluorescence-foundation.org/lectures%5Cmadrid2010%5Clecture1.pdf Accessed (02 January 2015)

[35] L. Li and A.R. Barron *http://creativecommons.org/licenses/by/* **3.0** (2012) 61 – 75

[36] B. Li, Z. Jacobs, R.G. Roberts and S-H. Li, *Quat. Geochronol.* **17** (2013) 55 – 678

[37] Y. Yang, Z. Li, Z. Li, F. Jiao, X. Su and D. Ge, *J. Alloys Compd*. **577** (2013) 170 – 173

[38] C. Neary and A.J. Wilkins *Perception* **18** (1989) 257 – 264

[39] Y. Karzazi, *J. Mater. Environ. Sci.* **5** (2014) 1 – 12

[40] L Ozawa, CRC Press, Taylor and Francis Group, LLC (2007)

[41] M.A Kastner *Physics Today*. (1993) 24 – 27

[42] P. Bindu and S. Thomas *J. Theor. Appl. Phys.* **8** (2014) 123 – 134

[43] K. Ramakanth, Basic of Diffraction and Its Application. I.K. *International Publishing House* Pvt. Ltd, NewDehli (2007)

[44] C. Dewen and W. Suhua *Sci. China Ser. B* **39** (1996) 645 – 653

[45] T. Kippeny, L.A. Swafford, S.A. Rosenthal, *J. Chem. Educ.* **79** (2002) 1094 – 1100

[46] A.L. Efros and A.L. Efros, *Sov. Phys. Semicond.* **16** (1982) 772 – 775

[47] L.E. Brus, *J. Chem. Phys.* **79** (1983) 5566 – 5571

[48] L. Brus *J. Phys. Chem.* **90** (1986) 2555 – 2560

[49] E.O. Chukwuocha, M.C. Onyeaju and T.S.T. Harry, *World Journal of Condensed Matter Physics* **2** (2012) 96 – 100

[50] C.J. Murphy and J.L. Coffer, *Appl. Spectrosc.* **56** (2002) 16A – 27A

[51] R.R. Prabhu and M.A. Khadar *Pramana – J. Phys*. **65** (2005) 801 – 807

[52] S.K. Panda and C. Jacob *Appl. Phys. A.* **96** (2006) 805 – 811

[53] S.V. Gaponenko *Cambridge University Press, Cambridge* 1998

[54] H. Weller, *Curr. Opin. Colloid Interface Sci.* **3** (1998) 194 – 199

[55] J.Y. Fan, X.L. Wu, H.X. Li, H.W Liu, G.G Siu and P.K. Chu *Appl. Phys. Lett.* **88** (2006) 041909

[56] A. Tomasulo and M.V. Ramakrishna, *Submitted to J. Chem. Phys.* (2008)

[57] S. Shionoya and W.M. Yen Eds., *Phosphor Handbook*,CRC Press, Boca Raton, Fla, USA (1998)

[58] S. Talam, S.R. Karumuri and N. Gunnam *ISRN Nanotechnology* **2012** (2012) 1 – 6

[59] S.M. Soosen, L. Bose and K.C. George *SB Academic Review.* **XVI** (2009) 57 – 65

[60] J. Sinclair and D. Dagotto, *Solid State II Lecture Notes,* University of Tennessee, Knoxville (2009)

[61] L.F. Koao, F.B. Dejene and H.C. Swart, *Mater. Sci. Semicond. Process.* **27** (2014) 33 – 40

[62] O. Paris, C.H. Li, S. Siegel, G. Weseloh, F. Emmerling, H. Riesemeier, A. Erko and P. Fratzl *J. Appl. Cryst.* **40** (2007) S466 – S470

[63] A. Leonardi, M. Leoni and P. Scardi *Thin Solid Films.* **530** (2013) 40 – 43

[64] J.I. Langford and A.J.C. Wilson, *J. Appl. Cryst.* **11** (1978) 102 – 113

[65] A.K. Zak, W.H.A. Majid, M.E. Abrishami and R. Yousefi *Solid State Sci.* **13** (2011) 251 – 256

[66] P. Scherrer *Mathematish-Physikalische Klasse.* **2** (1918) 98 – 100

[67] A. Monshi, M.R. Foroughi and M.R. Monshi *W. J. N. S. E.* **2 (**2012) 154 – 160

[68] R. Yogamalar, R. Srinivasan, A. Vinu, K. Ariga and A.C. Bose, *Solid State Commun.* **149** (2009) 1919 – 1923

[69] K.D. Rogers and P. Daniels, *Biomaterials* **23** (2002) 2577 – 2585

[70] H. Klug and L. Alexander, *2nd Edition, John Wiley and Sons, New York* (1974)

3

Experimental procedure & characterization techniques

3.1 Introduction

ZnO nanoparticles were prepared using chemical bath deposition method (CBD). Several research techniques were employed to probe the thermal, structural, morphology, optical and luminescence properties of ZnO. Above mentioned properties were determined using Thermo Gravimetric Analysis (TGA), Differential Scanning Calorimetry (DSC), X-ray Diffraction (XRD), Scanning Electron Microscopy (SEM), Energy Dispersive Spectroscopy, Ultraviolet Visible spectroscopy (UV-Vis), Photoluminescence Spectroscopy (PL) and X-ray Photoelectron Spectrometer (XPS). The objective of this chapter is to provide a brief overview of the above mentioned techniques.

3.2 Chemical Bath Deposition (CBD)

A set of specific methods have been developed to synthesize ZnO, of which some of the following are commonly in use. The sol-gel method [1], it is a wet chemical technique used in the fabrication of metal oxides from a chemical solution, and this acts as a precursor for an integrated network (gel) of discrete particles. Hydrothermal method [2], in this method metal complexes are decomposed thermally either by boiling in an inert atmosphere or by using an autoclave with the help of higher temperatures (160- 280 ˚C [3]) and pressures (90 – 930 psi). Chemical bath deposition (CBD) [4], technique used in the present study is one of the useful solution methods for the preparation of compound semiconductors from aqueous solution. CBD is particularly suitable since it does not require high-pressure containers and is also entirely safe and environmentally friendly, because only water or alcohols is used as a solvent. The safety hazards of organic solvents and their eventual evaporation and potential toxicity are avoided using this method. This method is thus an increasingly important complement to other solution-based techniques in the fabrication of nanostructures.

3.2.1 Growth Mechanism

Despite the experimental simplicity, it is a complicated task to understand the mechanisms involved in the chemical bath process. The growth of zinc oxide (ZnO) using CBD is controlled mainly by the internal structure of the ZnO which is related to its crystallographic structure. In addition to that, the growth process which determines the final surface morphology is dependent on external parameters such as precursor solution, reaction time and reaction temperature.

In the chemical reaction for growing ZnO nanostructures, zinc acetate was used as the source of Zn^{2+} ions and thiourea was used as the alkali to provide the OH^- ions. Although the exact role of ammonia solution during the growth is still unclear, it is believed to act as a weak base (complexing agent) [5]. During the growth, the precursors start by undergoing the nucleation process after saturation point. This is followed by the successive dissolution and recrystallization process. Above processes depends on the nature of the reactive bulk solution in the vicinity of the ZnO crystals which is dependent on the time as well as the temperature of exposure of the solution. Many researchers indicated that formation of ZnO takes place through the decomposition of $Zn(OH)_2$ into ZnO [6 – 7]. The main reaction process for the formation of ZnO can be expressed by the following reactions in equations (3.1), (3.2) and (3.3) [8],

$$Zn \rightarrow Zn^{2+} + 2e^- \quad (3.1)$$

$$Zn^{2+} + 2OH^- \rightarrow Zn(OH)_2 + 2e^- \quad (3.2)$$

$$Zn(OH)_2 + 2OH^- \rightarrow Zn(OH)_4^{2-} \rightarrow ZnO + 2H_2O + 2OH^- \quad (3.3)$$

3.2.2 Synthesis procedure

When studying the "Effect of reaction time on structural, morphology and optical properties of ZnO nanoflakes prepared by chemical bath deposition method" the following synthesis procedure was followed. The ZnO powders were prepared by the chemical bath deposition method. The following starting materials such as zinc acetate ($Zn(O_2CCH_3)_2$), thiourea ($(NH_2)_2CS$) and ammonia (25 % NH_3) were used. All the precursors used for the

preparation of the nano-powders were of analytical grade. The sample solutions were prepared by dissolving 0.3 M of zinc acetate, 0.4 M of thiourea and also 98.8 ml of ammonia into deionized water. Then a magnetic stirrer was used to stir each of the mixtures overnight at room temperature to ensure homogenous distribution of the solution reagents. An equal volume ratio (1:1:1) was considered for each solution in the following order: 60 ml quantity of zinc acetate was first added to the test tube which was placed in the water bath, followed by addition of 60 ml of thiourea solution while stirring and finally 60 ml of ammonia solution was also added while continuously stirring.

Water bath was maintained to be at a constant desired temperature of 80 ℃ with continuous stirring of the solution for the different times. The ammonia (NH_3) solution was used as complexing agent. The white precipitates were then formed within 30 s after the solution was placed inside the water bath. The beakers were removed from the bath at various reaction time intervals (1, 3, 5, and 10 min). The solution was allowed to stabilize and cool down overnight in the lab at RT. Finally the solution was filtered and the dry precipitate was collected, washed several times with 60 ml of ethanol and 60 ml of acetone to remove the residue and desiccated for a maximum of three days to ensure that they are dried prior to characterization.

Similar experimental procedure was followed when trying to find "Moderate Zinc Acetate (ZnAc) Concentrations for the preparation of ZnO using Chemical bath deposition". The sample solutions were prepared by dissolving 0.1, 0.12, 0.14, 0.16, 0.18 and 0.2 M of ZnAc in 60 ml of H_2O, respectively, and 0.4 M of $((NH_2)_2CS)$ and also 98.8 ml of (25 % NH_3), were dissolved into 200 ml of deionized water, respectively. The beakers were removed from the bath after 10 minutes.

During the synthesis of ZnO nanostructures at various reaction temperatures for the article "Phase formation of Hexagonal wurtzite ZnO through decomposition of $Zn(OH)_2$ at various reaction temperatures using CBD method" the same procedure was followed. Four sets of samples were prepared under different CBD temperatures (55 ^{0}C, 65 ^{0}C, 75 ^{0}C and 80 ^{0}C). The resulting mixture was continuously stirred using rod-stirrer and the white precipitate was formed within 30 seconds while continuously stirring.

Lastly, the synthesis of ZnO nanostructures was also performed similarly at an 80 ℃ reaction temperature wherein one sample was prepared to study "The influence of annealing temperature on luminescence properties of ZnO nanopowders prepared by chemical bath deposition method". Furthermore the dried nanopowders were annealed in air at 300 ℃ and 600 ℃ prior to characterization.

3.4 Characterization techniques

In order to determine the temperature of possible decomposition and crystallization of the nanoparticles, the dried nanopowders were subjected to a (Perkin-Elmer TGA 7) thermogravimetric analyzer and (Perkin-Elmer DSC 7) differential scanning calorimeter. The crystal structures of the nanopowders were determined with two different XRD systems (Bruker AXS Discover and Bruker AXS D8 Advanced GmbH X-ray diffractometer) with CuKα (1.5418Å) radiation. Surface morphologies were studied using two different scanning electron microscopes (Shimadzu model ZU SSX-550 Superscan SEM model with EDS and JEOL J SM 7800F thermal field emission scanning electron microscope (FE-SEM)) by mounting the as-prepared nanopowders on conducting carbon tape. The chemical composition analysis was carried out using an Oxford Instruments AzTEC energy dispersive spectrometer (EDS), with X-Max80 silicon drift detector (SD D) system, attached to the FESEM. The optical measurements were carried out in the 200 to 800 nm wavelength range using a (Perkin Elmer UV/Vis Lambda) 20 powder Spectrophotometer. Luminescence measurements were done using four different PL systems (Varian Cary Eclipse fluorescence spectrophotometer with a monochromatized 150 W xenon lamp as an excitation source, mini-PL UV laser system 5.0 (Photon systems, USA), which uses a NeCu laser with an excitation wavelength of 248.6 nm, PL laser system 5.0 (Photon systems, USA), which uses a He-Cd laser with an excitation wavelength of 325 nm and Hitachi F-7000 FLUORESCENCE SPECTROPHOTOMETER respectively.

3.4.1 Thermogravimetric analysis (TGA)

TGA is the analytical method wherein the mass of samples is measured as a function of time or temperature while the sample is subjected to a controlled temperature program. It is usually used to ascertain the possible decomposition, degradation, crystallization, phase

change and thermal stability of materials during the heat treatment. These techniques consist of thermo-balance which is the main component, capable of measuring the sample mass as a function of temperature or time [9]. The changes in mass due to dehydration and oxidation can also be measured using TGA system. It is useful for compositional analysis of multi-component materials and used to examine the kinetics of the physio-chemical processes occurring in the sample [10 – 11].
The following properties of materials can be determined using the TGA technique:

1. The mass of metal catalyst impurity in as synthesized samples,
2. The number of functional groups in the sample and
3. The mass of reactive species absorbed by a functional group.

Quantitative determination of these properties is used to define the purity of the prepared material and the extent of their functionalization.

TGA spectrums were acquired using the Perkin Elmer TGA7 thermogravimetric analyzer, under nitrogen atmosphere at a flow rate of 20 ml.min^{-1}. The samples with mass (5-10 mg) were heated from 30 to 600 ºC at a rate of 10 ºC.min^{-1}.

3.4.2 Differential scanning calorimetry (DSC)

DSC is a quantitative technique used to measure the energy enthalpy changes of the system and heat capacity associated with phase transitions. The phase transition is the physical process in which changes like glass transitions, melting and crystallization occur when the sample or material is heated or cooled at a controlled rate [12]. DSC is used to monitor the amount of energy absorbed and released during the chemical reaction as a function of change in temperature. This system was discovered in 1962 by Emmett Watson and Michael O'Neill who were working for Perkin-Elmer Company [13]. It is used to measure the heat flow range which is meant to create phase diagram and gather thermo analytical information. The phase change obtained using DSC system can be either endotherm or exotherm. But if the DSC curve is constant that means there is no phase change in the sample.

Analysis of samples were carried out under nitrogen atmosphere (20 mlmin^{-1}) using a Perkin Elmer Pyris-1 differential scanning calorimeter from (Waltham, Massachusetts, U.S.A). The technique was calibrated using the onset temperatures of zinc and indium

standard and the enthalpy of indium. The sample masses in the range 5 – 10 mg were used and heated from 25 to 170 °C at the rate of (10 °Cmin^{-1}) and cooled to 25 °C at the same rate. The second scan was acquired under the same heating and cooling conditions. The peak temperatures of melting and crystallization including the melting and crystallization enthalpies were determined from the second scans to eliminate any thermal history effects.

3.4.3 X-ray Diffraction (XRD)

The X-ray diffraction (XRD) is a non-destructive analytical technique for identification and quantitative determination of crystalline phases present in powder and solid samples [14]. This useful technique was discovered by the German scientist by the name of Wilhelm Roentgen in 1895 and he was awarded the first Nobel Prize in Physics in 1901 [15]. It is well known as a common technique for the study of crystal structures, grain size, lattice constants, atomic spacing and degree of crystallinity in a mixture of amorphous and crystalline substances [16]. XRD system uses monochromatic X-ray generated inside cathode ray tube to gather information. X-rays are produced when high-energy charged particles, such as electrons are accelerated and collide with a metal target, for example, Cu. The resulting X-ray are collimated and directed onto the sample. As the sample and detector are rotated the intensity of the reflected X - rays are recorded. When the geometry of the incident X-rays striking to the sample satisfies the Bragg law, constructive interference occurs and characteristic diffraction peak of the sample will be observed [17].

The waves of the x-rays incident to the crystal compound create an oscillating electric field that interacts with electrons of the compound atoms. The electrons coherently scatter the incoming electromagnetic radiation. Diffraction occurs when the atoms arranged in a periodic array scatter radiation at specific angles [18]. The incident angle of the X-rays is equal to that of the reflected rays. The relationship of the angle and wavelength of the diffracted X-rays in terms of reflection by the crystal planes is determined by Bragg's law equation (3.4),

$$n\lambda = 2dSin(\theta) \tag{3.4}$$

where λ is the wavelength of the incident light rays, θ is the angle of incidence, and d represents the inter-planar spacing that sets the difference between the path and length for the rays scattered from the top plane and the rays scattered from the next plane parallel to the top one.

3.4.4 Scanning electron Microscopy (SEM)

The scanning electron microscope (SEM) is a surface technique that is essentially designed to characterize the size, shape and morphology of samples by scanning it with a high-energy beam of electrons in a raster scan pattern [19]. This technique is equipped with an electron gun, secondary electrons detector, BS detector, and a specimen holder. These important components are enclosed inside the vacuum chamber. The electrons interact with the atoms on the sample producing signals that contain information about the sample's surface topography and composition. Secondary and backscattered electrons that come from the specimen surface when it is irradiated by primary electrons from the electron gun within the system are employed to produce specimen images. From secondary electron images we obtain topographic contrast while backscattered electron images are used to extract compositional differences on the surface [20]. The SEM technique can operate in connection with energy dispersive spectroscopy (EDS).

In a distinctive SEM system, an electron beam is emitted from an electron gun fitted with a tungsten filament cathode and these emitted electrons are directed and focused on the sample by using an anode and various electromagnetic lenses between the electron gun and sample. These projected electrons eject secondary and back scattered electrons when hitting the sample. The ejected secondary and back scattered electrons from the sample are transferred into electronic signal which is sent to the viewing screen, producing an image.

3.4.5 Energy Dispersive Spectroscopy (EDS)

However, the images from the SEM cannot definitively prove that the obtained nanostructures actually consist of ZnO. Such information can be obtained from EDS, which is most commonly attached to the SEM as explained above. EDS technique is useful in identifying materials and contaminants, as well as estimating their relative concentrations on the surface of the specimens. During EDS analysis, the specimen is irradiated with an electron beam inside the SEM. The bombarding electrons collide with the specimen atoms own electrons, knocking some of them off in the process. A position vacated by an ejected inner shell electron is eventually occupied by a higher - energy electron from an outer shell. Thus, by measuring the amounts of energy present in the X - rays being released by a

specimen during electron beam bombardment, the identity of the atom from which the X-ray was emitted can be established.

3.4.6 Ultraviolet Visible spectroscopy (UV-Vis)

UV-vis spectroscopy is the technique used to measure the attenuation of a beam of light after it has passed through the sample or after reflection from a sample surface. It is well known that the ultraviolet (UV) region ranges from 200 to 400 nm and the visible (Vis) region extends from 400 to 800 nm. It is useful to characterize the absorption, transmission, and reflectivity of variety of technologically important materials, such as pigments, coating, windows and filters [21]. In absorption spectroscopy the amount of light that is absorbed is measured as a function of wavelength. Both qualitative and quantitative information can be obtained from the sample using this method.

Fundamentally, the spectrophotometer (single beam) consists of the following elements: a light source (usually a deuterium lamp for the UV spectral range and a tungsten lamp for the VIS and IR spectral ranges). In operation light source is focused on the entrance to a monochromator, which is used to select a single frequency wavelength from all those provided by the lamp source and scan over a desired frequency range, a sample holder, followed by the light detector (usually a photomultiplier for the UV-VIS range and a SPb cell for the IR range) to measure the intensity of each monochromatic beam after crossing the sample. Lastly, this system consists of a computer to save the reflectance/absorption spectrum [22].

3.4.7 Photoluminescence Spectroscopy (PL)

Photoluminescence spectroscopy (PL) is a powerful contactless, nondestructive technique of physically probing the electronic structure of materials. PL is a very useful technique to disclose the efficiency of charge carrier trapping, immigration and transfer in a semiconductor [23]. The process of photoluminescence can be achieved using a laser, a xenon lamp or synchrotron radiation to generate the electron hole pairs in the structure of a sample, and the light from the source is focused to the sample using lenses. The results obtained from detected emission are displayed as PL intensity as a function of the emitted light wavelength. Generally, the photoluminescence emissions on semiconductor materials

originate from the radiative recombination of photo-generated electrons and holes. The two major photo-physical processes can give rise to photoluminescence signals. From PL measurement, we can obtain a variety of material parameters, which includes band gap determination, Impurity levels and defect detection, recombination mechanisms [24]. There are so many advanced PL spectroscopy techniques which can be used to measure photoluminescence, photoluminescence excitation centers and phosphorescent lifetimes. Within these techniques we have "Hitachi F-7000 FLUORESCENCE SPECTROPHOTOMETER" which uses xenon lamp as a source of excitation. The schematic diagram for this system is presented in **Figure 3.1** presenting the signal processing and control System [25].

3.4.7.1 Operating principle

Signal processing and Control System

The light emitted from the Xe lamp enters the excitation side monochromator, and part of the light from this monochromator is directed to the monitor detector by the beam splitter. All of the drive components including wavelength motor, slit control motor and chopper motor, are operated via signal from the computer. Output signals from the monitor detector and fluorescence measuring detector (Photomultiplier) go through the A/D converter and are processed by the computer, and then sent to the PC.

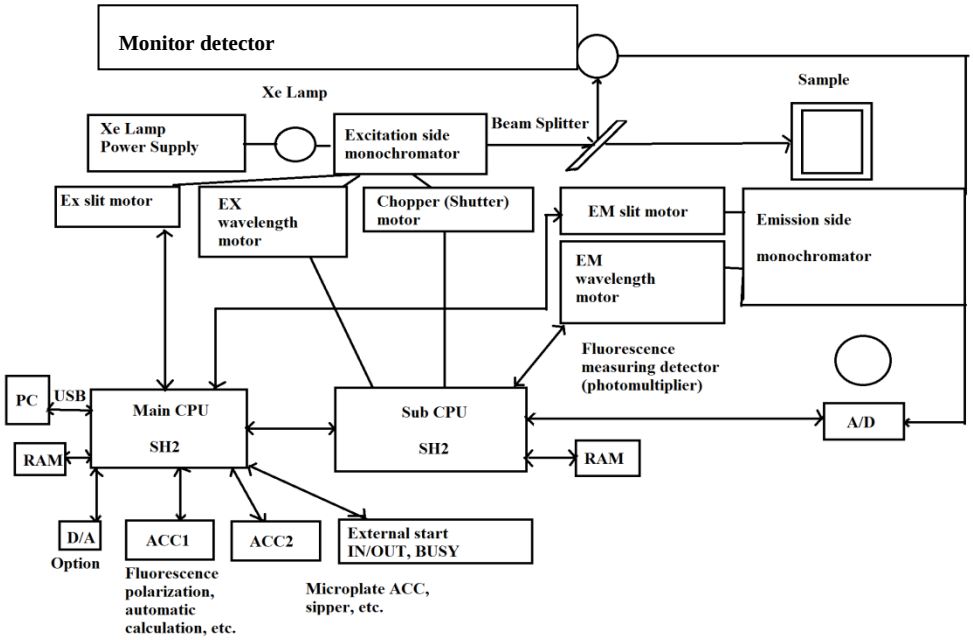

Figure 3.1 Schematic diagram of the PL system at UFS (Qwaqwa campus) - (Signal Processing and Control System).

3.4.8 X-ray Photoelectron Spectroscopy (XPS)

X-ray photoelectron spectroscopy (XPS) is a surface analytical technique well known as electron spectroscopy for chemical analysis (ESCA) which makes use of photo-ionization effect [26]. XPS aims at characterizing elemental composition, chemical state and the electronic state of the elements on the specimen surface. In principle, when an X-ray beam illuminates the surface of a specimen, the core electron of an atom on the surface will absorb the entire X-ray photon energy. If the X-ray photon energy is higher enough, the core electron will then escape from the atom and emit out of the surface with certain kinetic energy called photoelectron. This technique is capable of simultaneous measuring of the kinetic energy (E_k) and number of electrons that escape from 1 - 10 nm of the material surface being analyzed. The kinetic energy E_k of these photoelectrons can be determined by the X-ray photon energy ($h\nu$) and the respective binding energies (E_b) in equation (3.5):

$$E_k = h\nu - E_b \tag{3.5}$$

The energy carried by a particular wavelength is equal to a known, and the electron binding energy (BE) of emitted electrons can be measured using an equation (3.6):

$$E_b = h\nu - E_k - \phi \tag{3.6}$$

and the binding energy is that of an electron emitted by electron configuration within the atom, the photon energy being that of the X-ray used, kinetic energy is that of the photoelectron and ϕ is the work function of the detector [27]. The binding energy of each atom is unique; hence the energy peaks of different atoms have different energy positions.

XPS PHI 5000 versa probe using 100 µm, 25 W and 15 kV Al monochromatic x-ray beam was used to analyze the samples. It is a very sensitive system to the point that it can identify almost all elements except hydrogen (H_2) and helium (He) by measuring the binding energy of its core electron. (H_2) and (He) cannot be detected by XPS because their electrons come from the valence band. This causes them not to have unique energy peaks [28 – 29].

3.5 References

[1] M. Ohyama, H. Kozuka and T. Yoko, *Thin Solid Films* **306** (1997) 7885

[2] B. Weintraub, Z. Zhou, Y. Li and Y. Deng *Nanoscale* **2** (2010) 1573 – 1587

[3] W.L. Suchanek, *J. Cryst. growth* **312** (2009) 100 – 108

[4] L. Vayssieres *Adv. Mater.* **15** (2003) 464 – 466

[5] L.F. Koao, F.B. Dejene, R.E. Kroon and H.C. Swart, *J. Lumin.* **147** (2014) 85 – 89

[6] S. Baruah and J. Dutta *Sci. Technol. Adv. Mater.* **10** (2009) 1 – 18

[7] Z. Lockman, Y.P. Fong, T.W. Kian, K. Ibrahim, K.A. Razak *J. Alloys Compd.* **493** (2010) 699 – 706

[8] S. Sreekantan, L.R. Gee and Z. Lockman *J. Alloys Compd.* **476** (2009) 513 – 518

[9] M.A. Sibeko and A.S. Luyt *M.Sc thesis* University of the Free State, RSA (2012)

[10] M. Fan and R.C. Brown, *Energy and Fuels* **15** (2001) 1414 – 1417

[11] M.E, Brown *Chapman & Hall*, London (1988)

[12] E.L. Charstey and S.B. Warrington *Royal Society of Chemistry*: Cambridge (1992)

[13] E. Watson, M. O'Neill, J. Justin and N. Brenner, *Anal. Chem.* **36** (1964) 1233

[14] R. Jenkins, and R.L. Snyder *John Wiley & Sons, N.Y* **138** (1996) 1 – 322

[15] G. Crundwell, J. Phan, and K.A. Kantardjieff *J. Chem. Ed.* **76 (**1999) 1242 – 1245

[16] G. Cao *6th edition*, London (2004)

[17] B.M. Mothudi *PhD thesis* University of the Free State, South Africa (2009)

[18] M.A. Prelas, G. Popouci and L.K. Bigelow CRC Press (1998)

[19] J.I. Goldstein and H. Yakowits *Plenum Press*, London (1977)

[20] S.J.B. Reed, *2nd edition*, Cambridge Press, New York (2005)

[21] P.A. Moleme, *MSc thesis*, University of the Free State, Republic of South Africa (2011)

[22] Skoog, Holler and Crouch, *6th edition* Thomson Brooks/Cole: Belmont, CA **351** (2007)

[23] Y. Cong, J. Zhang, F. Chen and M. Anpo, *J. Phys. Chem. C* **111** (2007) 6976 – 6982

[24] Photoluminescence spectroscopy (Online) http://www.itst.ucsb.edu/~vinhnguyen/Time-Frequency_Spectroscopy.htm (Accessed 17 September 2014)

[25] Hitachi F-7000 FLUORESCENCE SPECTROPHOTOMETER manual

[26] D.J. O'connor, B.A. Sexton and R.St.C. Smart, *Springer-Verlag*, Heidelberg (1992)

[27] C.D. Wagner, W.D. Riggs, L.E. Davis, *et al*, *Perkin-Elmer Corp*. Eden Prairie, MN, USA (1979)

[28] D .Briggs and M.P. Seah *John Wiley & Sons* Ltd (1993)

[29] N.M.K. Lamba, A.K. Woodhouse, S.L. Cooper *CRC Press* (1997) 101

4

Phase formation of Hexagonal wurtzite ZnO through decomposition of $Zn(OH)_2$ at various reaction temperatures using CBD method

4.1 Introduction

Most recently, the study on the luminescence behavior of the hexagonal wurtzite structure of ZnO has attracted vast attention owing to its unique structural, optical, thermal, electrical, and luminescence properties which can be exploited to manufacture promising phosphor materials [1 – 4]. Within various disciplines of nano-research, the control of structure and morphology has always been under extreme focus due to nanomaterials properties which are usually size, shape and distribution dependent [5]. The dependence of ZnO properties on the size and shape of the nanoparticles contributes towards various applications, such as ultraviolet (UV) photodiodes [6], spin light emitting diodes [7] and solar cells [8]. ZnO is the key inorganic material with novel applications in the field of nanoscience and nanotechnology. Furthermore, the n-type semiconductor has many interesting applications because of its optical transparency in the visible region [9]. It is well known that ZnO has three stable structures, namely cubic rock-salt, zinc-blende and hexagonal wurtzite [10]. Among all metal oxide semiconductors ZnO is important both scientifically and industrially due to its wide band gap of 3.37 eV, and large exciton binding energy of 60 meV at room temperature (RT) [11 – 12].

Numerous synthetic methods like sonochemistry [13], combustion method [14], sol-gel method [15], and hydrothermal process [16] have been used to prepare ZnO nanoparticles at high reaction temperatures. Some of these synthetic processes usually require long reaction time, high temperature and some are not good with quality control [17]. To avoid some of these challenges CBD method was used to prepare ZnO at low reaction time and temperature. CBD is one of the best solution phase methods for synthesis of compound semiconductors [18]. It is easy, cheap and user friendly because one can be able to vary parameters such as PH, time, concentration and temperature [19]. The influence of the reaction temperature on

the properties of ZnO has been reported by several research groups [20 – 21]. Kumar S *et al.* [22] indicated that structure, morphology and luminescence properties of ZnO strongly depend on the reaction temperature using hydrothermal route. Pawar B.N *et al.* [23] observed only the strong near-band edge UV absorption at RT UV-vis results using the low temperature CBD approach. The phase change in ZnO at different reaction temperatures has never been reported before using CBD method to the best of our knowledge.

Therefore, the present study aims at preparing ZnO phosphor using CBD method at various reaction temperatures. Agglomerated flakes-like particles were observed. The effect of these particles on the structure, optical and luminescence properties was investigated as the reaction temperature increases. The novelty in this study lies in the enhancement of the ultraviolet-blue emission which is of great potential in light emitting and biological fluorescence labelling applications. Due to advances in nanotechnology, it is valuable to develop a phosphor material in the nano regime to absorb any form of energy and convert it to visible light.

4.2 Results and discussions

4.2.1 TGA analysis

Figure 4.1 shows TGA curves that display the thermal behaviour of ZnO nanophosphors prepared at different reaction temperatures. ZnO nanophosphors were found to undergo five degradation processes. Initially all the samples degrade partially about ~ 2 % weight loss from 50 – 90 ℃ due to evaporation of ethanol as the most volatile compound used. This primary weight loss is followed by ~ 4 % loss in the temperature range 90 – 150 ℃ as the result of the dehydration of water, but sample prepared at 55 ℃ extends to 175 ℃ as compared to the others. Between 180 – 200 ℃ it was observed that ~ 10, 12, 13 and 16 % weight losses corresponding to samples prepared at 55, 65, 75 and 80 ℃, respectively. These distinct weight losses were attributed to degradation of unreacted acetate ions. Thus it can be clearly seen that acetate ions degradation increased with the increase in reaction temperature and this can possibly be due to well dissolved zinc acetate at high reaction temperatures. From 200 – 250 ℃ all TGA spectrums revealed ~ 3 % gradual weight loss assigned to the thermal decomposition of ammonia. Finally the observed 4 % weight loss through all the spectrums in the temperature range 252 – 430 ℃ is mainly due to phase transformation from

$Zn(OH)_2$ to ZnO [24 – 25]. The weight loss processes ceased at ~ 430 ℃ and the stable residues that extends to 700 ℃ was ascribed to crystallization of ZnO. The residual masses during crystallization of material decreased from sample prepared at 55 ℃ throughout to sample prepared at 80 ℃. These decreases in the residual masses might be due to decreased organic species with increase in the reaction temperature. Samples prepared at 65 and 75 ℃ have moderate thermal stability compared to sample prepared at 55 ℃. However, the thermal stability of the ZnO prepared at 80 ℃ was slightly better than the rest, indicating that the increase in reaction temperature increased the thermal stability of ZnO. Khan *et al.* [26] reported decomposition of $Zn(OH)_2$ into ZnO for the sample prepared at 70 ℃ in agreement with XRD results.

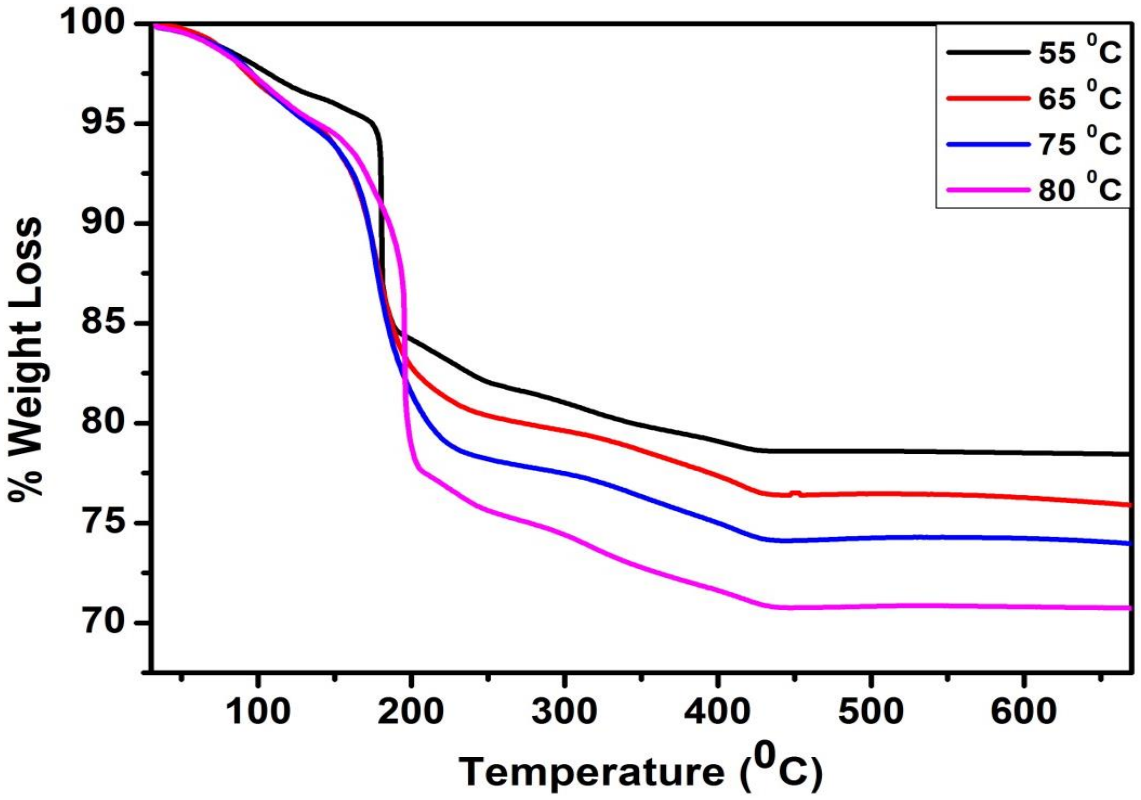

Figure 4.1 TGA curves of thermal decomposition of ZnO nanophosphors prepared by CBD method at different reaction temperatures.

4.2.2 DSC analysis

Figure 4.2 shows DSC endotherm curves of ZnO nanophosphors prepared by CBD method at different reaction temperatures. The melting and onset temperatures including peak enthalpies from DSC together with percentage weight loss and residual mass percentage from

TGA are summarized in **Table 4.1**. The melting temperature significantly decreases while the melting enthalpy increases with an increase in the reaction temperature. There is still some controversy on why the sample prepared at 65 ℃ showed increased melting temperature and decreased peak enthalpies in contrast to the behaviour of other samples. The curves in **Figure 4.2** confirm the decrease in the melting peak temperature as the reaction temperature increases. The decrease in melting temperature can be assigned to reactivity of acetate ions at high temperature which reduces packing of the atoms and inhibit the crystallization of ZnO [27]. The intensity of the endothermic peaks decreases with the increase in the reaction temperature but increased to the optimum level for the sample prepared at 80 ℃. The sample prepared at 80 ℃ has highest endothermic because it is well crystallized compared to the others.

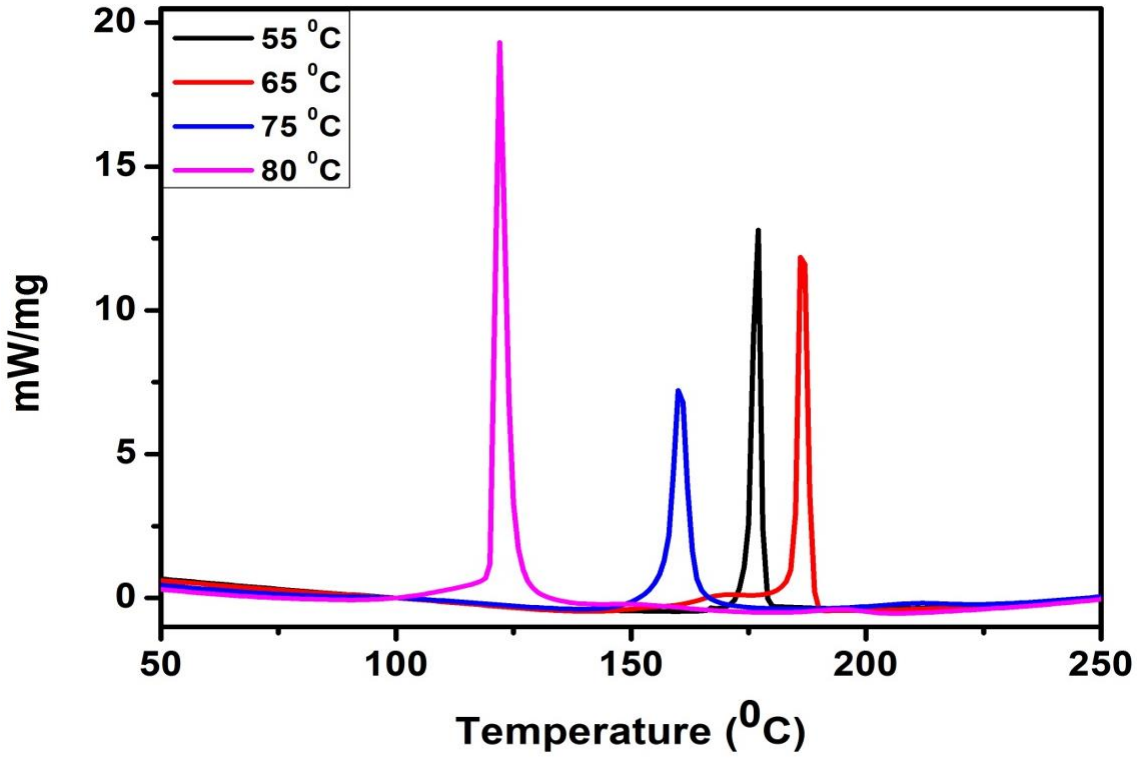

Figure 4.2 DSC endotherm curves of ZnO nanophosphors prepared by CBD method at different reaction temperatures.

Table 4.1 Summary of DSC heating results for all investigated ZnO samples and TGA % loss.

Samples	T_m / ℃	ΔH_m / J g^{-1}	Onset T_o/ ℃	Total W.L %	Residue %
ZnO (55 ℃)	176.73	192.49	175.16	21.520	78.566
ZnO (65 ℃)	186.50	191.65	184.82	23.661	76.538
ZnO (75 ℃)	160.37	227.53	157.64	25.811	74.274
ZnO (80 ℃)	122.03	409.35	120.39	29.226	70.858

4.2.3 XRD analysis

Figure 4.3 (a) represents the XRD pattern of the ZnO nanophosphors prepared by controlling the reaction temperature, from 55 ℃ to 80 ℃ respectively.

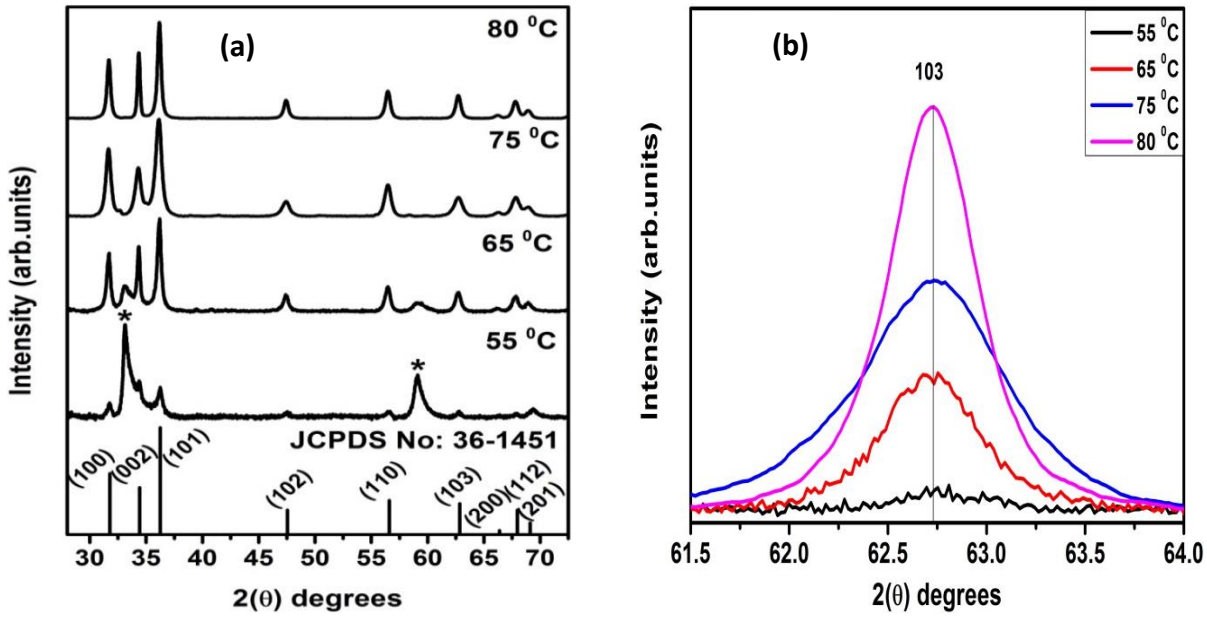

Figure 4.3 (a) XRD spectra of ZnO nanophosphors prepared by CBD method at different reaction temperatures, **(b)** Detail of the (110) peak.

Two different phases were obtained at low and high reaction temperatures. At low reaction temperature 55 ℃ there are mainly three diffraction peaks at 2θ values 33.5^0, 59.5^0, and 69.6^0 marked with asterisks (*) which are indexed to $Zn(OH)_2$ phase with data from JCPDS card no. (38-0356). It can be clearly seen that by increasing the reaction temperature to 65 and 75 ℃ the $Zn(OH)_2$ peaks diminishes while ZnO peaks prevails. The sample prepared at

maximum reaction temperature 80 ℃ reveals nine diffraction peaks around 31.8^0, 34.5^0, 36.4^0, 47.5^0, 56.2^0, 62.9^0, 66.4^0, 68.0^0 and 69.1^0 corresponding to ZnO phase. This nine diffraction peaks indexed to hexagonal wurtzite structure of ZnO are in agreement with data from JCPDS card no. (36-1451) with lattice constants a = 3.249 Å and c = 5.206 Å.

Lattice constants a = 3.240, 3.257, 3.259 and 3.261 Å and c = 5.193, 5.217, 5.223 and 5.224 Å corresponding to 55, 65, 75 and 80 ℃ reaction temperatures were estimated from (100) and (002) diffraction peaks. The above estimated lattice constants slightly increased as the reaction temperature increases and they respectively match with hexagonal wurtzite ZnO lattice constants. Despite this diffraction peaks no additional characteristic peaks corresponding to precursors such as zinc acetate were observed, which shows the formation of pristine ZnO at high reaction temperature 80 ℃. These results indicate that temperature played an important role in the formation of hexagonal wurtzite ZnO crystal structure. Furthermore, the average crystalline size was estimated using Debye Scherrer's equation (4.1) [28],

$$D = \frac{0.9\lambda}{\beta Cos(\theta)} \tag{4.1}$$

with the full width at half maximum (FWHM) at the line broadening of (100), (002), (101), (102), (110) and (103) reflections for the samples prepared at 65, 75 and 80 ℃ temperatures. In equation (4.1) λ represents the wavelength of Cu-Kα which is equal to 1.5406 Å, β is the (FWHM) in radians, θ is the Bragg's diffraction angle in degrees. The estimated average crystal sizes in nm were 23.9, 17.0 and 24.1 corresponding to 65, 75 and 80 ℃ reaction temperatures respectively. The estimated crystalline size fluctuates as reaction temperature increases and increased to maximum at highest reaction temperature of 80 ℃ due to narrowing of diffraction peak.

Kumar *et al.* [20] observed an increase in average particle size when increasing temperature of Teflon (hydrothermal synthesis). The intensity ratio, $I_{(002)}/I_{(101)}$ of the peaks presenting (002) and (101) is equal to 0.70 which is higher than the corresponding standard value of 0.44 of bulk hexagonal wurtzite ZnO [29]. This ratio determines the preferred orientation of ZnO structure [30]. From **Figure 4.3 (a)** it is clearly seen that all diffraction intensities for sample prepared at 75 ℃ match perfectly with reference data from JCPDS card no. (36-1451). But (002) diffraction intensity for samples prepared at 65 ℃ and 80 ℃ does not match with the

reference data. This may be due to high intensity ratio 0.70, thus in our results ZnO prefers (002) orientation. From **Figure 4.3 (b)** the (103) orientation reveals a tiny shift to the lower diffraction angle when the reaction temperature increases. This corresponds to the increase in lattice spacing as $Zn(OH)_2$ decomposes into the ZnO. Furthermore, the diffraction peak becomes narrower and intense. Thus, increasing the reaction temperature improved crystallinity of ZnO. **Figure 4.4** represents XRD diffraction spectra of ZnO prepared at 55 ℃ with two phases presented with two different JCPDS standard cards as explained in **Figure 4.3(a)**.

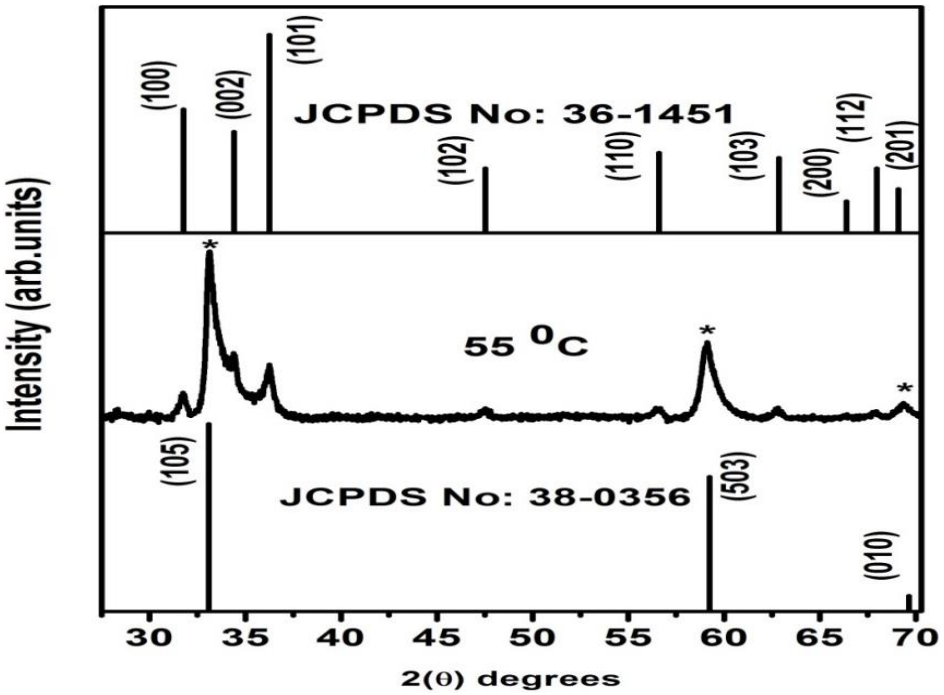

Figure 4.4 ZnO nanophosphors prepared at 55 ℃ with JCPDS cards corresponding to observed diffraction peaks.

4.2.4 SEM analysis

The surface morphology of the ZnO nanophosphors, prepared by CBD method under low and high reaction temperature conditions, analyzed by SEM is shown in **Figure 4.5 (a)** and **(b)**. The SEM images clearly indicate that there are variations in the surface morphology of ZnO nanophosphors depending on the reaction temperature. The SEM image in **Figure 4.5 (a)** demonstrates incomplete non-uniform flakes highly agglomerated around the spherical nanoparticles. It is interesting to observe that the spherical nanoparticles disappeared when

the reaction temperature is 80 ℃ and fully flakes-like morphology remains as shown in **Figure 4.5 (b)**. It can be noted that the sphere-like structures accumulates and stack on each other to give the overall appearance of flake-like morphology [31]. Hence at 80 ℃ the nanoflakes are uniform. The results illustrate that temperature acts as a structure-directing parameter, significantly gathering sphere-like structures together to form flakes-like structure. The formation of flakes-like morphology can be attributed to the increase in the reaction temperature of ZnO nanophosphors.

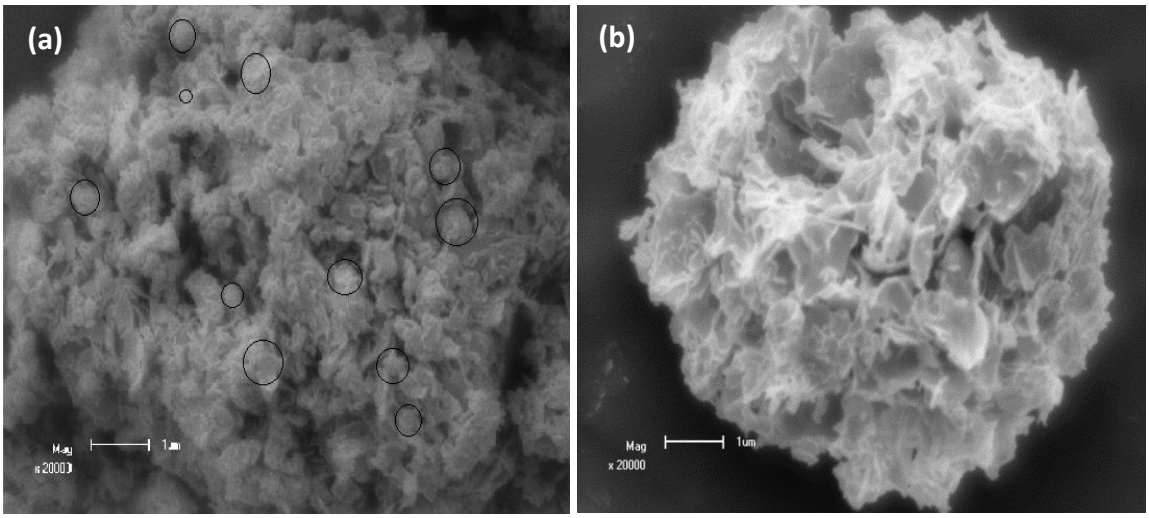

Figure 4.5 SEM images of ZnO nanophosphors prepared using CBD method at different reaction temperatures **(a)** 55 ℃ and **(b)** 80 ℃.

Furthermore, the observed change in XRD structure wherein $Zn(OH)_2$ decomposed into hexagonal wurtzite which agrees with the observed morphology. Nevertheless, the mechanism for the formation of nanoflakes at different reaction temperatures can be clearly explained by chemical process of CBD. It was anticipated that at longer reaction temperature nanoparticle growth would occur leading to change in surface morphology. Sreekantan *et al.* [32] obtained ZnO with different morphologies from spherical nanoparticles to nanoflakes. Thus the observed spherical nanoparticles are expected to be the building blocks in the formation nanoflakes morphology. It is believed that the radius of the small spherical nanoparticles increases linearly with reaction temperature. As the spherical nanoparticles grow, there is an increase in the phase boundaries and the nanoparticles comes into contact with one another, thus forming well pronounced nanoflakes morphology. In terms of morphology, Adnan *et al.* [33] reported nanoflakes of almost the same size being the key factor influencing the efficiency of ZnO. Guzman *et al.* [34] observed the change in

morphologies of synthesized ZnO from flake like to flower like morphologies using aqueous precipitation method at 60, 70 and 80 ℃ of reaction temperature.

4.2.5 EDS analysis

Figure 4.6 Shows chemical stoichiometry of ZnO nanophosphors prepared at 55 and 80 ^{o}C reaction temperatures. The results presented in **Figure 4.6 (a)** and **(b)** shows that the prepared material contains Carbon (C), O and Zn elements. The observed C was probably coming from the adventitious carbon which comes from the atmosphere and the conducting carbon tape used to mount the samples. Apart from those elements no other impurities are present in the sample. In **Figure 4.6** at the top right corners there is a bar graph comparing the weight % of elements in the samples. The concentration of Zn and O are ~ 77 and ~ 23 % in **Figure 4.6 (a)** while the concentrations of Zn and O are ~ 80 and ~ 20 % in **Figure 4.6 (b)**, respectively. When comparing both samples prepared at 55 and 80 ℃, it is clear that the amount of Zn increased while O decreased with an increase in the reaction temperature.

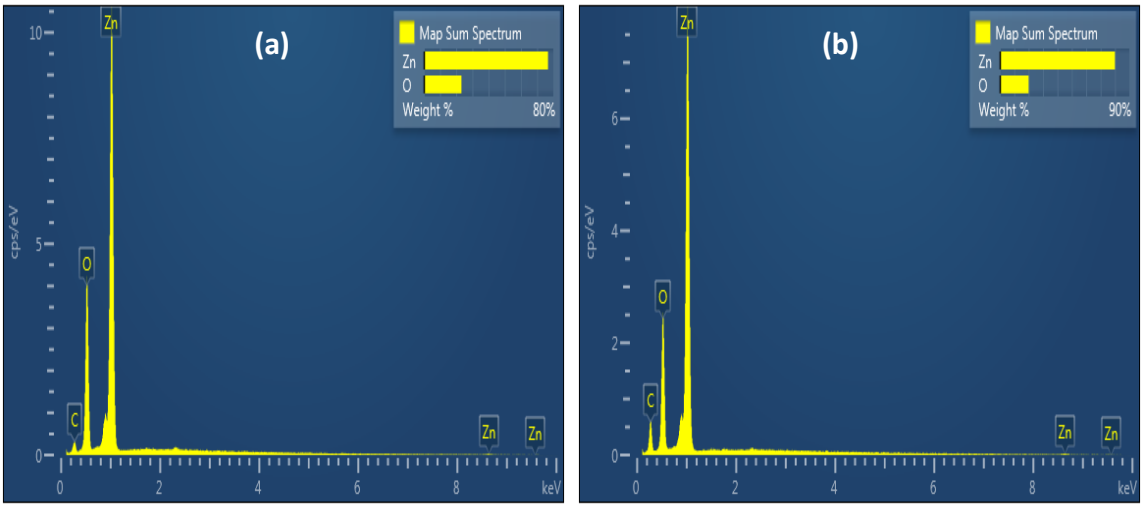

Figure 4.6 EDS spectra of ZnO nanophosphors prepared using CBD method at **(a)** 55 and **(b)** 80 ℃ reaction temperatures.

8.2.6 Reflectance analysis

UV-vis spectroscopy is a technique used to determine the optical properties of nanoparticles. The reflectance spectrum of ZnO nanophosphors recorded as the function of wavelength in the wavelength range 200 - 800 nm prepared at different reaction temperatures is shown in

Figure 4.7. It is evident that all the nanophosphors exhibit an absorption edge at about ~ 370 nm and this edge shifts slightly to the higher wavelength with an increase in the reaction temperature. The absorption edge at around ~ 370 nm is assigned to intrinsic band-gap absorption of ZnO due to the electron transitions from the valence band to the conduction band ($O_{2p} \rightarrow Zn_{3d}$) [35].

Furthermore this red shift indicates the shrinkage effect in the band gap energy. Jaber *et al.* [36] obtained ZnO which exhibit high absorption band in the UV region (wavelength ≤ 380 nm). The percentage reflectance of the ZnO nanophosphors in the visible is found to decrease considerably from 94 % to 80 % when the reaction temperature is increased from 55 ℃ to 80 ℃. Thus the loss in the percentage reflection suggests that this material can be suitable for anti-reflection coating because material absorb more with the increase in reaction temperature [37].

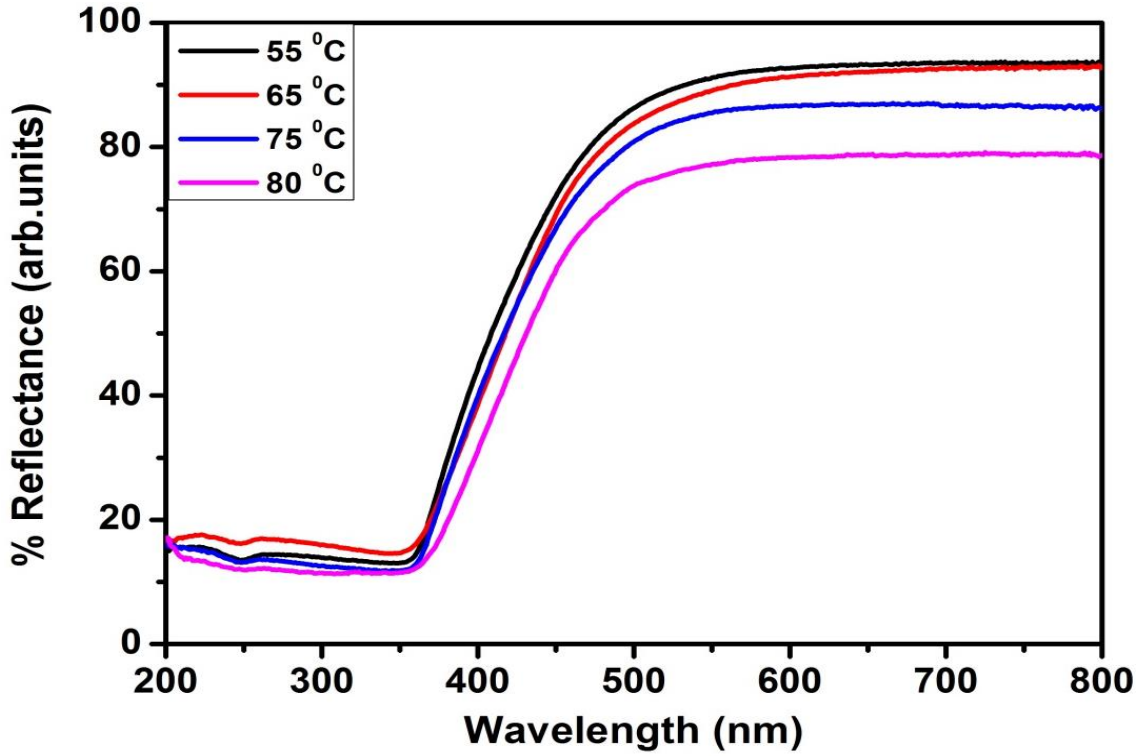

Figure 4.7 UV-vis reflectance spectrum of the CBD synthesized ZnO nanophosphors at different reaction temperatures.

Figure 4.8 represents the relationship $(Khv)^2$ versus (hv) from which the optical band gap of the nanophosphors was determined by extrapolating the linear part of the spectrum. Equation (4.2) is used to perform the Kubelka−Munk transformation of diffuse reflectance.

$$K = \frac{(1-R)^2}{2R} \tag{4.2}$$

From equation (4.2) K is the reflectance transformed according to Kubelka−Munk, h is Planck constant, v is the light frequency, and R is reflectance (%) [38 – 39].

Figure 4.8 represents the plot of $(Khv)^2$ versus (hv) for ZnO nanophosphors prepared at 55, 65, 75 and 80 ℃ reaction temperatures which produced values of energy band gap of 3.27, 3.24, 3.20 and 3.15 eV. Thus the band gap energy of zinc oxide was found to be dependent on the reaction temperature because it decreased with the increase in the reaction temperature. Kathalingam *et al.* [18] also observed a decrease in band gap energy of ZnO as the reaction temperature increases using CBD method.

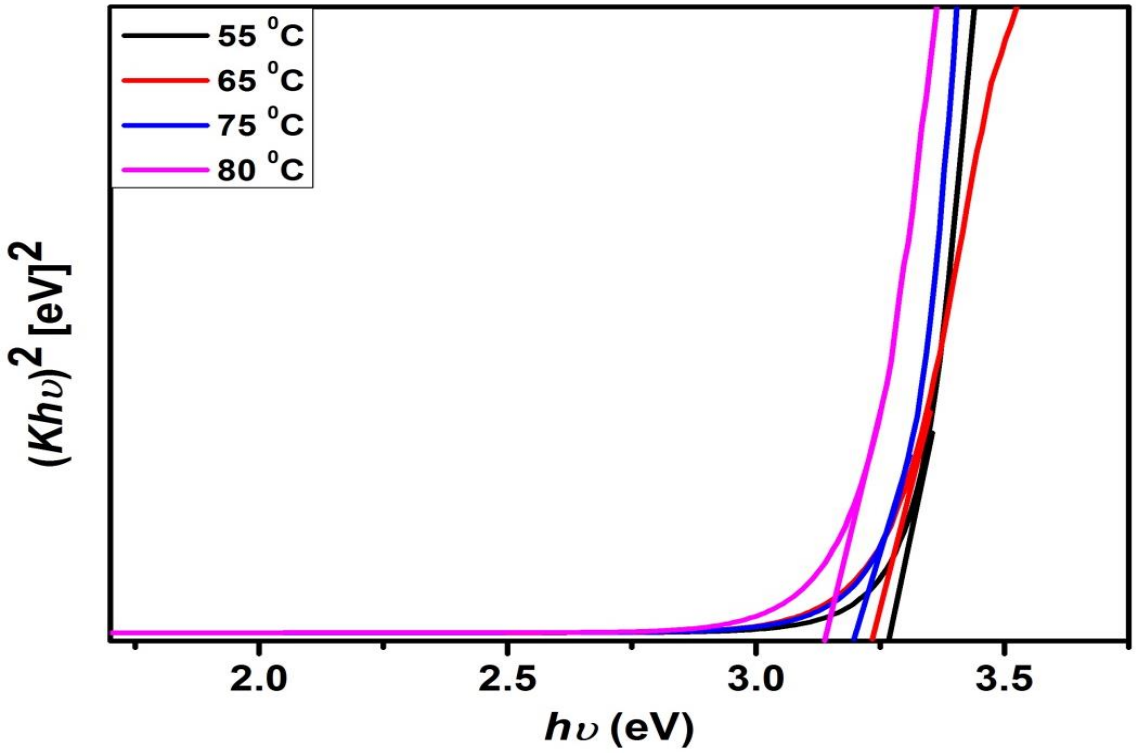

Figure 4.8 Plot to determine the band gap energy of flower-like ZnO nanophosphors prepared by CBD method at different reaction temperatures using relationship $(K * hv)^{1/2}$ = f(hv).

The effective mass model was used to derive equation (4.3) [40], used to calculate the particle size.

$$r(nm) = \frac{-0.3049\sqrt{-26.23012 + \frac{10240.72}{\lambda_p(nm)}}}{-6.3829 + \frac{2483.2}{\lambda_p(nm)}} \tag{4.3}$$

From UV – Vis reflectance spectra in **Figure 4.7**, the particle size was determined using equation (3) where λ_p (nm) indicates the wavelength of the absorption edge. The obtained particle sizes are 6.90, 8.10, 11.6 and 17.4 nm corresponding to 55, 65, 75 and 80 ℃ reaction temperatures. It can be clearly seen that the particle size increases with the increase in the reaction temperature. The increase in particle size is a result of red shift in the absorption edge due to decreasing quantum confinement [41]. Soosen *et al.* [42] also observed the increase in the particle size when the temperature increases. As a result it can be concluded that the energy band gap decrease as the particle size increases and this is also in good agreement with confinement effects of nanoparticles.

4.*2.7 Photoluminescence Analysis*

Figure 4.9 (a) shows the PL spectra of ZnO prepared at different reaction temperatures. The broad deep level emission that starts from UV to the visible region (350 – 800 nm) with the maximum peak at ~ 475 nm is observed.

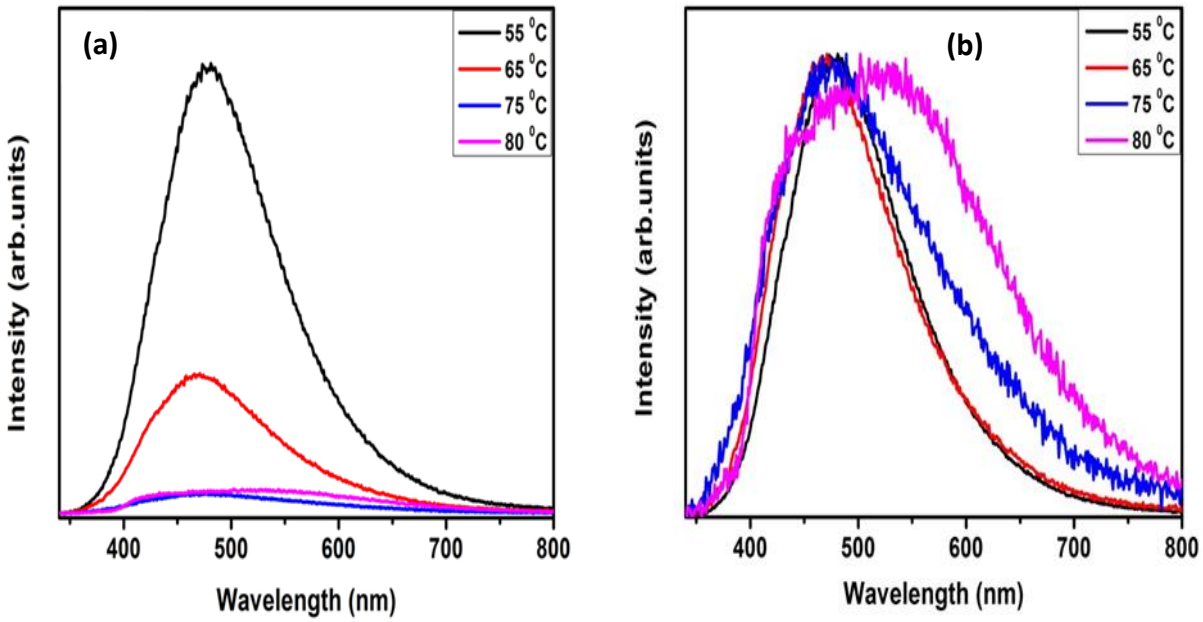

Figure 4.9 (a) PL spectra of ZnO prepared at different reaction temperatures, **(b)** Normalized temperature dependent PL emission spectrum of ZnO nanophosphors prepared at different reaction temperatures.

The PL emission intensity for the sample prepared at 55 ℃ reaction temperature was the maximum. The decline in PL emission intensity was observed when increasing the reaction

temperature to 65 ℃. The luminescence efficiency decreased further with the increase in reaction temperature whereby we observed slightly equal intensities for samples prepared at 75 and 80 ℃. The blue emission at ~ 475 nm is assigned to $Zn(OH)_2$ as confirmed by XRD and TGA results. Thus, the sudden decrease in luminescence intensity may be due to the decomposition of $Zn(OH)_2$ into ZnO. Florica *et al.* [43] attributed the quenching of luminescence emission to dehydration of $Zn(OH)_2$ during formation of ZnO when using chemical methods including CBD.

Figure 4.9 (b) shows the normalized temperature-dependent PL emission spectra of the ZnO nanophosphors to study the effect of reaction temperature on peak positions. Three emission peaks can be seen at the same position ~ 475 nm for samples prepared at 55, 65 and 75 ℃ while emission for sample prepared at 80 ℃ is positioned at ~ 526 nm. The emergence of green emission at ~ 526 nm is due to formation of pure ZnO. Al-Azri *et al.* [44] obtained the green emission which decreased with the increase in the synthesis temperature. Heo *et al.* [45] reported that green emission is usually observed in ZnO samples prepared in the environment with insufficient oxygen which gives rise to oxygen vacancies (V_O) and such emission was attributed to donor V_O – acceptor V_{Zn} recombination. In the present study, the prepared ZnO using CBD method was without any reducing atmosphere. The environment was not oxygen deficient so the presence of oxygen vacancies is very unlikely. Thus the observed green emission at ~ 526 nm is attributed to radiative transition from conduction band to the edge of the acceptor levels of oxygen antisites O_{Zn} caused by O_{Zn} as reported by Murphy *et al.* [46].

As seen in **Figure 4.9 (b),** the peak positions are red-shifted from blue emission ~ 475 nm to green emission ~ 526 nm with the increase in the reaction temperature. The red-shift of the emission bands can be associated to the increase in the particle size of ZnO with the increase in the reaction temperature as seen in the UV-Vis results. Furthermore, when increasing the reaction temperature all emission spectra are broadened. The possible reason for broadening of PL emission spectra may be related to the increase in concentration of defect related emissions with the increase in reaction temperature. There are many theoretical studies about the broadening of the visible emissions in ZnO, and some studies assigned it to Purcell effect [47 – 48]. The Purcell effect states that, the PL enhancement and broadening in the green

spectral region is due to spontaneous emission rates of atoms when they are matched in a resonant cavity [49].

Figure 4.10 illustrates the Commission Internationale de l'Eclairage (CIE) chromaticity diagram of ZnO nanopowders prepared at different reaction temperatures calculated using photoluminescence data and color calculator software. It can be seen from the figure that the PL CIE coordinates (x, y) of (0.215, 0.273), (0.215, 0.257), (0.254, 0.295) and (0.296, 0.332) correspond to 55, 65, 75 and 80 ℃, respectively with the shade of the blue region. The coordinates are shifted toward the near white light with the increase in reaction temperature. This is because the emission peaks in **Figure 4.9 (b)** are red-shifted. Thus, this indicates that reaction temperature play a major role in tuning the emission of ZnO.

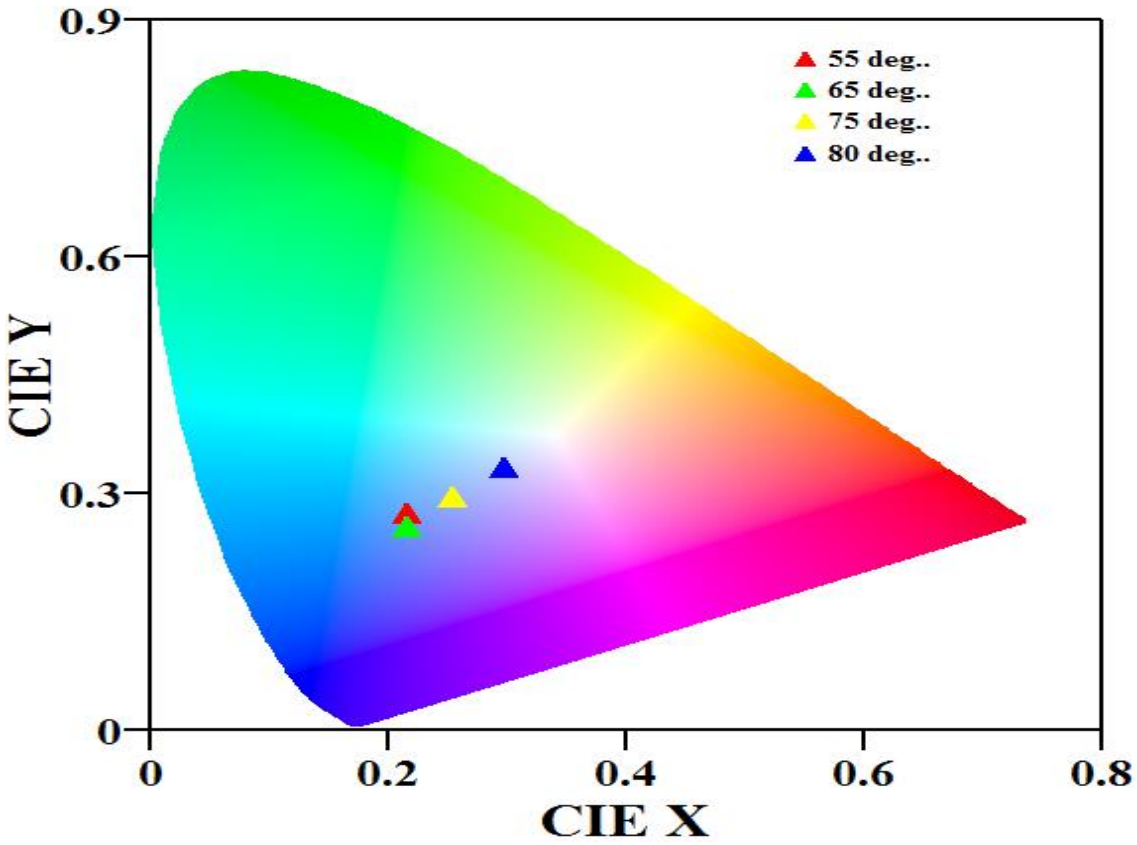

Figure 4.10 CIE diagram of ZnO nanophosphors prepared at various reaction temperatures.

4.3 Conclusion

The ZnO nano-powders were prepared successfully by CBD method at low bath temperature ranges from 55 to 80 °C for 10 minutes per sample. The following changes were observed: structure, surface morphology and optical properties of ZnO. By increasing the reaction temperature $Zn(OH)_2$ decomposed into ZnO and the thermal stability was improved. The melting temperatures were observed to decrease with the increase in reaction temperature due to crystallization of ZnO. From the XRD pattern there is an improvement in structure as reaction temperature increases, and $Zn(OH)_2$ decomposed into ZnO. Morphological changes were observed with the increase in the reaction temperature. Spherical shapes accumulate with flakes like shapes to form the complete nanoflakes morphology. The EDS analysis confirmed that the prepared material consisted of pure ZnO. Absorption band of ZnO can be controlled by changing the reaction temperature. When reaction temperature increases absorption edge shifts to high wavelength and as a result the band gap energy decreases. Due to the increase in the reaction temperature ZnO emission was quenched and we observed red shift in the peak positions. Based on our studies, conclusion can be reached that reaction temperature has a great influence on properties of ZnO. It is found that by varying the reaction temperature we can tune the structure and band gap of ZnO nanophosphors.

4.4 References

[1] A-Q. Zhang, L. Zhang, L. Sui, D-J. Qian and M. Chen *Cryst. Res. Technol.* **48** (2013) 947 – 955

[2] L.F. Koao, F.B. Dejene, R.E. Kroon and H.C. Swart *J. Lumin.* **147** (2014) 85 – 89

[3] A.O. Awodugba and A.O Ilyas *Asian j. appl. sci*. **2** (2013) 41 – 44

[4] L.F. Koao, F.B. Dejene and H.C. Swart *Mat. Sci. Semicon. Proc.* **27** (2014) 33 – 40

[5] M.A. El-Sayed, *Acc. Chem. Res.* **37** (2004) 326

[6] I.S. Jeong, J.H. Kim and S. Im *Appl. Phys. Lett*. **83** (2003) 2946

[7] Vinod Kumar, S. Som, Vijay Kumar, Vinay Kumar, O.M. Ntwaeaborwa, E. Coetsee and H.C. Swart *Chem. Eng. J.* **255** (2014) 541 – 552

[8] L. Sepet, N. Baydogan, H. Cimenoglu, E.S. Kayali, B. Tugrul, N. Altinsoy, G. Albayrak, H. Sengel, F. Akmaz and A. Parlar *Defect and Diffusion Forum*. (2011) 836 – 841

[9] D. Raoufi and T. Raoufi, *Appl. Surf. Sci* **255** (2009) 5812

[10] T.D. Malevu and R.O, Ocaya *Int. J. Electrochem. Sci.* **9** (2014) 8011 – 8023

[11] M.A. Shah, *Afr. Phys.* Rev. **2** (2008) 106 – 109

[12] D.E. Motaung, I. Kortidis, D. Papadaki, S.S. Nkosi, G.H. Mhlongo, J. Wesley-Smith, G.F. Malgas, B.W. Mwakikunga, E. Coetsee, H.C. Swart, G. Kiriakidis and S.S. Ray, *Appl. Surf. Sci.* **311** (2014) 14 – 26

[13] X. Jia, H. Fan, F. Zhang and L. Qin *Ultrasonics Sonochemistry* **17** (2010) 284 – 287

[14] V. Kumar, H.C. Swart, O.M. Ntwaeaborwa, R.E. Kroon, J.J. Terblans, S.K.K. Shaat, A. Yousif and M.M. Duvenhage *Mat. Lett.* **101** (2013) 57 – 60

[15] K. Omri, I. Najeh, R. Dhahri, J.El. Ghoul and L.El. Mir, *Microelectron. Eng.* **128** (2014) 53 – 58

[16] P. Pookmanee, W. Kidrob, R. Intarapoom and S. Phanichphant, *J. Micros. Soc. Tail.* **20 (**2006) 72 – 78

[17] R. Nazir, N. Iqbal, A.S. Khan, A. Akram, A. Asif, A.A. Chaudhry, I. Rehman and R. Hussain, *Ceram. Int.* **38** (2012) 457

[18] A. Kathalingam, N. Ambika, M.R. Kim, J. Elanchezhiyan, Y.S. Chae and J.K. Rhee *Materials Science-Poland*. **28** (2010) 513 – 522

[19] B.R. Sankapal, S.D. Sartale, C.D. Lokhande and A. Ennaoui *Sol. Energy Mater. Solar Cells*. **83** (2004) 447

[20] A.I. Inamdar, S.H. Mujawar, S.R. Barman, P.N. Bhosale and P.S. Pat, *Semicond. Sci. Technol.* **23** (2008) 085013

[21] E. Belavalli, P. Prasad, K. Vishnu and S. Ranganath *J. Solid State Electrochem.* **16** (2012) 3715 – 3722

[22] S. Kumar and P.D. Sahare, *Optics Communications* **285** (2012) 5210 – 5216

[23] G.R. Patil, R.S. Gaikwad, M.B. Shelar, R.S. Mane, S.H. Han, B.N. Pawar *Arch. Phy. Res.* **3** (2012) 401 – 406

[24] Y. Khan, S.K. Durrani, M. Mehmood, J Ahmad, M.R. Khan and S. Firdous, *App. Surf. Sci.* **257** (2010) 1756 – 1761

[25] W. Jia, S. Dang, H. Liu, Z. Zhang, C. Yu, X. Liu and B. Xu, *Mater. Lett.* **82** (2012) 99 – 101

[26] Y. Khan, S.K. Durrani, M. Mehmood, J. Ahmad, M.R. Khan and S. Firdous, *Applied Surface Science*. **257** (2010) 1756 – 1761

[27] Y.T. Prabhu, K.V. Rao, V.S.S. Kumar, B.S. Kumari , *Advances in Nanoparticles*. **2** (2013) 45 – 50

[28] G. Takidis, D.N. Bikiaris, G.Z. Papageorgiou, D.S. Achilias and I. Sideridou, *Journal of Applied Polymer Science*. **90** (2003) 841 – 852

[29] A. Goux, T. Pauporté, J. Chivot and D. Lincot, *Electrochimica Acta.* **50** (2005) 2239 – 2248

[30] N.J. Ridha, M.H.H. Jumali, A.A. Umar and F. Alosfur, *Int. J. Electrochem. Sci*. **8** (2013) 4583 – 4594

[31] P.V. Adhyapak, S.P. Meshram, V. Tomar, D.P. Amalnerkar and I.S. Mulla *Ceramics International.* **39** (2013) 7367 – 7378

[32] S. Sreekantan, L.R. Gee and Z. Lockman, *Journal of Alloys and Compounds* **476** (2009) 513 – 51

[33] H-S. Goh, R. Adnan and M.A. Farrukh, *Turk. J. Chem.* **35** (2011) 375 – 391

[34] S. Sepulveda-Guzman, B. Reeja-Jayan, E. de la Rosa, A. Torres-Castro, V. GonzalezGonzalez, M. Jose-Yacaman, *Mater. Chem. Phys*. **115** (2009) 172

[35] A.K. Zak, R. Razali, WH.A. Majid and M. Darroudi, *International Journal of Nanomedicine* **6** (2011) 1399 – 140

[36] B. Jaber and L. Laânab, *Materials Science in Semiconductor Processing* **27** (2014) 446 – 451

[37] I.A. Ezenwa *Research Journal of Chemical Sciences* **2** (2012) 26 – 30

[38] L.F. Koao, B.F. Dejene and H.C. Swart, *Physica B.* (2013) 1 – 4

[39] J. Xu, Z. Ju, X. Gao, Y. An, X. Tang and W. Liu, *Inorg. Chem.* (2013) 1 – 7

[40] S. Talam, S.R. Karumuri, and N. Gunnam, *ISRN Nanotechnology*. **2012** (2012) 1 – 6

[41] S. Tachikawa, A. Noguchi, T. Tsuge, M. Hara, O. Odawara and H. Wada, *Materials*. **4** (2011) 1132 – 1143

[42] S.M. Soosen, L. Bose and K.C. George, *SB Academic Review*. **1 & 2** (2009) 57 – 65

[43] C. Florica, N. Preda, M. Enculescu, I. Zgura, M. Socol and I. Enclulecsc, *Nanoscle Research Letters* **9** (2014) 385 1 – 10

[44] K. Al-Azri, R.M. Nor, Y.M. Amin and M.S. Al-Ruqeishi, *App. Surf. Sci.* **256** (2010) 5957 – 5960

[45] Y.W. Heo, D.P. Norton and S.J. Pearton, *J. Appl. Phys.* **98** (2005) 073502

[46] T.E. Murphy, K. Moazzami and J.D. Phillips *J. Electron. Mater.* **35** (2006) 543 – 549

[47] M. Boroditsky, R. Vrijen, T. F. Krauss, R. Coccioli, R. Bhat and E. Yablonovitch *J. Lightwave Tech.* **17 (**1999) 2096

[48] T.D. Happ, I.I. Tartakovskii, V.D. Kulakovskii, J.-P. Reithmaier, M. Kamp and A. Forchel, *Phys. Rev. B,* **66** (2002) 041303(R)

[49] E.M. Purcell, *Phys. Rev.* **69** (1946) 681

5

Effect of reaction time on structural, morphology and optical properties of ZnO nanoflakes prepared by chemical bath deposition method

5.1 Introduction

Owing to their unique optical and luminescence properties, one-dimensional (1D) ZnO nanostructures have received great attention in the past decade. Photoluminescence (PL) properties of ZnO nanostructures have been extensively investigated due to potential application of these materials in light emitting devices [1]. These materials behave differently from bulk semiconductors. With decreasing the particle size the band structure of the ZnO semiconductor changes, the band gap increases and the edges of the bands split into discrete energy levels. This process is called quantum confinement. But researchers have also found band gap increases in some nanomaterial's having sizes far beyond the quantum confinement regime [2]. Zinc oxide (ZnO) is an inorganic compound and occurs rarely in nature, generally appears as a white crystalline powder, which is nearly insoluble in water. It has been under intensive focus among the researchers because of its special properties such as high electron mobility with undoped state, high thermal conductivity, good transparency, wide band gap (~ 3.37 eV), large exciton binding energy (60 meV) and room temperature thermal excited energy (25 meV) [3]. The following methods have been developed to prepare nanostructured ZnO and include sol–gel [4], chemical bath deposition method [5], electro deposition [6], microwave-assisted techniques [7], chemical vapor deposition [8], hydrothermal [9] and precipitation methods [10]. In this study the ZnO nanoflakes were synthesized by the chemical bath deposition method (CBD). CBD is one of the solution phase methods useful for the preparation of compound semiconductors from aqueous solutions [11]. The CBD method has several advantages such as the use of simple equipment, cost effective, less hazardous and the low temperature reaction. The low reaction temperature makes this method attractive and the particle properties such as morphology and size can be controlled via the CBD process by adjusting the synthesizing time [12]. In this paper, ZnO samples were successfully synthesized by the chemical bath deposition by varying the reaction times. The

transformation of the amended cubic phase ZnO to hexagonal (wurtzite) phase was observed for the first time.

5.2 Results and discussions

5.2.1 Structural and compositional analyses

Figure 5.1 shows the X-ray diffraction (XRD) patterns from ZnO particles produced in 1, 3, 5 and 10 min. At a short reaction time ($1 \leq t \leq 3$) the modified cubic ZnO phase [13–15] has three peaks at 33.51, 59.51, and 69.61, which are consistent with the literature data of JCPDS 21-1486. By increasing the synthesizing time the detected (h k l) peaks are at 2θ values of 31.81, 34.51, 36.41, 47.51, 56.21, 62.91 and 69.11 corresponding to the lattice planes (1 0 0), (0 0 2), (1 0 1), (1 0 2), (1 1 0), (1 0 3) and (2 0 1) respectively, which are in agreement with the standard JCPDS (card no. 361451) for hexagonal wurtzite ZnO except that the peaks marked with a star that still represents the modified cubic ZnO structure.

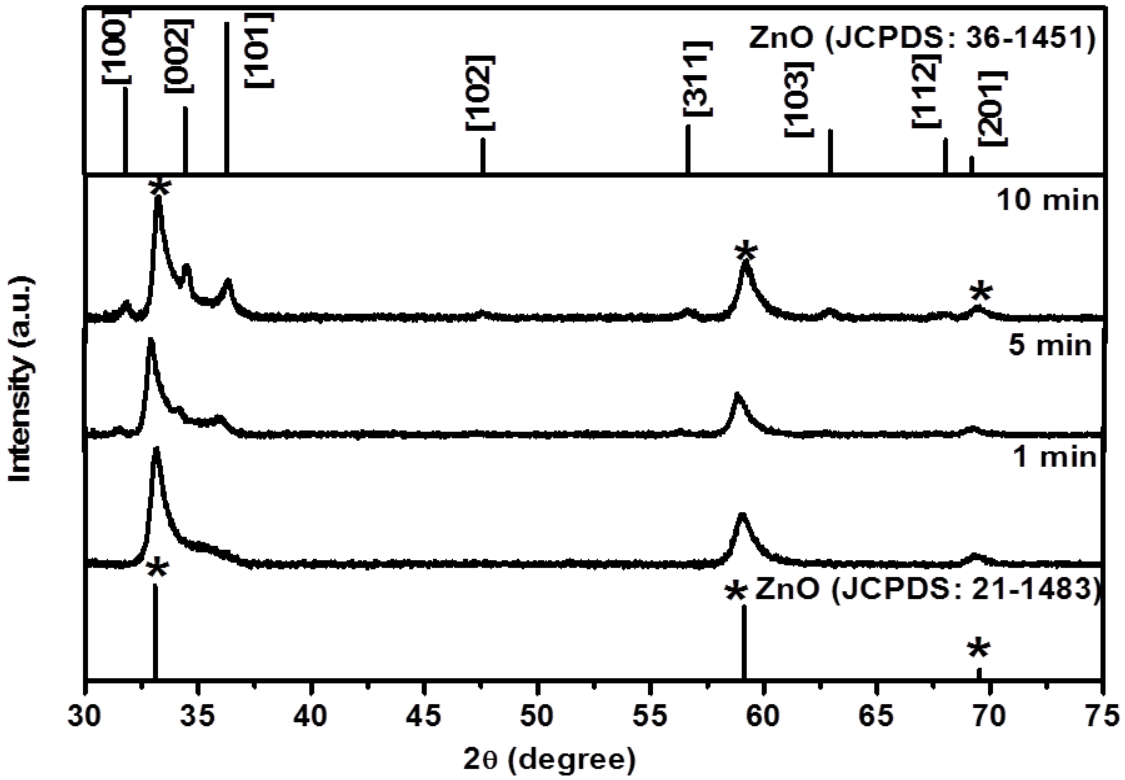

Figure 5.1 XRD patterns of ZnO nanostructures synthesized at different reaction times using the CBD method.

In order to evaluate the mean crystallite size of the particles, the Scherrer formula depicted in equation 5.1 was used [16] to determine the crystallite sizes of the different ZnO particles. From Scherrer formula D represents thickness of crystallite, K is constant dependent on crystallite shape (0.89) λ is X – ray wavelength (0.154 nm) β is FWHM (Full width at half maximum) in radians and θ-scattering angle in degrees.

$$D = \frac{K\lambda}{\beta Cos(\theta)} \tag{5.1}$$

Two major diffraction peaks for all samples were chosen to estimate the average size of the nanoparticles by the least square method. The estimated grain sizes are 24, 26 and 29 nm for 1 min, 5 min and 10 min. It is clear that the estimated grain sizes increases with an increase in synthesis time. Thus the growth time during synthesis of ZnO by the CBD method plays an important role on the ZnO nanostructure.

Figure 5.2 (a) and (b) shows the surface morphologies of the ZnO powders prepared at various synthesis time ranging from 1 min to 10 min. The surface aspects of the SEM images of both of the ZnO samples consist of agglomerated nanoflakes structures which appear non-uniform for both. It is discovered that the increase in reaction time did not have a significant effect on surface morphology.

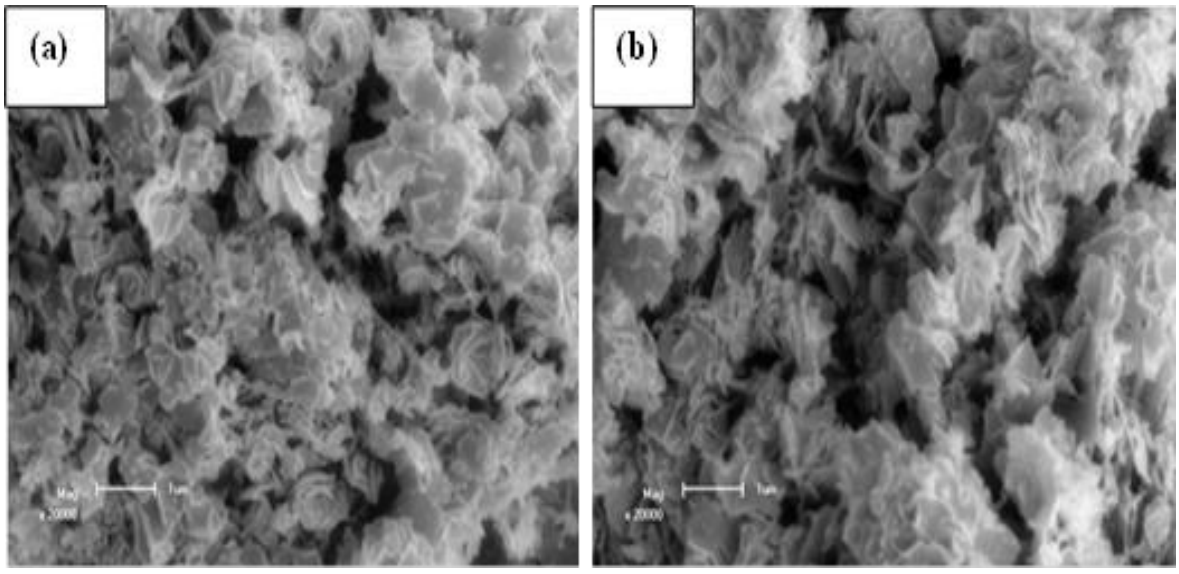

Figure 5.2 SEM images of ZnO nanostructures synthesized at different reaction time **(a)** 1 min and **(b)** 10 min using the CBD method.

5.2.2 Optical properties

The UV–visible reflectance spectra of ZnO nanostructures synthesized at various reaction times is shown in **Figure 5.3**. The spectra of all the samples show good optical quality in the visible range due to the complete reflectance in the 200–800 nm range. With increasing the synthesis time, the reflectance in the UV region obviously decrease and the absorption edge shifts slightly (circled part in **Figure 5.3**) to a longer wavelength region. The red shift of the absorption peak should be due to quantum-size effects. The ZnO is a direct band gap material. The energy band gap of these materials was estimated using the Kubelka–Munk remission function in equation (5.2) [17],

$$K = \frac{(1-R)^2}{2R} \qquad (5.2)$$

where K is reflectance transformed according to Kubelka–Munk, R is reflectance (%), hv is the photon energy, E_g is the band gap at n = 2 for direct transitions.

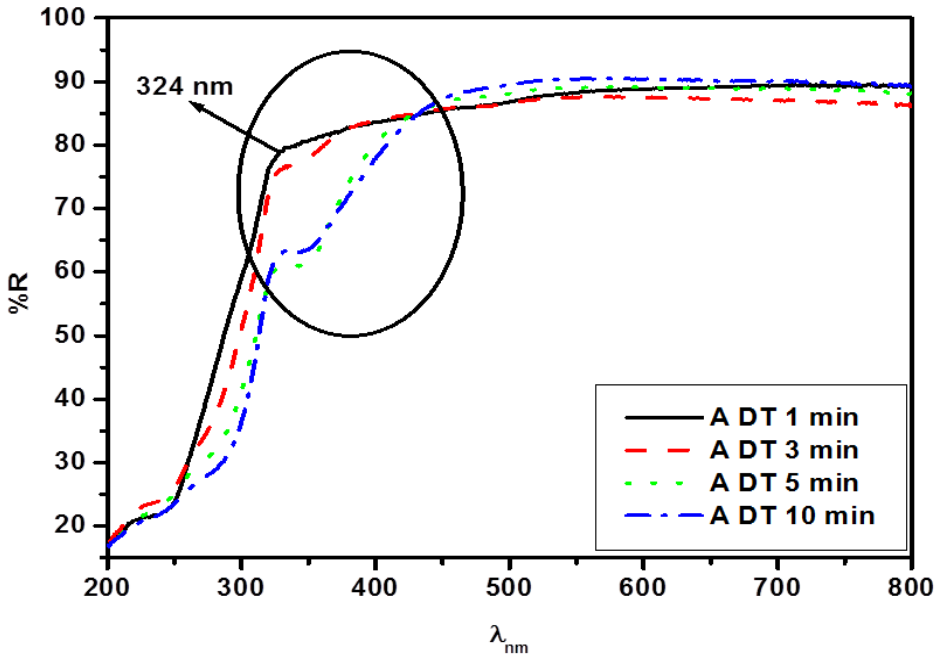

Figure 5.3 The reflectance spectra of the ZnO nanoflakes synthesized at different reaction times using CBD method.

In **Figure 5.4** the energy band gaps were measured with the help of reflectance spectra plotting graphs of $(Khv)^n$ versus $f(hv)$ [18]. However, it is notable that the absorption spectra are composed of two absorption edges for samples synthesized for 5 and 10 min

(**Figure 5.4**). The absorptions at the low energy side are ascribed to the absorption of bulk ZnO nanostructures from which band gaps are estimated to be 3.34 ± 0.06 and 3.26 ± 0.07 eV for samples prepared at 5 and 10 min, respectively.

The dependence of the band gap energy of the ZnO on synthesis time is illustrated in **Figure 5.5**. It can be seen clearly that the band gap energy of the ZnO nanoflakes decay nearly exponential with synthesis time. The highest band gap energy is obtained for sample synthesized at 1 min, with its estimated band gap energy of 4.01± 0.08 eV. The shift of absorption edge and the change in band-gap energy may be attributed to the slight changes in particle sizes.

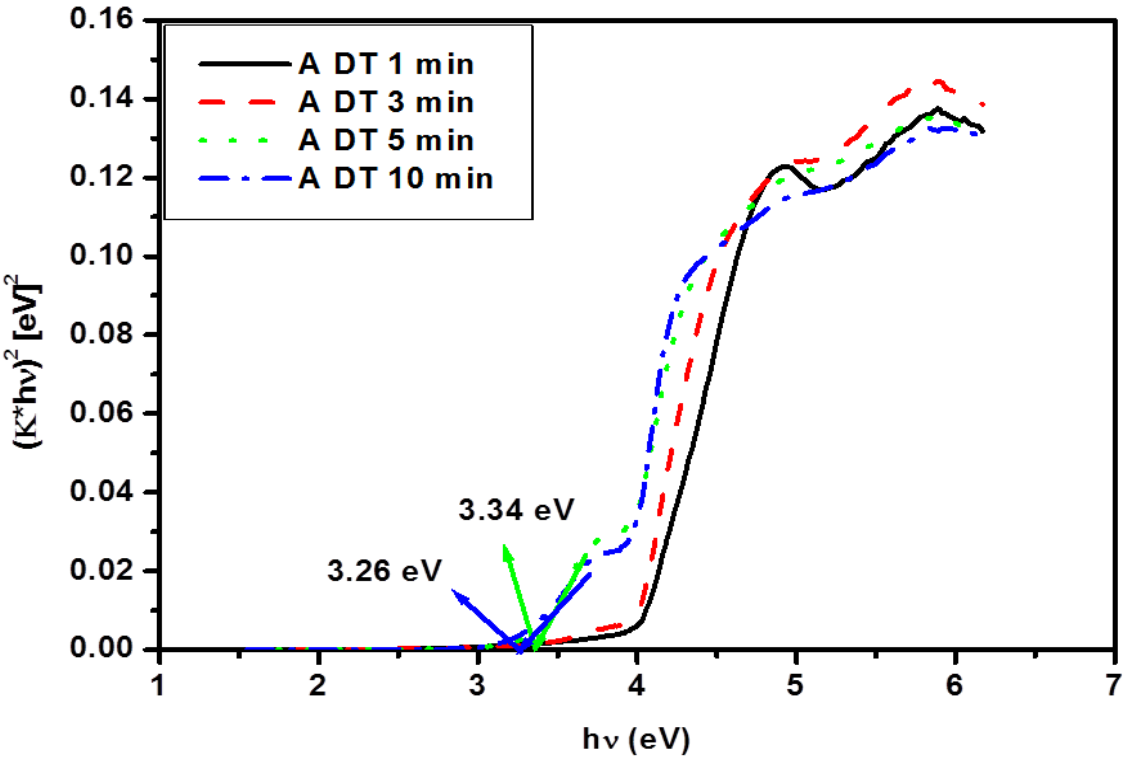

Figure 5.4 Plot to determine the band gap energy of ZnO nanoflakes prepared by CBD method.

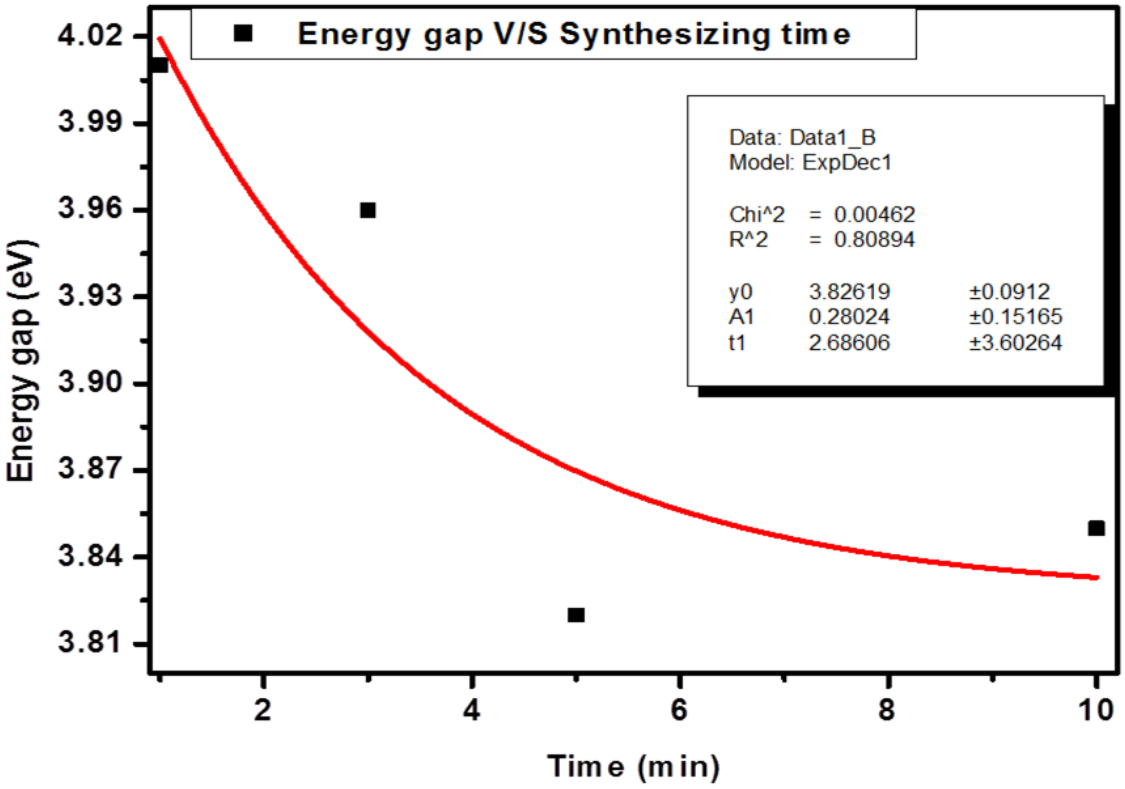

Figure 5.5 Dependence of band gap energies of the ZnO nanoflakes on the reaction time.

5.2.3 Photoluminescence properties

The PL measurement of the ZnO nanostructures was carried out using a Xenon lamp. The excitation spectra obtained by monitoring the emission of ZnO at around 473 nm is depicted in **Figure 5.6**. It can be seen that the excitation spectrum consists of a broad band with a maximum peak at 316 nm whose intensity decreases with the increase in reaction time. The excitation peak corresponds to the band to band transition in the band gap of ZnO nanoparticles [19].

Figure 5.7 shows the photoluminescence emission spectrum of the ZnO nanoflakes synthesized at various reaction times, excited by the 316 nm wavelength. One obvious broad peak is observed; the blue emission band is from 375 nm to 675 nm and the center value is 473 nm, which ascribed to electron transitions from Zn_i to V_{Zn} [20]. Lin *et al*. [21] calculated the energy levels of intrinsic defects in undoped ZnO and figured out the energy level draft of the intrinsic defects. The maximum emission intensity was obtained for the ZnO nanoflakes synthesized for 1 min. The location of blue emission does not change while the intensity has become weaker with increase in synthesis time. A possible reason for the blue emission

diminishing may be related to increase in particle size with increasing synthesis time which causes an increase in surface defect density.

Figure 5.8 shows the plot of intensity versus the reaction time for ZnO prepared by the CBD method. It can be seen clearly that the luminescence intensity in the visible region decay nearly exponential with synthesizing time. The higher reaction time resulted in a substantial decrease in luminescence intensity.

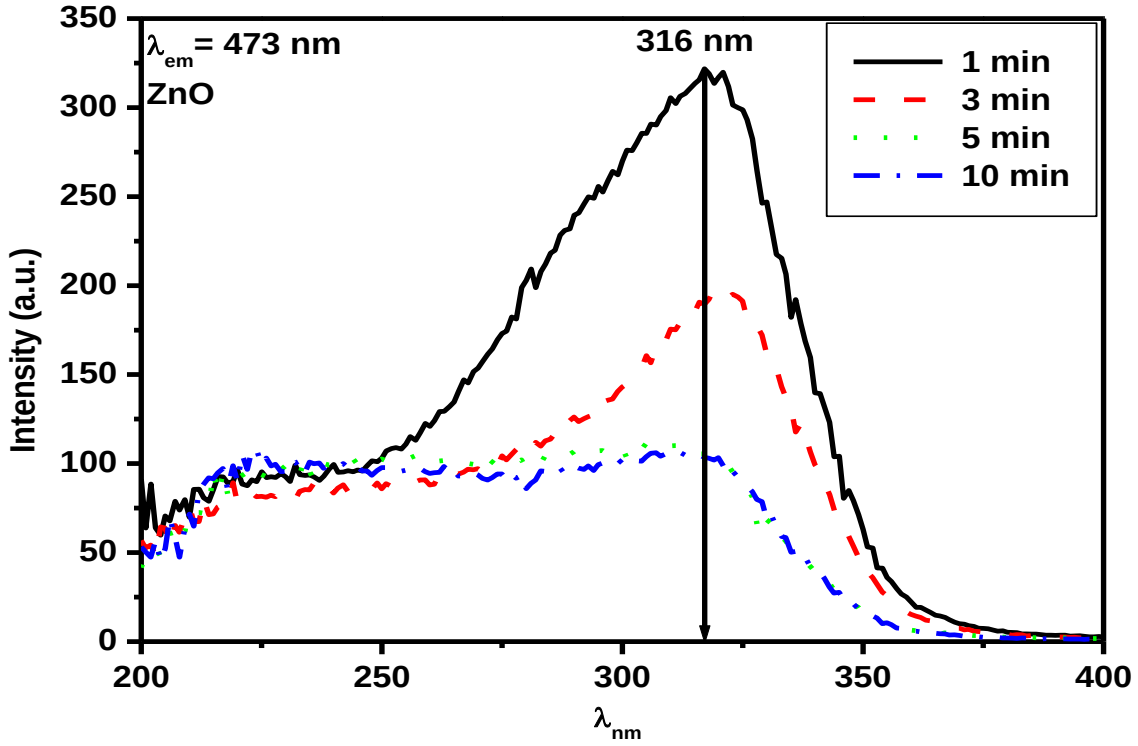

Figure 5.6 PL excitation spectra of ZnO nanoflakes emitted at λ_{em} = 473 nm.

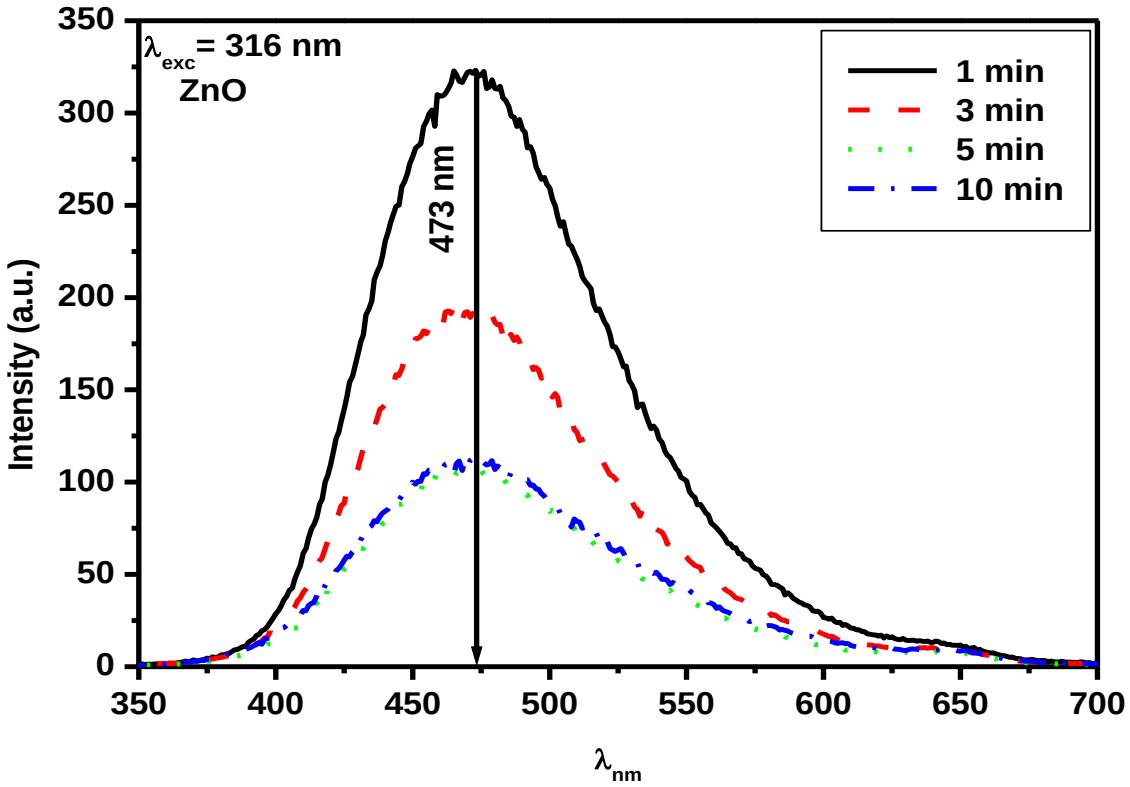

Figure 5.7 PL emission spectra of ZnO nanoflakes excited at λ_{exc} = 316 nm.

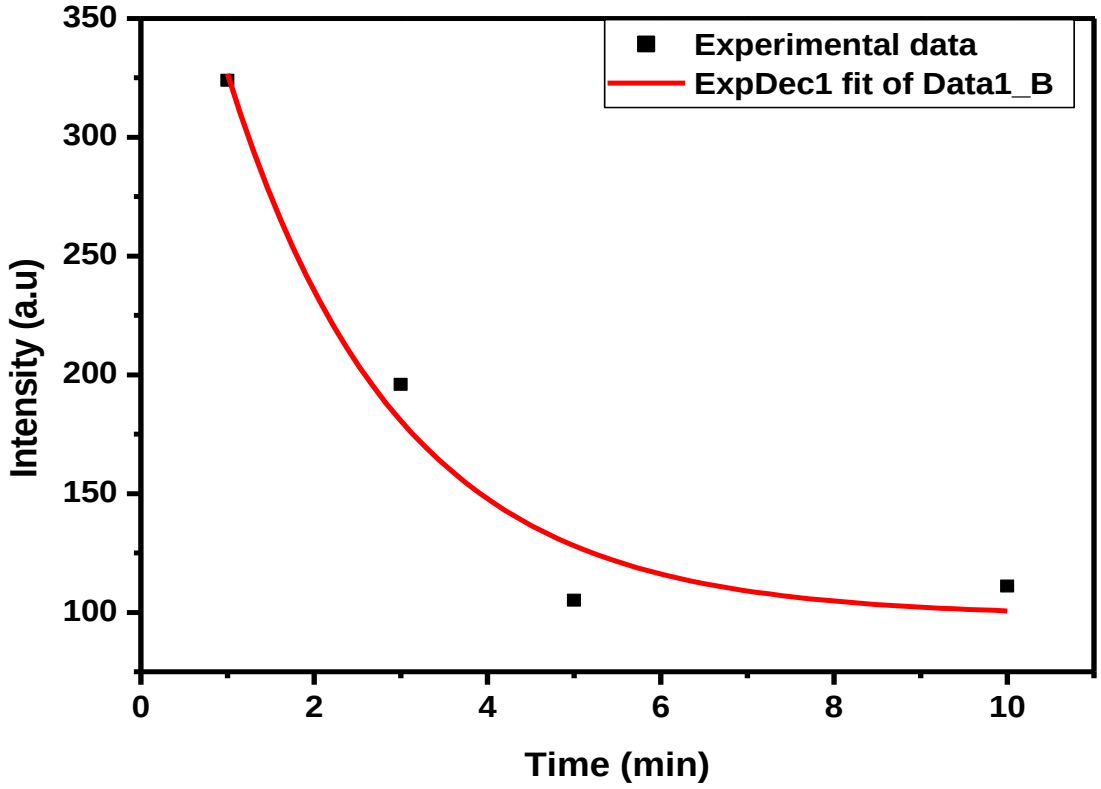

Figure 5.8 The effect of time on luminescence intensity of ZnO nanoflakes synthesized at different reaction times.

5.3 Conclusion

The CBD method was successfully used to prepare ZnO nanostructure at different reaction times. Increasing reaction time showed a noticeable effect on structural, morphological, optical and luminescence properties of ZnO. XRD showed that as the synthesizing time increased the modified cubic phase of ZnO changed to hexagonal wurtzite ZnO. SEM images depict homogenous agglomerated ZnO nanoflakes. UV spectroscopy showed that the highest band gap energy is obtained at ZnO synthesized for 1 min, with its estimated band gap energy of 4.01 ± 0.08 eV. The band gap energy of the ZnO nanoflakes decreased with an increase in the reaction time. The PL intensity was found to be a maximum for ZnO nanoflakes synthesized for 1 min and thereafter luminescence intensity decreased with an increase in reaction time.

5.4 References

[1] H.J. Zhou, M. Wissinger, J.F. Allert, R. Hauschild, F.S telzl, C. Klingshirn, H. Kalt, *Appl. Phys. Lett.* **91** (2007) 181112 - 1 – 181112-3

[2] C.W. Chen, K.H. Chen, C.H. Shen, A. Ganguly, L.C. Chen, J.J. Wu, H.I. Wen, W.F. Pong, *Appl. Phys. Lett*. **88** (2006) **241** 905-1 – 241905-3

[3] J.P. Borah, J. Barman, K.C. Sarma, Chalcogenide Lett. **5** (2008) 201 – 208

[4] M.S. Takumoto, S.H. Pulcinelli, C.V. Santilli, V. Briois, *J. Phys. Chem.* **107** (2003) 568 – 574

[5] L.F. Koao, F.B. Dejene, R.E. Kroon, H.C. Swart, *J. Lumin*. **147** (2014) 85

[6] A.B. Moghamad, T. Nazari, J. Badraghi, M. Kazemzadeh, *Int. J. Electrochem.* **4** (2009) 247 – 257

[7] X.L. Hu, Y.J. Zhu, S.W. Wang, *Mater. Chem. Phys.* **88** (2004) 421–426

[8] J.J. Wu, S.C. Liu, *Adv. Mater*. **14** (2002) 215 – 218

[9] H.J. Zhai, W.H. Wu, F. Lu, H.S. Wang, *Mater. Chem. Phys*. **112** (2008) 1024 – 1028

[10] M. Bitenc, M. Marinsek, Z. C. Orel, *J. Eur. Ceramic. Soc*. **28** (2008) 2915–2921

[11] P. Duran, F. Capel, J. Tartaj, C. Moure, *Adv. Mater*. **14** (2002) 137 – 141

[12] J.K. Behera, MSc thesis, *National Institute of technology, India*. pp. 11 – 35

[13] T.H. Aeugle, H. Bialas, K. Heneka, W. Pleyer, *Thin Solid Films*. **201** (1991) 293–304

[14] M. Parhizkar, N. Kumar, P.K. Nayak, S. Singh, S.S. Talwar , S.S. Major, R.S. Srinivasa, *J. Colloids and Surfaces A: Physicochem. Eng. Aspects* **257–258** (2005) 445 – 449

[15] Y. Liao, X. Wu, Z. Wang, Y.F. Chen, *J. Solid. Sate. Chem*. **184** (2011)1603 – 1607

[16] G. RangaRao, H. RanjanSahu, *Proc. Indian Acad. Sci. (Chem. Sci).* **113** (2001) 651 – 658

[17] J. Tauc, R. Grigorovici, A. Vancu Sharma, *Phys. Status Solidi.* **15** (1966) 627 – 629

[18] M. Xiangyang, Z. Hui, J. Yujie, X. Jin, Y. Deren, *Mater. Lett*. **59** (27) (2005) 3393 – 3397

[19] W.Q. Peng, S.C. Qu, G.W. Cong, Z.G. Wang, *Mater. Sci. Semicond. Process*. **9** (2006) 156 – 159

[20] M. Willander, O.Nur, J.R. Sadaf, M.I. Qadir, S. Zaman, A. Zainelabdin, N.Bano, I. Hussain, *Mater.* **3** (2010) 2643

[21] B.X. Lin, Z.X. Fu, Y.B. Jia, *Appl. Phys. Lett.* **79** (2001)7

6

Influence of zinc acetate concentration in the preparation of ZnO nanoparticles via chemical bath deposition

6.1 Introduction

Zinc oxide (ZnO) is a metal oxide semiconductor material with wide direct band gap energy equal to 3.37 eV [1]. It is an n – type semiconductor which has a moderate high exciton binding energy of 60 meV at room temperature [2]. This large exciton binding energy indicates that efficient excitonic emission in ZnO can persist at room temperature and higher [3]. From the first half of the 20th century ZnO has been under great focus even up-to-date it is still drawing attention due to its unique structure and morphology [4]. This wurtzite n – type semiconductor has potential applications because of various properties that include good transparency, high electron mobility, and strong room temperature luminescence [5].

Simply because ZnO has good optical properties it can be used in solar cells and light emitting devices [6]. Recently nanotechnology is playing a major role in optimizing metal oxide for various applications in the fields such as electronics, material science and optics [7]. Lifen *et al.* [8] showed that ZnO has different morphologies ranging from the hexagonal shape up to the rhombohedron shape which can be obtained by different methods of preparation. Several techniques have been employed recently to prepare ZnO and include solution combustion method [9].

Three dimensional flower-like morphologies have been synthesized through facile hydrothermal process by Lu *et al.* [10] at 95 ℃ for 24 hrs who obtained well dispersed flower-like ZnO structures. Koao *et al.* [11], reported on the Properties of flower-like ZnO nanostructures synthesized using the chemical bath deposition (CBD) technique. They found that by varying the amount of ZnAc there was no change in morphology and crystal structure, due to high concentration of ZnAc that was used. Following the work of Koao *et al*. [11], we prepared ZnO at low ZnAc concentration to study its influence on structural, morphology, optical and luminescence properties using CBD technique.

The current study confirms the consistency of CBD method for the formation of flower-like morphology. The CBD method is preferred due to sample preparation at low temperature and

it is relatively inexpensive way of preparation hence it provides a good control of particle size and a uniform morphology.

6.2 Results and discussions

6.2.1 Structural analysis

Figure 6.1 (a) presents the XRD patterns of ZnO prepared at various concentrations of ZnAc ranging from 0.1 to 0.2 M. All the XRD diffraction peaks observed between 0.1 to 0.18 M match with hexagonal wurtzite structure JCPDS card no. 36-1451, with calculated average lattice constants a = 3.245 Å and c = 5.177 Å. There was no effect on lattice constants as ZnAc concentration increases. At higher ZnAc concentration 0.2 M there is a mixture of ZnO diffraction peaks marked with circles (^{o}) and ZnAc diffraction peaks marked with asterisks (*). The Scherrer's equation [12], was employed to estimate the ZnO mean crystalline size using the full width at half maximum (FWHM) of all the diffraction peaks. The average estimated mean crystalline size of ZnO powders was ~ 23 nm, and there was no change in the crystalline size when increasing ZnAc concentration. From **Figure 6.1 (b)** it is observed that the preferred (101) orientation of the ZnO powders, have slightly shifted to higher diffraction angles when the ZnAc concentration was increased. This corresponds to the decrease in lattice spacing with more Zn^{2+} ions incorporated into the ZnO.

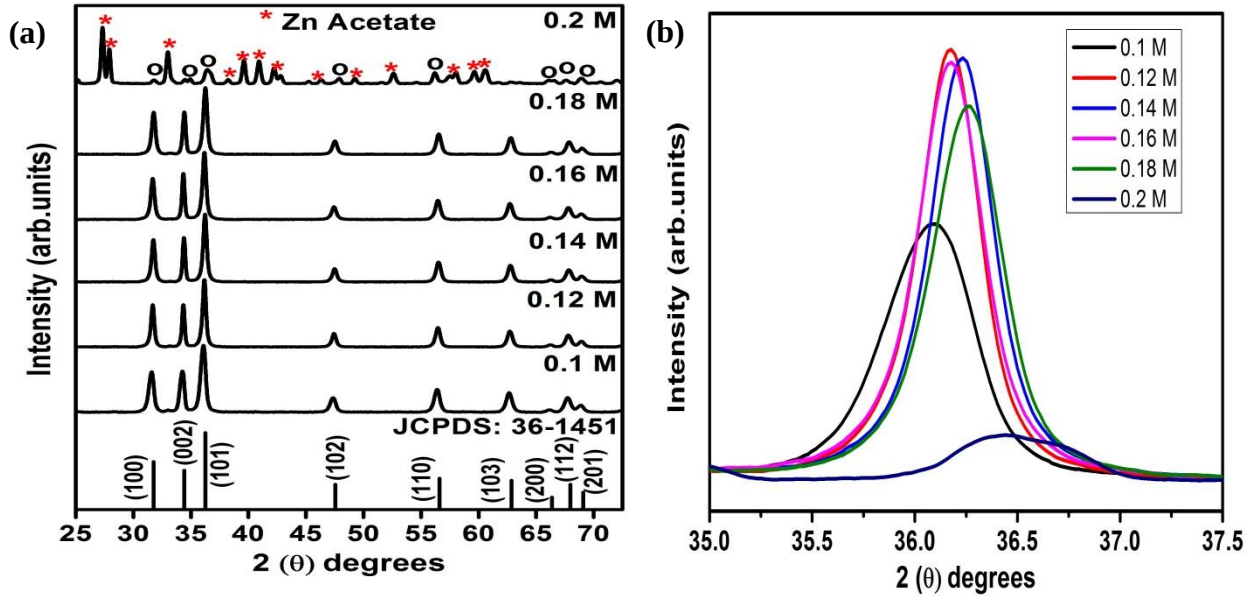

Figure 6.1 XRD patterns of **(a)** ZnO nanoparticles prepared at different concentrations of ZnAc using the CBD method as well as the JCPDS standard spectrum, **(b)** Detail of the (101) peak.

6.2.2 SEM analysis

The SEM images of the ZnO nanoparticles prepared using the CBD method by varying ZnAc concentration are shown in **Figure 6.2 (a) – (d)**. In **Figure 6.2 (a)** the image reveals highly agglomerated flower-like particles for the samples prepared at the low concentration of ZnAc 0.1 M. The image in **Figure 6.2 (b)** shows a slight increase in size of flower – like particles for 0.14 M concentration. **Figure 6.2 (c)** shows a sample prepared at 0.18 M concentration with more pronounced flowers in which big voids occurs. Such voids are also available in between flower-like structures presented in **Figure 6.2 (a) and (b)**, and are caused by the evaporation of water molecules when drying the samples and the addition of ZnAc created more surface defects. With increasing the ZnAc concentration to 0.2 M we observed an alteration in the structure wherein small flower-like structures are grown on big diamond like structure as shown in **Figure 6.2 (d)**. We assume that the observed big chunks are caused by the unreacted ZnAc. When comparing the results presented from **Figure 6.2 (a) – (c)** it can be seen that the morphology is non-uniform flower-like structures, except for the sample prepared at 0.2 M which also showed ZnAc impurities in the XRD spectrum.

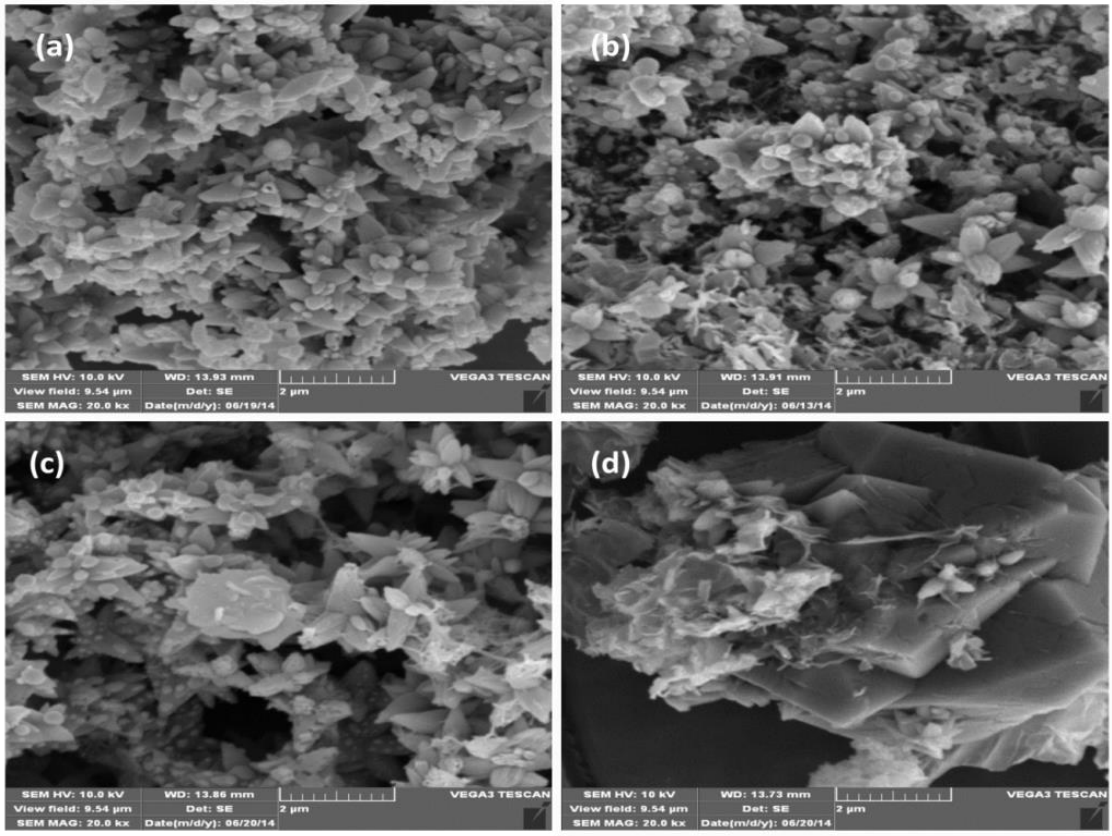

Figure 6.2 SEM images of ZnO nanoparticles prepared at different concentrations of ZnAc using the CBD method, **(a)** 0.1 M **(b)** 0.14 M **(c)** 0.18 M and **(d)** 0.2 M.

6.2.3 UV-vis analysis

Figure 6.3 shows diffuse reflectance measurements of the ZnO nanoparticles in the wavelength range 200 – 800 nm. The percentage reflectance in the visible region increased from ~ 78.5 % at 0.1 M and reached ~ 94.7 % maximum at 0.14 M ZnAc concentration. This indicates that the ZnO absorbs more at low ZnAc concentration. When increasing the ZnAc concentration from 0.1 M to 0.18 M we observed no shift in the absorption band. As illustrated in **Figure 6.3** there is a blue shift in absorption band for the sample prepared at 0.2 M ZnAc concentration. This blue shift may be due to ZnAc impurities observed in the XRD spectrum and the formation of diamond like structure observed in the SEM morphology at 0.2 M ZnAc concentration.

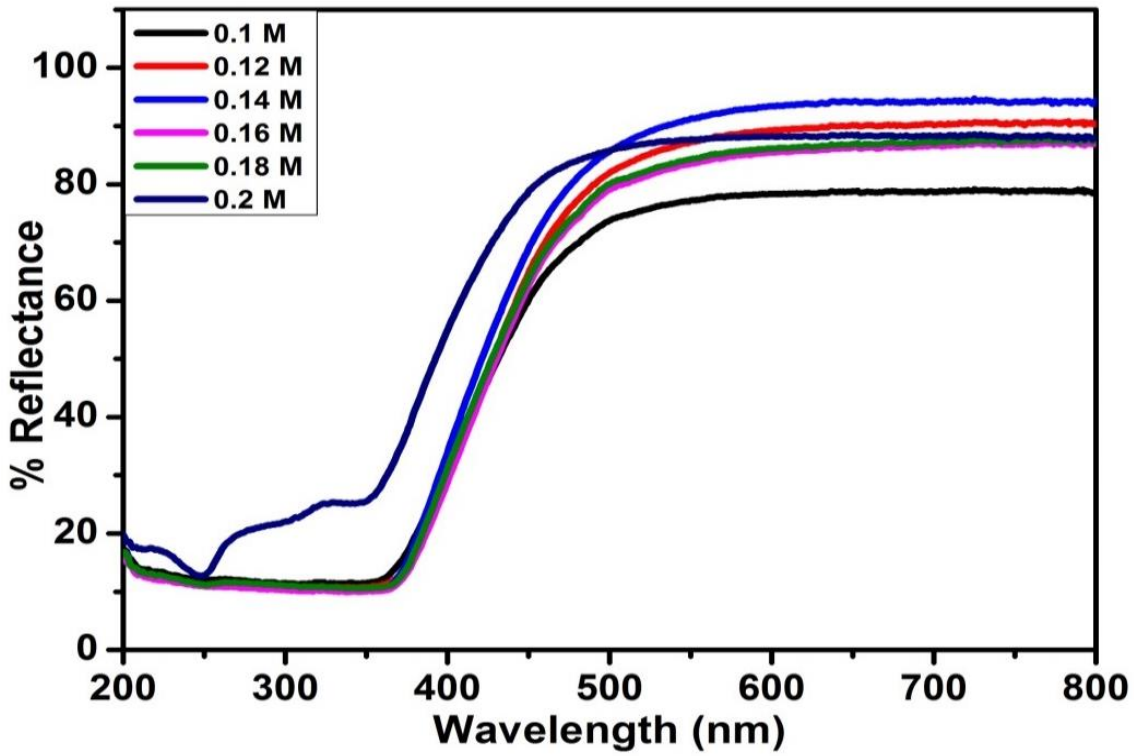

Figure 6.3 shows the comparison between diffuse reflectance curves of the ZnO prepared at different concentrations of ZnAc.

The optical band gaps (E_g) for the ZnO powders was calculated from the Kubelka Munk's function [13], by extrapolating the linear portion of the graph to $(Khv)^2 = 0$ as shown in **Figure 6.4**. It is demonstrated in **Figure 6.4** that the optical band gaps (E_g) shows no appreciable change for ZnO powders prepared at 0.1 to 0.18 M ZnAc concentrations. The

non-change in band gaps can be because of no change in crystalline size when increasing ZnAc concentration. The average estimated energy band gap for ZnO powders prepared at 0.1 to 0.18 M ZnAc concentrations is ~ 3.20 eV. The inset in **Figure 6.4** shows the increase in band gap for the sample prepared at 0.2 M ZnAc, which is equal to ~ 4.60 eV. The increase in band gap energy due to increase in the ZnAc to 0.2 M concentration also relates to ZnAc impurities and structural morphology observed in **Figure 6.1** and **Figure 6.2 (d)**.

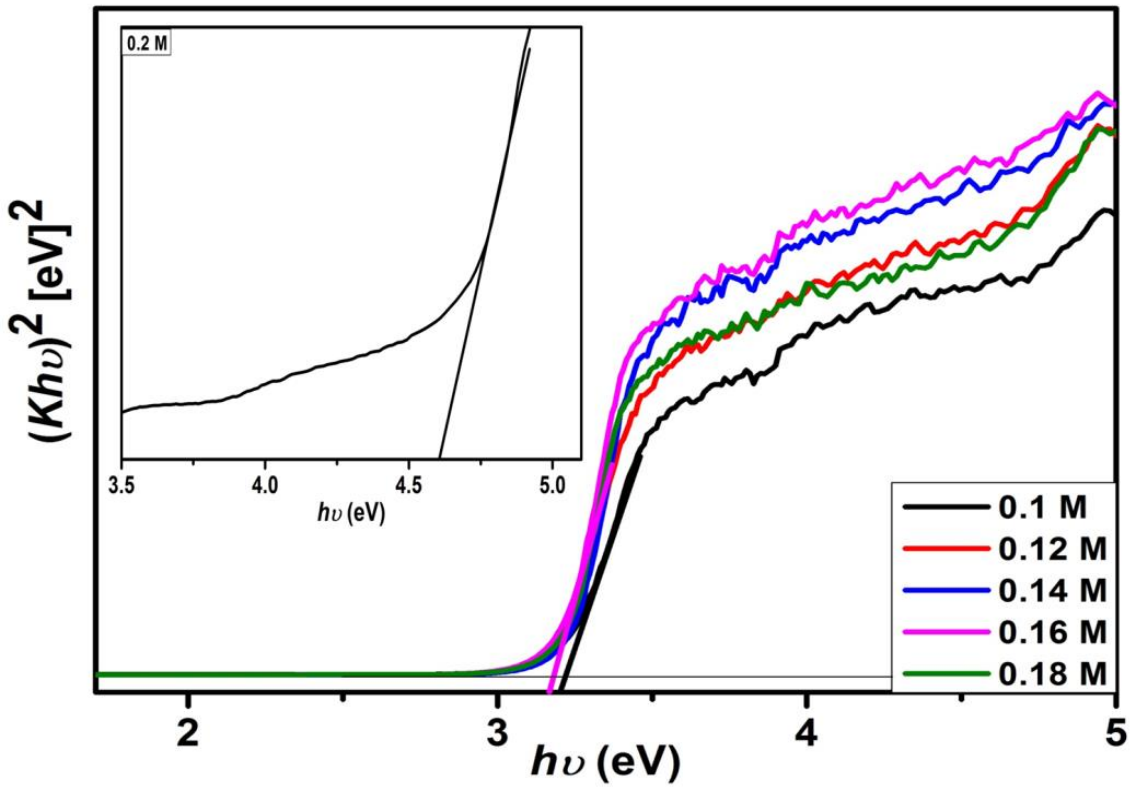

Figure 6.4 Estimate of the direct energy band gap of ZnO for different concentrations of ZnAc.

6.2.4 Photoluminescence analysis

Figure 6.5 shows the room temperature PL spectra of the obtained ZnO flower-like structure prepared at different concentrations of ZnAc. It can be seen that the emission spectrum consist of a broad band in the visible region with two observable peaks. The PL spectrum for the sample prepared at the low ZnAc concentration of 0.1 M exhibits a dominant band emission in the blue region at ~ 450 nm, and a weak green band emission at ~ 528 nm. The luminescence band emission at ~ 450 nm is caused by the electronic transitions from zinc interstitial levels (Zn_i) to the valence band [14].The observed weak green emission at ~ 528

nm has been attributed by several authors to the oxygen vacancies (V_O) [15], therefore the green emission is due to radiative recombination of photo generated hole with an electron occupying the oxygen vacancy at the local level in the band gap [16]. It is clear that with increasing ZnAc concentration from 0.1 M to 0.18 M the blue emission is quenched while the green emission is enhanced, and there is a small red-shift in the green emission. This phenomenon can be clearly seen in the inset in Figure 5 wherein the spectra for 0.2 M ZnAc is not included. Further increasing of the ZnAc concentration to 0.2 M enhanced the luminescence intensity, indicating an increase in the density of defects such as zinc interstitial (Zn_i) and oxygen vacancies (V_O) within the ZnO nanoparticles.

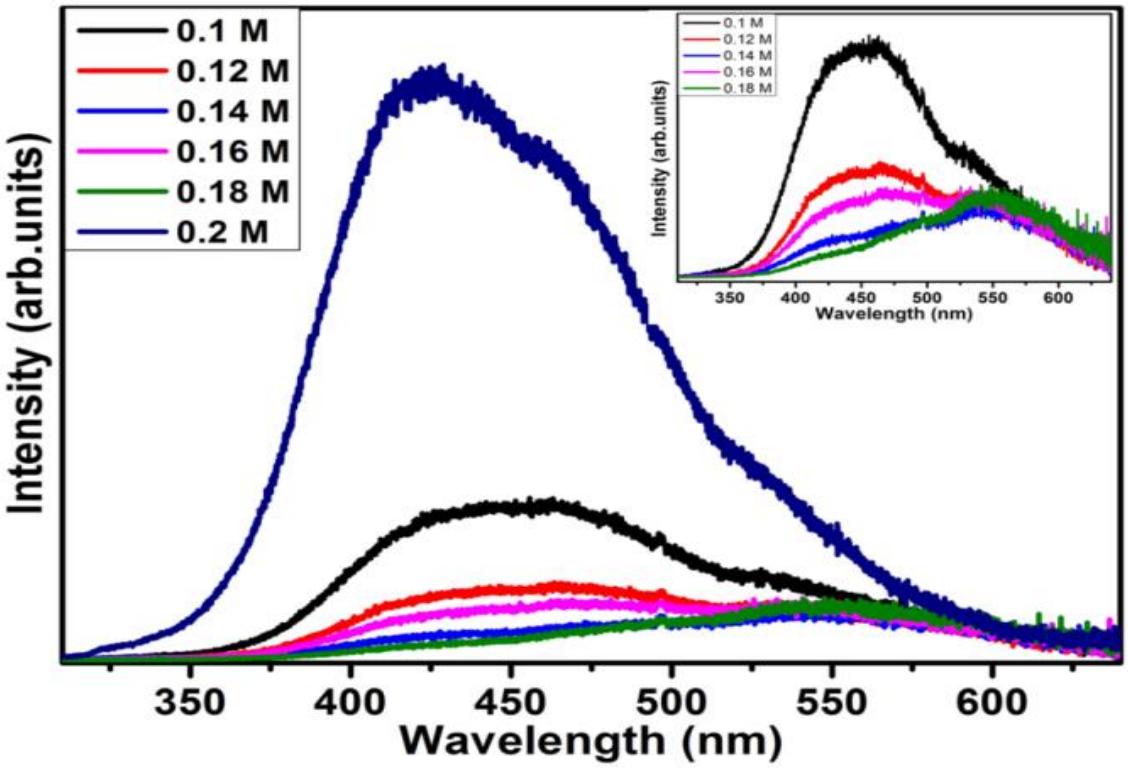

Figure 6.5 Room temperature PL spectra for ZnO flower-like structure prepared at different concentrations of ZnAc.

Gaussian fits were performed on the PL spectrum of ZnO prepared at 0.1 M ZnAc concentration as shown in **Figure 6.6**. The de-convoluted spectrum shows two peaks centred at ~ 440, and ~ 520 nm except the peak centred at ~ 450 nm observed in **Figure 6.5** above. It is well known that a visible emission of zinc originates from intrinsic and structural defects [17]. The blue emission is observed at ~ 440 nm because of surface defects in ZnO, this emission is attributed to Zn interstitials (Zni) [18]. The weak green emission observed at ~

520 nm is well attributed to singly ionized oxygen vacancy in ZnO [19]. The weak green emission at ~ 520 nm typically associated with the recombination of electrons trapped in singly ionized oxygen vacancy (V_o^+) with photo generated holes [20].

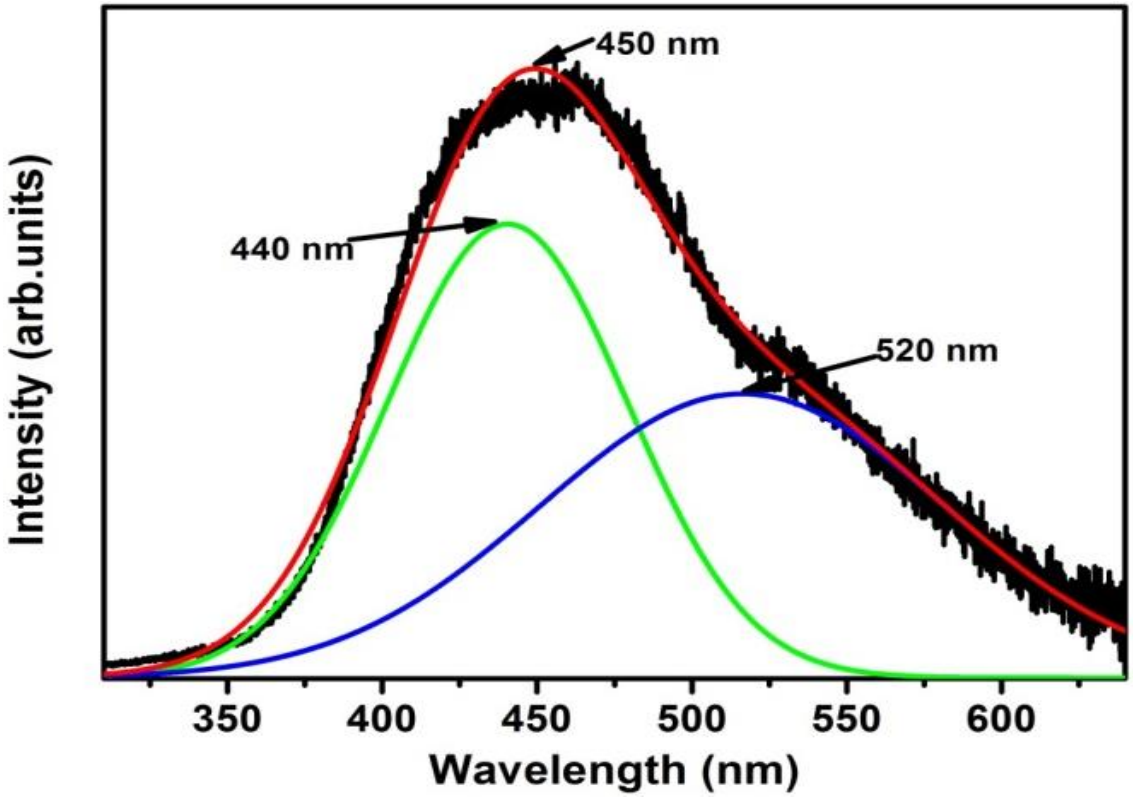

Figure 6.6 De-convoluted spectra of ZnO sample prepared at 0.1 M ZnAc concentration.

6.3 Conclusion

ZnO nanoparticles were successfully prepared using CBD method by varying molar concentrations of the ZnAc. There was no change in the crystalline size when increasing ZnAc concentration. Non-uniform flower-like structure indicated that the morphology cannot be completely controlled by the ZnAc concentration. UV-vis spectroscopy shows no appreciable change in band gap energy of the flower-like structure when the ZnAc concentration increases. PL showed that the emission of the ZnO nanoparticles also depends on the ZnAc concentration.

6.4 References

[1] V. Kumar, H.C. Swart, O.M. Ntwaeaborwa, R.E. Kroon, J.J. Terblans, S.K.K. Shaat, A. Yousif and M.M. Duvenhage, *Mat. Lett.* **101** (2013) 57 – 60

[2] S.M. Abrarov, S.U. Yuldashev, T.W. Kim, Y.H. Kwon, and T.W. Kang, *Optics Commun.* **259** (2006) 378 – 384

[3] D.M. Bagnall, Y.F Chen, Z. Zhu, T Yao, S Koyama, M.Y. Shen and T Goto, *Appl. Phys. Lett.* **70** (1997) 2230

[4] A.J. Meaney, *thesis*. Dublin City University,Glasnevin, Dublin 9, Ireland (2010) 105pp

[5] A.O. Awodugba, and A.O. Ilyas, *Asian J. Appl. Sci.* **2** (2013) 41 – 44

[6] L. Sepet, *et al. Def. Diff. Forum.* **312 – 315** (2011) 836 – 41

[7] Z.L. Wang, *Mat. Sci. Eng.* **64** (2009) 33 – 71

[8] L. Xu, Y Guo, Q Liao, J. Zhang and D. Xu *J. Phys. Chem*. **109** (2005) 13519

[9] V. Kumar, S. Som, V. Kumar, V. Kumar, O.M. Ntwaeaborwa, E. Coetsee and H.C Swart, *Chem. Eng. J. CEJ* **12266** (2014) 1 – 33

[10] Y.C. Lu, L.L. Wang, T.F, Xie, L.P. Chen and Y.H. Lin, *Mater. Chem. Phys*. **129** (2011) 281 – 87

[11] L.F. Koao, F.B. Dejene and H.C. Swart, *Mat. Sci. Sem. Proc*. **27** (2014) 33 – 40

[12] Cullity. B.D, Elements of X-ray Diffraction (Addison-Wesley Publishing Company, Inc., London, (1978)

[13] F.V. Molefe, L.F. Koao, J.J. Dolo and B.F. Dejene, *Physica B.* **439** (2014) 185 – 88

[14] D.E. Motaung, I. Kortidis, D. Papadaki, S.S. Nkosi, G.H, Mhlongo, J. Wesley-Smith, G.F. Malgas, B.W. Mwakikunga, E. Coetsee, H.C. Swart, G. Kiriakidise, and S.S. Ray *App. Surf Sci.* **311** (2014) 14 – 26

[15] N. Goswami and D.K. Sharma *Physica E*. **42 (**2010) 1675 – 82

[16] A. Mohanta and R.K. Thareja, *J. Appl. Phys*. **104** (2008) 044906

[17] K.G. Yim, M.Y. Cho, S.M. Jeon, M.S. Kim and J.Y. Leem *J. Korean Phys. Soc.* **58** (2011) 520 – 24

[18] S. Dutta, and B.N. Ganguly *J. Nanobiotech*. **10** (2012) 1 – 10

[19] M. Mazhdi, J. Saydi, M. Karimi, J. Seidi and F. Mazhdi, *Optik*. **124** (2013) 4128 – 4133

[20] C.Y. Lin, W.H. Wang, C-S. Lee, K.W. Sun, and Y.W. Suen, *Appl. Phys. Lett*. (2009) **94**151909 –151909-3

7

The influence of annealing temperature on luminescence properties of ZnO nanopowders prepared by chemical bath deposition method

7.1 Introduction

In the recent years wide band gap semiconductors such as ZnO are extensively studied by nano-scientists at the nanometer scale in order to optimize and widen the applications of nanomaterials. ZnO is a compound that is composed of group II and group IV elements, and it is mainly important because of its wide direct band gap of 3.37 eV and a large exciton binding energy of 60 meV [1]. Extensive experimental and theoretical studies have been conducted on ZnO due to its outstanding properties such as electrical, optical and luminescence which depends on the size of the nanomaterials [2 – 4]. ZnO is the active subject of research in nanoscience and nanotechnology [5], and it is commercially used as a phosphor for cathode ray tubes in flat panel displays [6]. Its applications include luminescent materials [7], and it consists of the visible light emission which is mainly important for white – light emitting diodes (WLEDs) [8].

Nano-sized ZnO materials have been prepared by various methods, such as wet chemical methods [9 – 10], combustion method [11], sol-gel method [12] and pulsed laser deposition (PLD) [13]. But these methods are too expensive, they take long periods to synthesize and usually require high temperature. The influence of the annealing temperature on the properties of ZnO has been reported by several research groups [14, 15]. But to the best of our knowledge, there is no report available on the influence of annealing temperature on the ZnO prepared using the chemical bath deposition (CBD) method on phosphor powder materials. Huang W-Y *et al.* [16] showed that the CBD method is good with crystal distribution for the formation of homogenous ZnO membrane and thermal annealing temperature has the effect of enhancing the crystal structure. Nehru *et al.* [17] reported the drastic increase in the blue emission intensity of ZnO influenced by the increase in annealing temperature.

In the present study, ZnO nanoparticles were synthesized by the CBD method, which is a simple approach with a low cost to synthesize ZnO nanoparticles at a low reaction

temperature. The CBD was the preferred choice because it is one of the solution phase methods useful for the preparation of compound semiconductors from aqueous solutions [18]. The effect of annealing temperatures on the crystal structure, morphology, optical and luminescence properties of ZnO synthesized by CBD are investigated. The novelty of this study lie's in the possibility that ZnO nanopowders with low intensity prepared by CBD method might be used as a source for blue light in LED's in future.

7.2 Results and discussions

7.2.1 Thermal TGA analysis

The TGA of the dried as-prepared ZnO nanopowders is shown in **Figure 7.1**. The TGA traces of the ZnO shows an initial ~ 4 % weight loss from 70 – 120 ℃, which is attributed to $Zn(OH)_2$ decomposition [19]. It is followed by gradual weight loss of 15 % from 120 - 160 ℃, which corresponds to the loss of surface adsorbed water. The further 2% weight loss in the range 220 – 350 ℃ is assumed to be due to decomposition of unreacted zinc acetate. A gradual weight loss of ~ 5 % is observed in the range 310 - 430 ℃ and is assigned to dehydration of residual ammonia and nitrate ions, and in the range 380 - 440 ℃ there is 3% weight loss which is due to the volatilization and combustible organic species present in the ZnO nanopowders [20]. The slightly clear plateau is observed in the temperature range 460 – 700 ℃ indicating that the ZnO nanopowders starts to become thermally stable without further weight loss. Hence the as-prepared ZnO nanopowders were annealed at 600 ℃ for crystallization. Motloung *et al.* [21] indicated that the minimum annealing temperature to start forming metal oxide such as ZnO is 400 ℃. Thus, the annealing temperature needs to be higher than 300 ℃ to remove all impurities and to improve the crystal structure of ZnO. These results agree with what is experimented in XRD analysis wherein $Zn(OH)_2$ peaks are removed after annealing and decomposed crystalline ZnO is formed by annealing at 600 ℃. The observed high residual yield could be due to the annealing temperature being just above the crystallization temperature of ZnO.

7.2.2 Thermal DSC analysis

Figure 7.2 shows the DSC spectra of the as-prepared ZnO nanopowders. The DSC spectra show an endothermic peak around 155 ℃ with the onset temperature of 153 ℃ together with

enthalpy of 240.55 J/g. The observed endothermic peak is attributed to conversion of zinc hydroxide to zinc oxide [22]. This illustrates that the decomposition of OH^- has taken place.

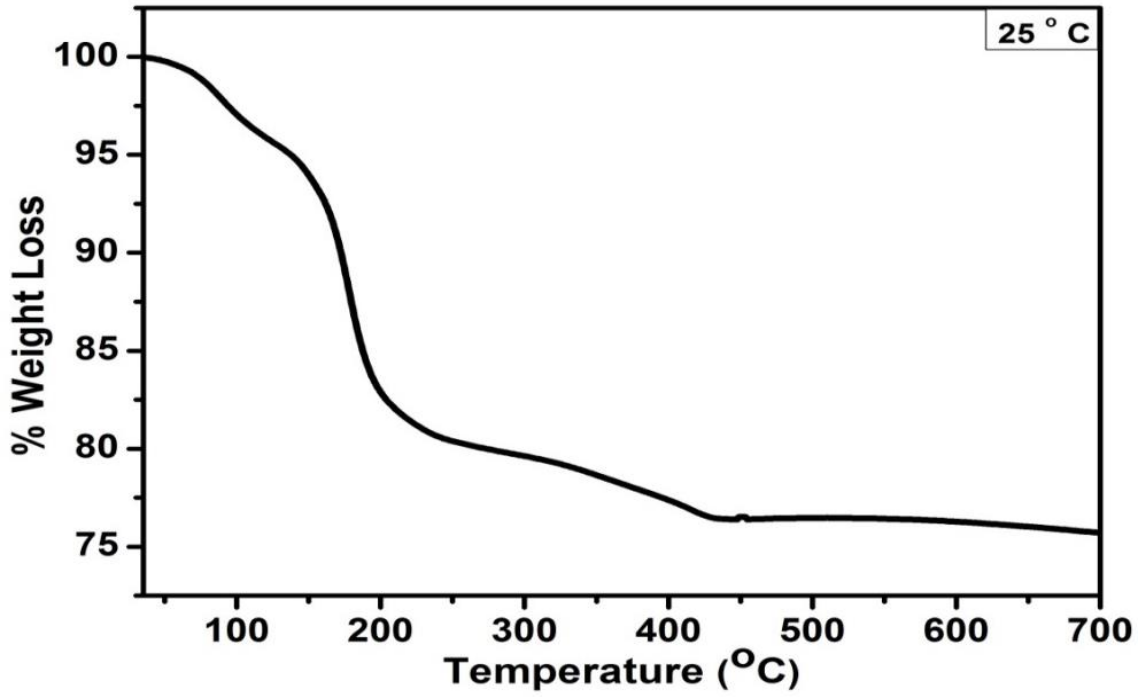

Figure 7.1 TGA spectra for thermal decomposition of as-prepared ZnO nanopowders.

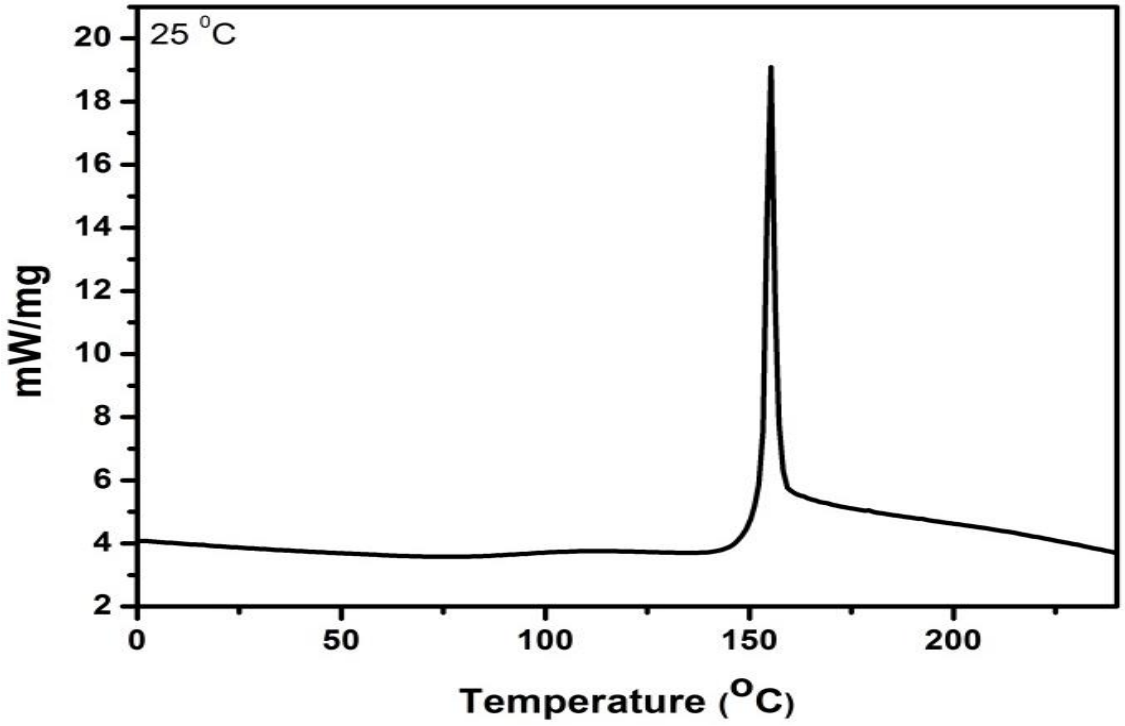

Figure 7.2 DSC spectra of thermal decomposition of as-prepared ZnO nanopowders.

7.2.3 XRD analysis

Figure 7.3 (a) shows typical XRD patterns of ZnO nanopowders prepared by the CBD method and dried at room temperature. These nanopowders were further dried at 300 ^{0}C and 600 ^{0}C to study the effect of annealing on the structure of ZnO. For the as-prepared ZnO nanopowders there are two diffraction peaks marked with asterisks at 2θ of 33.03 and 58.40 degrees attributed to $Zn(OH)_2$ impurities. It can clearly be seen from the spectrum that at room temperature the ZnO structure was still forming because the (002) diffraction peak was unresolved due to $Zn(OH)_2$ impurity lying next to it.

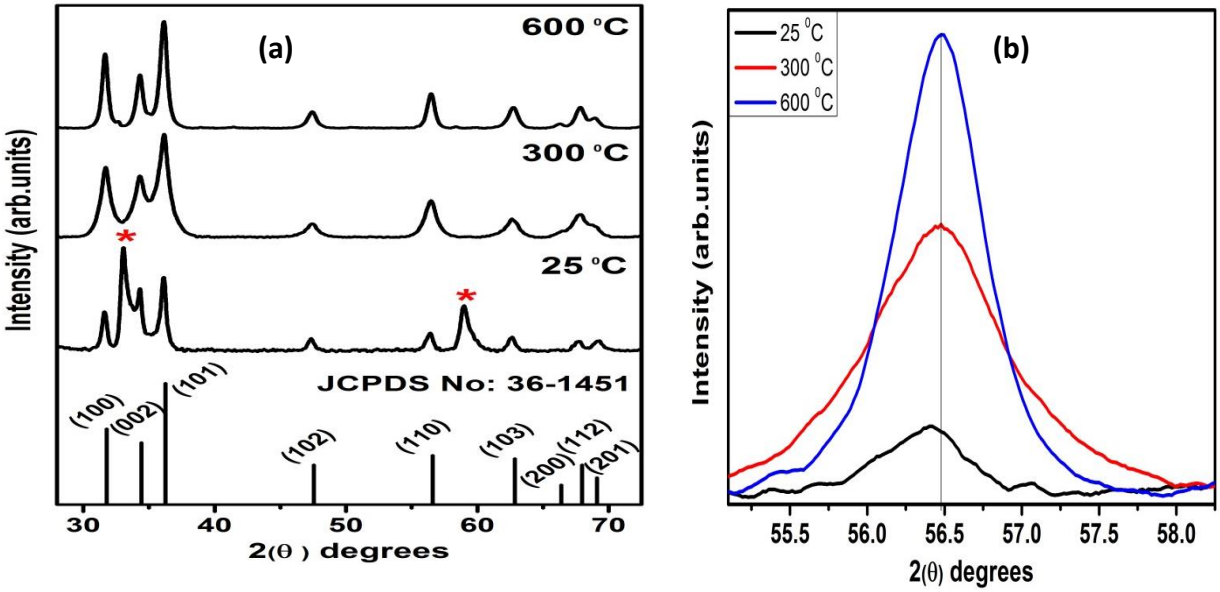

Figure 7.3 XRD pattern of **(a)** ZnO nanopowders prepared by CBD method annealed at different temperatures, **(b)** Detail of the (110) peak.

After annealing at 300 ℃ all the impurities were removed and ZnO diffraction peaks were intensified with the (200) peak still developing. For the ZnO nanopowders annealed at 600 ℃, all diffraction peaks are resolved. The XRD pattern at 600 ℃ clearly shows ZnO well consistent with hexagonal wurtzite structure with lattice constants a = 3.25 Å, c = 5.18 Å indexed to JCPDS card no. 36-1451. An improvement in ZnO crystallinity is observed for the ZnO nanopowders annealed at 600 ℃ and these results are consistent with that of TGA.

The average crystallite size of ZnO nanoparticles was evaluated using familiar Scherrer's equation [23]. The calculated average crystal sizes were in the range of 17 to 25 nm and were found to change with an increase in annealing temperature. The observations suggest that annealing ZnO nanopowders plays a role in formation of pure hexagonal ZnO structure.

Kumar *et al.* [24] indicated that as-prepared ZnO have an amorphous nature, while the annealed ZnO have a hexagonal wurtzite structure.

From **Figure 7.3 (b)** it is clearly seen that the (110) orientation of the ZnO nanopowders is slightly shifted to higher diffraction angle when the annealing temperature increases. This corresponds to the decrease in lattice spacing as $Zn(OH)_2$ decomposes into the ZnO. Lupan *et al.* [25] also observed the shift in diffraction angle to higher 2θ value with the increase in annealing temperature. Thus the diffraction peak becomes more intense and narrower with increasing annealing temperature indicating that the annealing temperature improves the crystallinity of ZnO. Peng *et al.* [8] observed a similar behaviour where the $Zn(OH)_2$ peaks disappear as the annealing temperature increases and the diffraction peaks of hexagonal ZnO becomes narrower and more crystalline as the annealing temperature increases.

7.2.4 SEM analysis

The SEM images of the as-prepared and annealed ZnO nanopowders are shown in **Figure 7.4**. The as-prepared nanopowders dried at room temperature shows clearly defined nanoflakes like morphology in the entire field of view. By annealing the ZnO nanopowders at 300 ℃ the nanoflakes can still be observed but oriented differently compared with the as-prepared nanopowders. With further annealing to high temperature of 600 ℃, ZnO nanoflakes become agglomerated as a result forming irregular shapes. Therefore ZnO surface morphology deforms with increasing annealing temperature. Raoufi e*t al.* [3] on the study of the effect of annealing temperature on the morphology of ZnO nanoparticles indicated that as the annealing temperature increase the ZnO nanoparticles aggregates and becomes larger in diameter due to the increase in the reaction rate at higher annealing temperature [26].

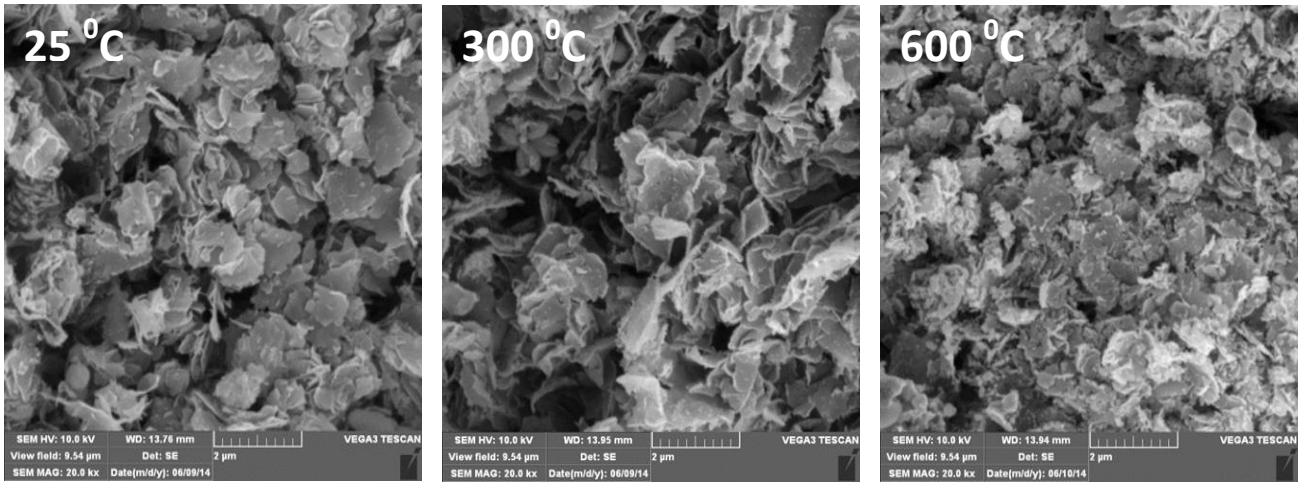

Figure 7.4 SEM images of ZnO nanopowders annealed at different temperatures.

7.2.5 XPS analysis

The surface and sub-surface elemental composition, defect analysis and oxidation states of ZnO prepared using CBD method at room temperature and ZnO annealed at different temperatures were investigated by the XPS technique. **Figure 7.5** shows three XPS survey scans of the as-prepared and annealed ZnO nanopowders **(a)** before 30 s of Ar^+ sputtering and **(b)** after 30 s of Ar^+ sputtering, obtained before acquiring high resolution scans for Zn and O. This survey scans we acquired with 100 µm 25 W 15 kV Al monochromatic x-ray beam. As presented in both **Figure 7.5 (a)** and **(b)**, only photoelectron peaks of the main elements namely C, O and Zn and Auger O KLL and Zn LMM were detected for as-prepared and annealed samples. The detected carbon is mainly referable to the carbon tape used to mount the samples and the carbon adsorbed on the surface the moment samples were exposed to ambient atmosphere. We observed no peaks indicating contaminants in our material. The binding energy (BE) scale for all the spectra was calibrated for the charge shift using the adventitious carbon (C - 1s) peak centred at 284.6 eV as reference [24,27].

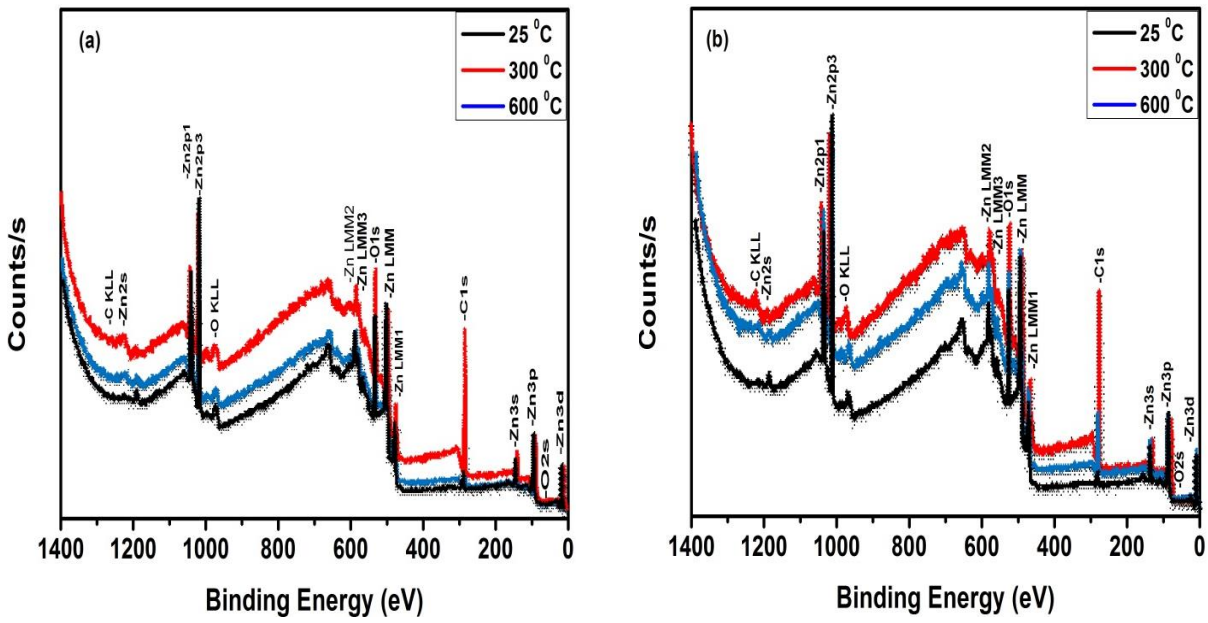

Figure 7.5 XPS broad survey scans of as-prepared ZnO nanopowders and that annealed at different temperatures **(a)** before sputtering **(b)** after 30 s of Ar^+ sputtering.

The chemical state of Zn in ZnO nanopowders is analysed in details by investigating the Zn 2p peak as presented in **Figure 7.6**. As shown in both **Figure 7.6 (a)** and **(b)** the high resolution spectra of the as-prepared and annealed ZnO nanopowders in the Zn 2p region

revealed two photoelectron peaks. From the as-prepared samples we observed metallic Zn with (BE) of 1021.5 and 1044.5 eV corresponding to Zn atoms at regular lattice sites in the ZnO crystal [28]. The doublet was observed at (BE's) of 1021.2 and 1044.2 eV for annealed samples corresponding to the energies of Zn-$2p_{3/2}$ and Zn-$2p_{1/2}$, respectively [29]. However, we observed a slight shift in Zn 2p peak positions between as-prepared and annealed samples before and after Ar^+ sputtering. The chemical shift in the peak positions from high energy towards low energy as the annealing temperature increased was caused by alterations in charge transfer from Zn^{2+} to O^{2-} ions caused by vacancies [30]. Tay *et al.* [31] explained that, in the presence of O vacancies, the amount of charge transferred from Zn^{2+} to O^{2-} ions would be effectively lesser, thus shifting the (BE) of Zn 2p to lower values. The average doublet (BE) separation between the vertical reference lines was measured for annealed samples and found to be 23.0 eV, which lies nearer to the standard reference value of ZnO [27]. The calculated doublet (BE) separation and the measured (BE) values in Zn 2p peaks for annealed samples, show that the Zn atoms are in the Zn^{2+} oxidation state. Kushwaha *et al.* [32] reported the shift of Zn 2p peaks to higher (BE) for ZnO annealed in oxygen.

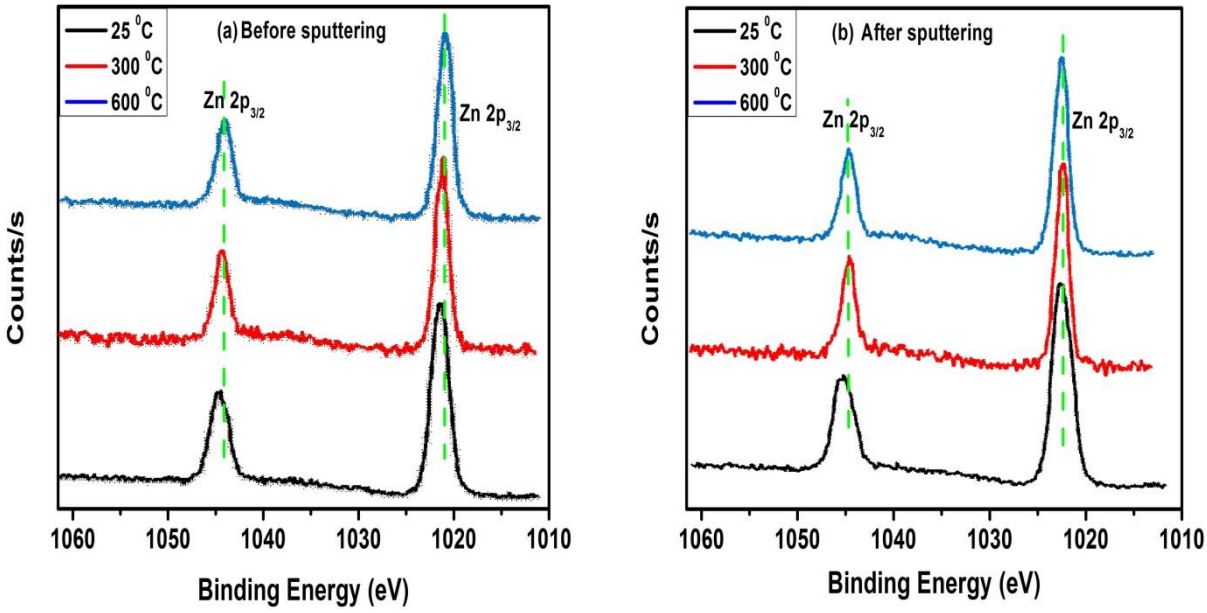

Figure 7.6 High resolution XPS spectra of Zn 2p core levels corresponding to as-prepared ZnO nanopowders and that annealed at different temperatures **(a)** before sputtering **(b)** after 30 s of Ar^+ sputtering.

The deconvoluted spectra of O 1s peak for as-prepared and annealed ZnO nanopowders fitted using Gaussian functions with the help of Multipak 8.2C software are shown in **Figure 7.7**.

The high resolution spectra of the O 1s peaks were acquired before and after 30 s of Ar^+ ions sputtering. The asymmetric O 1s peak for the as-prepared as well as annealed samples consists of three components: O_1, O_2 and O_3 respectively as shown in **Figure 7.7**. The corresponding peak positions are presented in **Table 7.1**.

Table 7.**1** Peak positions of different O1s peaks before and after 30 s Ar^+ ions sputtering.

Annealing Temperature (℃)	Peak name	Before sputtering	After sputtering
		Peak position (eV)	Peak position (eV)
As-prepared	O_1	528.7	528.5
	O_2	530.0	530.0
	O_3	531.2	531.4
Annealed (300)	O_1	529.4	529.3
	O_2	530.7	530.3
	O_3	531.9	531.5
Annealed (600)	O_1	530.8	531.0
	O_2	531.5	-
	O_3	532.7	532.6

The three fitted (BE) peaks approximate the results of Lupan *et al.* [25], Wang Z.G *et al.* [33] and Wang H *et al.* [34], who observed the shift in the peak positions when the annealing temperature was increased. The (BE) (O_1 peaks) around 528.5 – 528.7 observed in the as-prepared samples can be ascribed to oxygen from H-ZnO surface [35]. The peak positioned around 529.3 and 531.4 originates from the lattice oxygen and the defect oxygen such as that in vacancies, respectively [36 – 40]. Hence, the changes in the intensity of this component may be partially linked to the fluctuations in the concentration of oxygen defects (V_o and O_i) [11]. Bar *et al.* [41] indicated that one can find the (BE) of O 1s for ZnO between 530.0 – 530.9 eV and for $Zn(OH)_2$ between 531.5 – 532.3 eV. The component on the highest (BE) side (O_3) corresponds to chemisorbed or dissociated oxygen or hydroxyl (OH^-) species (such as CO_3 and O_2) on the surface of the ZnO [42 – 43]. The intensity of O_1 peak increased with the increase in annealing temperature before and after Ar^+ ion sputtering which indicates strong Zn-O bonding.

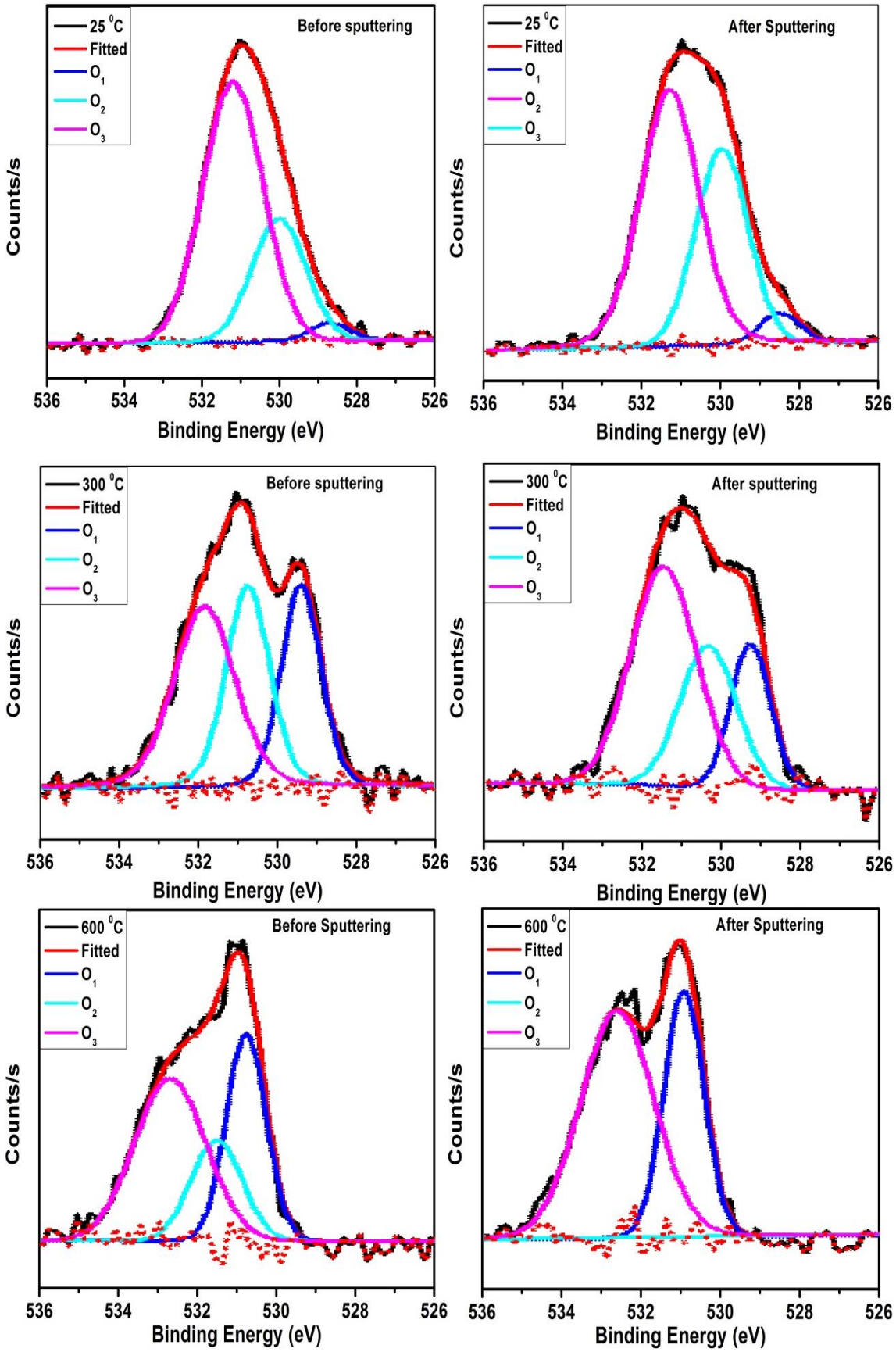

Figure 7.7 Deconvoluted O 1s spectra of as-prepared and annealed ZnO nanopowders obtained before and after Ar+ sputtering.

It can be seen from **Figure 7.7** and **Table 7.1** that the binding medium (BE) O_2 peak is present in all the samples except the ZnO annealed at 600 ℃ after Ar^+ sputtering. The intensity of the O_3 peak decreased with the increase in annealing temperature before and after Ar^+ sputtering except for sample annealed at 600 after Ar^+ sputtering due to decreased O_2 intensity. Furthermore the intensity of O_3 peak has decreased after sputter cleaning due to the removal of surface contaminants. This implies that, the high BE component can be removed in part by thermal treatment and Ar^+ ion sputtering.

7.2.6 UV-vis analysis

Figure 7.8 shows the UV-vis reflectance spectrum in the wavelength range of 200–800 nm for the as-prepared and annealed ZnO nanopowders. As illustrated there is a slight redshift of the absorption edge with an increase in the annealing temperature, due to the size effect of nanostructures [44]. Hence the observed redshift corresponds with the variation of the nanoparticle sizes as reported by Irimpan *et al.* [45]. Lupan *et al.* [25] also observed the redshift in the absorption edge as the annealing temperature increases.

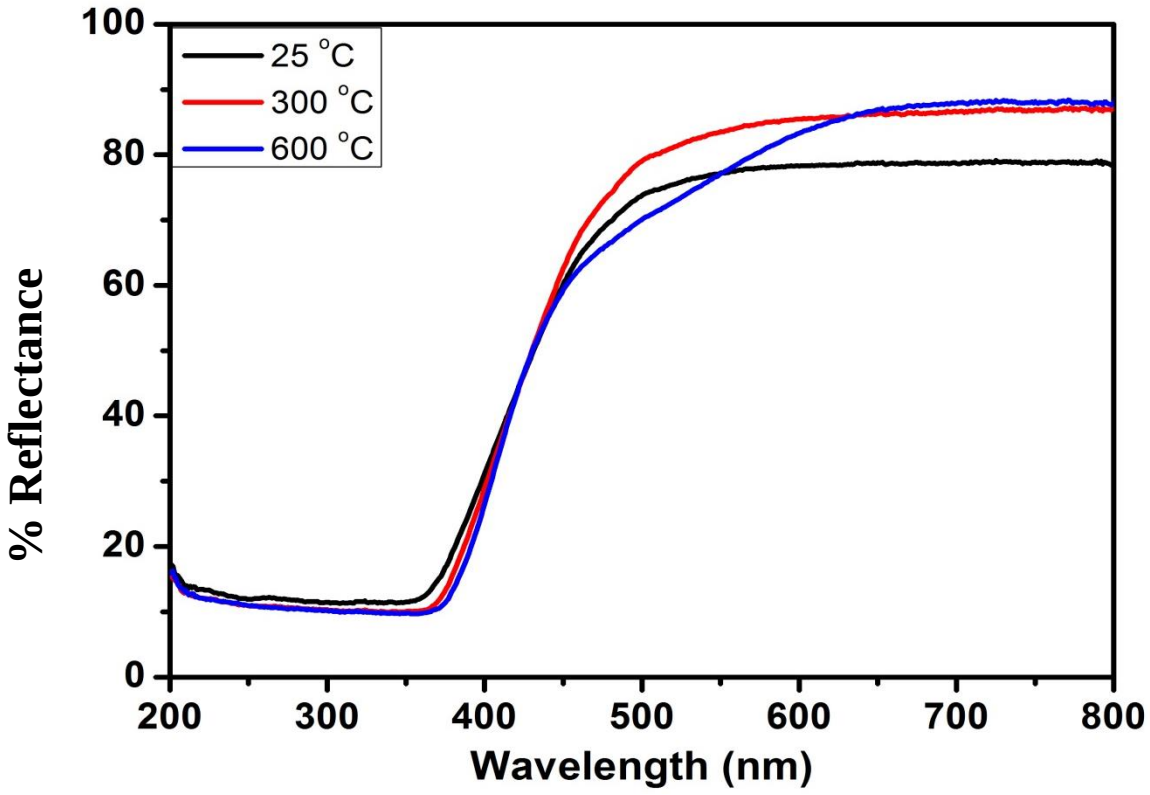

Figure 7.8 UV-vis reflectance spectra for ZnO nanopowders annealed at different temperatures.

The energy band gap of these materials was estimated using the Kubelka–Munk remission function (7.1) [18],

$$K = \frac{(1-R)^2}{2R} \qquad (7.1),$$

where K represents reflectance transformed according to Kubelka–Munk, R is the percentage (%) reflectance, hv is the photon energy and E_g is the band gap energy at n = 2 for direct transitions. The optical (E_g) for the ZnO powders was calculated by extrapolating the linear portion of the graph to $(Khv)^2$ = 0 as shown in **Figure 7.9**. The average band gap of ZnO was determined as 3.21 ± 0.02 eV for all the nanopowders. The band gap energy slightly decreased when the annealing temperature increased. The decrease in band gap can be attributed to the increase of particle size [46]. Therefore, the red shift of the optical absorption edge to the lower energy should be related to the band gap narrowing.

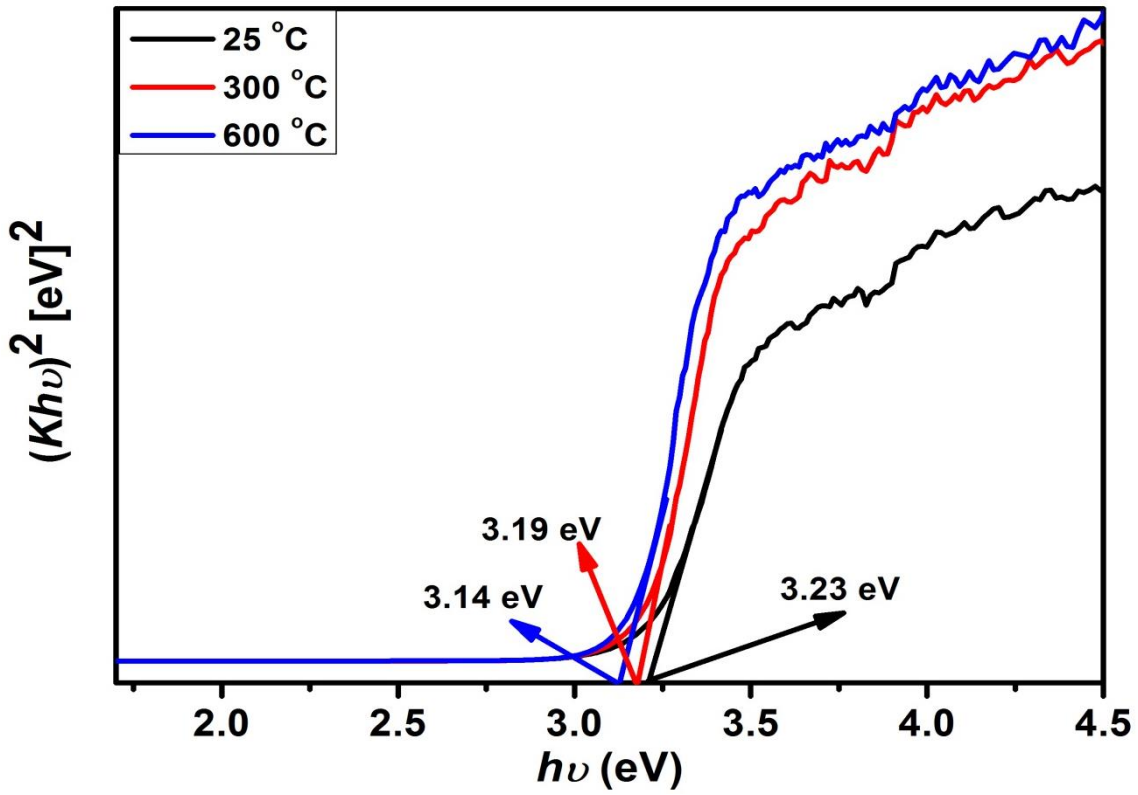

Figure 7.9 Plot to determine band gap energies of ZnO nanopowders.

7.2.7 Photoluminescence Analysis

Figure 7.10 show the PL spectra of ZnO nanopowders recorded at room temperature in the wavelength range 310 – 650 nm. A strong broad DLE which extends from the UV region to

the visible region is observed in **Figure 7.10 (a)** for the as-prepared nanopowders. This broad emission is de-convoluted into three Gaussian type sub-peaks centered at ~ 415, ~ 473 and ~ 550 nm, which originates from structural defects [47]. The maximum ultraviolet-blue peak is observed at ~ 415 nm and the blue emission peak is observed at ~ 473 nm. We assume that these two emission peaks originates from $Zn(OH)_2$ because XRD results confirmed the presence of $Zn(OH)_2$ as an impurity. TGA results showed that the amount of $Zn(OH)_2$ decay with an increase in annealing temperature. The weak yellow emission is observed at 550 nm typically associated with the (V_O) [48].

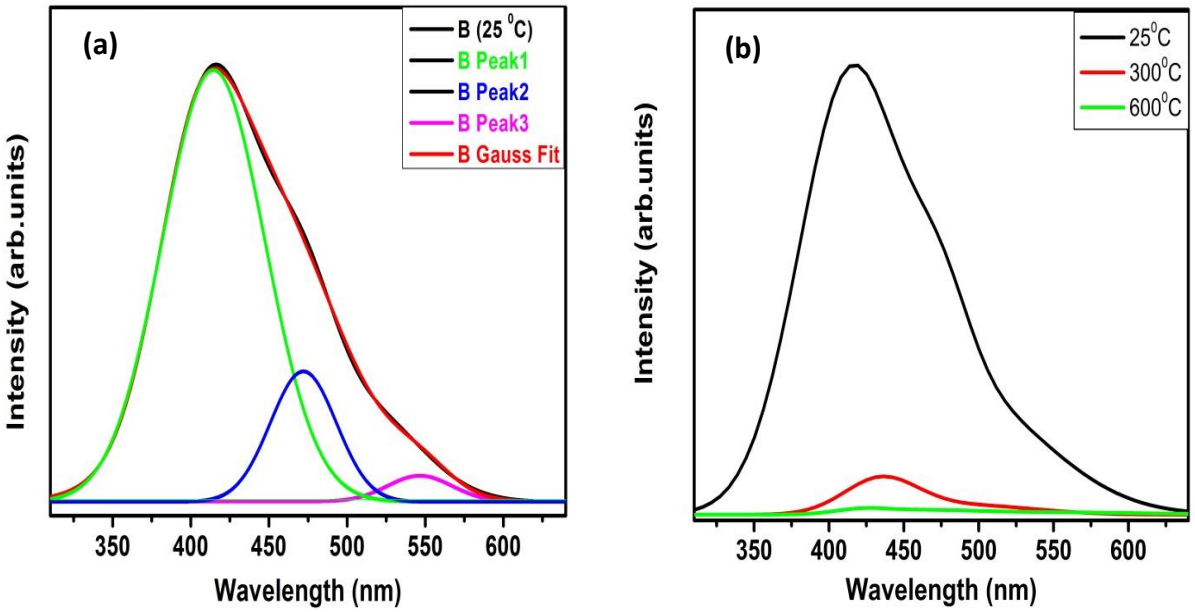

Figure 7.10 PL spectra of ZnO prepared by CBD method **(a)** de-convoluted spectra for the as-prepared ZnO nanopowders, **(b)** as-prepared ZnO nanopowders and ZnO nanopowders annealed at various temperatures.

Figure 7.10 (b) shows the comparison between as-prepared and the annealed ZnO nanopowders to study the influence of annealing temperature on ZnO nanopowders. The as-prepared ZnO has the maximum intensity positioned at 415 nm, a decrease in luminescence intensity is observed for the ZnO nanopowders annealed at 300 ℃. This sudden decrease in luminescence intensity may be due to the decrease in $Zn(OH)_2$ content as the annealing temperature increases [49]. It can be seen that after annealing at 300 ℃ the small emission peak at 430 nm appears in the range 400 – 500 nm. The 430 nm emission is induced by the electron transition between the shallow level of zinc interstitials Zn_i and the valence band [50]. Finally, after annealing at 600 ℃ we observed further quenching of the blue

luminescent efficiency now positioned at 440 nm. This 440 nm blue emission also originates from the level of Zn_i to valence band regulated by transition of excited electrons. This observation confirms Zeng *et al.* [51] results, who indicated that the extended Zn_i states can be formed during annealing process due to the defect ionization reaction. Therefore concentration of Zn_i related defects is drastically decreased. The broad intense blue emission observed in this study is promising for fluorescent materials. Zeng *et al.* [52] confirmed the viability of blue light source efficient for semiconductor UV emitters. The UV excitonic emission is not resolved in the presented results; Kundu *et al.* [53] indicated that UV emission cannot appear if there is high intensity of visible emission due to increased defect density. Because as the annealing temperature increases the luminescence intensity quenches, the weaker emission for the ZnO nanopowders annealed at 600 ℃ is an indication of higher crystalline quality [54], and it is confirmed by the XRD results.

In **Figure 7.11 (a)** we have the normalized PL emission spectrums for the as-prepared and annealed ZnO nanopowders to study the effect of annealing temperature on the peak positions. Three emission peaks can be seen at various wavelengths ~ 415, ~ 430, ~ 440 nm in the blue region. There is a redshift in the peak positions as the annealing temperature is increased and this observation agrees with the reflectance measurements. Peng *et al.* [8] managed to obtain yellow emission around 580 nm for as-prepared samples and he associated that emission with $Zn(OH)_2$, after annealing those samples the yellow emission disappears and meanwhile a green emission peak at around 490 nm occurs, which is due to known V_o. Other researchers also proved that the annealing treatment modify the green emission [55].

In our work (**Figure 7.11 (a)**) we were able to observe the redshift in UV region as the annealing temperature increased and again at 600 ℃ there was modification of DLE at around ~ 550 nm. The defect-related visible emission around ~ 550 nm is related to V_o. It is believed that this phenomenon is due to band transitions from Zn_i to V_o defect levels in ZnO [46]. The observed redshift in the position of the band edge emission is due to band gap narrowing as the annealing temperature increases [56]. After annealing at 600 ℃ the spectrum shifted back to 430 nm, and this blue shift is due to band renormalization and band filling [57]. **Figure 7.11 (b)** illustrates the Commission Internationale de l'Eclairage (CIE) chromaticity diagram of as-prepared and annealed ZnO nanopowders calculated using photoluminescence data and color calculator software. It can be seen from the figure that the

PL CIE coordinates (x, y) of (0.181, 0.260), (0.212, 0.268) and (0.233, 0.273) correspond to 25, 300 and 600 ℃, respectively with the shade of the blue region. The coordinates for the annealed samples are shifted a bit toward the near white light from the as-prepared sample. This is because the emission peaks in **Figure 7.11 (a)** are red-shifted compared to as-prepared sample. Thus, this results shows that the ZnO emission can be tuned by annealing.

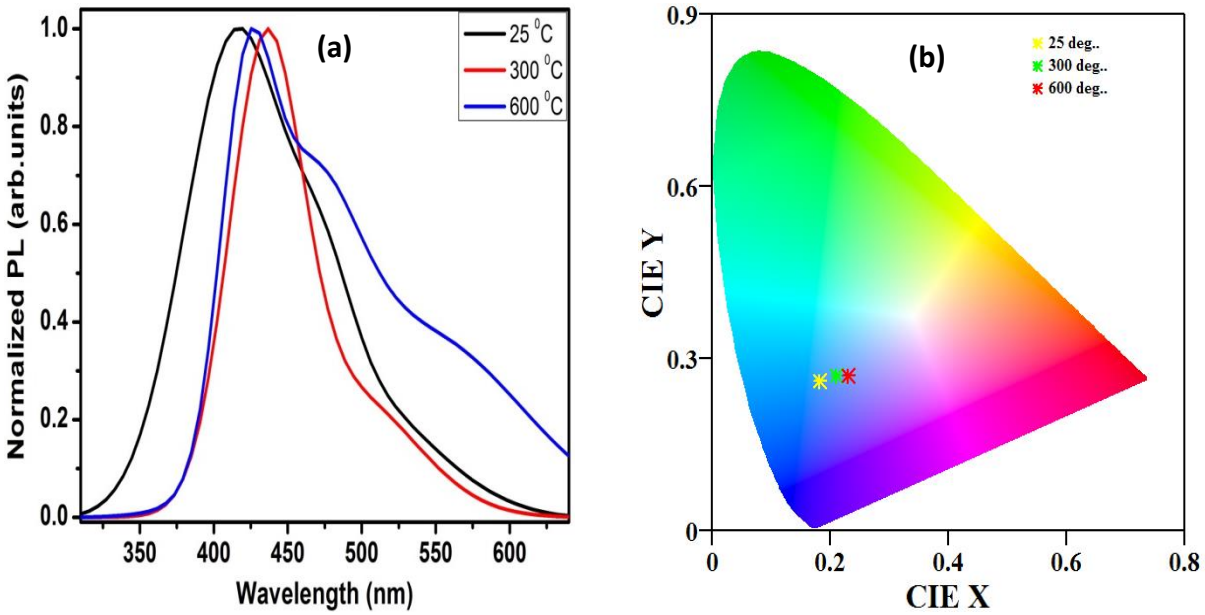

Figure 7.11 (a) Normalized PL emission spectrum of as-prepared and annealed ZnO nanopowders to study the effect of annealing, **(b)** CIE diagram of ZnO nanopowders annealed at various temperatures.

7.3 Conclusion

In this study CBD method was employed to synthesize ZnO nanopowders using zinc acetate and thiourea as the solutes and Ammonia and deionized water as solvents. Thermal studies were carried out by TGA and DSC for the decomposition of ZnO. XRD results showed improved crystallinity of hexagonal wurtzite structure of ZnO nanopowders. ZnO nanopowders of flakes like morphologies were successfully fabricated at 80 ℃, hence the annealing temperature has an influence on morphology of ZnO particles. XPS measurements confirmed presence of V_o observed in PL results. The UV-Visible study showed the red shift in the absorption edge. The direct band gap energy of ZnO nanopowders was found to be 3.21 ± 0.02 eV less as compared to their bulk counterpart. The luminescent properties of ZnO were studied. PL spectrum showed broad DLE from ultraviolet blue to green region. The luminescence intensity decreased with increasing annealing temperature.

7.4 References

[1] V. Ghafouri, A. Ebrahimzad and M. Shariati, *Scientia Iranica F*. **20** (2013) 1039 – 1048

[2] U. Seetawan, S. Jugsujinda, T. Seetawan, C. Euvananont, C. Junin, C. Thanachayanont, P. Chainaronk and V. Amornkitbamrung *Solid State Sciences* **13** (2011) 1599 – 1603

[3] D. Raoufi *Renewable Energy* **50** (2013) 932 – 937

[4] Vinod Kumar, S. Som, Vijay. Kumar, Vinay. Kumar, O.M. Ntwaeaborwa, E. Coetsee and H.C. Swart, *Chem. Eng. J.* **255** (2014) 541 – 552

[5] C. Burda, X. Chen, R. Narayanan and M.A. E1-sayed, *Chem. Rev.***105** (2005) 1025

[6] T.V. Prevenslik, *J. Lumin.* **1210** (2000) 87 – 89

[7] N. Hagura, T. Ogi, T. Shirahama, F. Iskandar and K. Okuyama, *J. Lumin.* **131** (2011) 921 – 925

[8] W.Q. Peng, S.C. Qu, G.W. Cong and Z.G. Wang, *Mat. Sci. Semicon. Proc*. **9** (2006) 156 – 159

[9] M.A. Verges, A. Mifsud and C.J. Serna, *J. Chem. Soc., Faraday Trans.* **86** (1990) 959 – 963

[10] L. Vayssieres, K. Keis, S.E. Lindquist and A. Hagfeldt, *J. Phys. Chem. B.* **105** (2001) 3350 – 3352

[11] V. Kumar, H.C. Swart, O.M. Ntwaeaborwa, R.E. Kroon, J.J. Terblans, S.K.K. Shaat A. Yousif and M.M. Duvenhage, *Mat. Lett.* **101** (2013) 57 – 60

[12] A.G. Ali, F.B. Dejene and H.C. Swart, *Cent. Eur. J. Phys.* **10 (**2012) 478 – 484

[13] J.I. Hong, J. Bae, Z.L. Wang and R.L. Snyder, *Nanotechnology* **20** (2009) 085609 – 085613

[14] V. Kumar, N. Singh, A. Kapoor, O.M. Ntwaeaborwa and H.C. Swart, *Mater. Res. Bull.* **48** (2013) 4596 – 4600

[15] T.M. Hammad, J.K. Salem and R.G. Harrison *Superlattice. Microst.* **47** (2010) 335 – 340

[16] W-Y. Haung, T-L. Hsieh, A-K. Chu, *J. Infor. Eng. App.* **2** (2012) 27 – 34

[17] L.C. Nehru and C. Sanjeeviraja, *J. Ceram. Process. Res*. **14** (2013) 712 – 716

[18] P. Duran, F. Capel, J. Tartaj and C. Moure, *Adv. Mater.* **14** (2002) 137

[19] Y. Khan, S.K. Durrani, M. Mehmood, J. Ahmad, M.R. Khan and S. Firdous, *App. Surf. Sci.* **257** (2010) 1756 – 1761

[20] S. Bagheri, K.G. Chandrappa and S.B.A. Hamid, *Der. Pharma. Chemica*. **5** (2013) 265 –270

[21] S.V. Motloung, B.F. Dejene, H.C. Swart and O.M. Ntwaeaborwa, *J. Sol-Gel Sci. Technol.* **70** (2014) 422 – 427

[22] H. Kumar and R. Rani, *Inter. Lett. Chem. Phy. Astro.* **14** (2013) 26 – 36

[23] H.P. Klong and L.E Alexander, X-ray Diffraction Procedures for Crystalline and Amorphous Materials. *Wiley: New York*. (1954) 491 – 538

[24] Vinod Kumar, Vijay Kumar, S. Som, A. Yousif, N. Singh, O.M. Ntwaeaborwa, A. Kapoor and H.C. Swart, *J. Colloid Interface Sci.* **428** (2014) 8 – 15

[25] O. Lupan, T. Pauporte, L. Chow, B. Viana, F. Pelle, L.K. Ono, B.R. Cuenya and H. Heinrich, *Appl. Surf. Sci.* **256** (2010) 1895 – 1907

[26] Z. Liu, C. Liu, J. Ya and E. Lei, *Solid State Sci.* **12** (2010) 111 – 114

[27] J.F. Moulder, W.F. Strickle, P.E. Sobol and K.D. Bomben, Handbook of X-ray Photoelectron Spectroscopy, (*Chigasaki: ULVAC-PHI, Inc*) (1995)

[28] M.N. Islam, T.B. Ghosh , K.L. Chopra and H.N. Acharya, *Thin Solid Films* **280** (1996) 20 – 25

[29] D.E. Motaung *et al. Appl. Surf. Sci.* **311** (2014) 14 – 26

[30] R.K. Sahu, K. Ganguly, T. Mishra, M. Mishra, R.S. Ningthoujam, S.K. Roy and L.C. Pathak, *J. Colloid Interface Sci.* **366** (2012) 8 – 15

[31] Y.Y. Tay, S. Li, C.Q. Sun and P. Chen *Appl. Phys. Lett.* **88** (2006) 173118

[32] A. Kushwaha, H. Kalita and M. Aslam, *World Academy of Science, Engineering and Technology*. **7** (2013) 254 – 259

[33] Z.G. Wang, X.T. Zu, S. Zhu, L.M. Wang, *Phys. E* **35** (2006) 199 – 202

[34] H. Wang, S. Dong, X. Zhou, X. Hu and Y. Chang *Phys. E* **44** (2011) 307 – 312

[35] L-L. Yang, Q. Zhao, M. Willander, X. Liu, M. Fahlman and J.H. Yang, *Crystal Growth and Design* **4** (2010) 1904 – 1910

[36] T. Jun, K. Song, Y. Jeong, K. Woo, D. Kim, C. Bae and J. Moon *J. Mater. Chem*. **21** (2011) 1102 – 1108

[37] G.H. Mhlongo, D.E. Motaung, S.S. Nkosi, H.C. Swart, G.F. Malgas, K.T. Hillie and B.W. Mwakikunga *Appl. Surf. Sci.* **293** (2014) 62 – 70

[38] D.I. Son *J. Korean Phys. Soc*.**55** (2009) 1973 – 1976

[39] R. Al-Gaashani, S. Radiman, A.R. Daud, N. Tabet and Y. Al-Douri *Ceram. Int.* **39** (2013) 2283 – 2292

[40] P.T Hsieh, Y.C. Chen, K.S. Kao and C.M. Wang, *Appl. Phys. A.* **90** (2008) 317 – 321

[41] M. Bär, J. Reichardt, I. Sieber, A. Grimm, I. Kötschau, I. Lauermann, S. Sokoll, M.C. Lux-Steiner, and Ch.-H. Fischer, *J. Appl. Phys.* **10** (2006) 1 – 9

[42] T.P. Rao, M.C.S. Kumar, A. Safarulla, V. Ganesan, S.R Barman and C Sanjeeviraja *Phys. B* **405** (2010) 2226

[43] Vinod Kumar, H.C. Swart, M. Gohain, Vijay Kumar, S. Som, B.C.B. Bezuindenhoudt and O.M. Ntwaeaborwa, *Ultrasonics Sonochemistry* **21** (2014) 1549 – 1556

[44] P.K. Samanta, S.K. Patra, A. Ghosh and P.R. Chaudhuri *I. J. N. N.* **1** (2009) 81 – 90

[45] L. Irimpan, V.P.N. Nampoori, P. Radhakrishnan, A. Deepthy and B. Krishnan *J. Appl. Phys.* **102** (2007) 063524 – 063529

[46] T. Pandiyarajan, M.L. Baesso and B. Karthikeyan, *Eur. Phys. J. D* **68** (2014) 28 – 36

[47] K.G. Yim, M.Y. Cho, S.M. Jeon, M.S. Kim and J.Y. Leem, *J. Korean Phy. Soc.* **58** (2011) 520 – 524

[48] Kumar S and Sahare P.D 2012 *Opt. Commun.***285** 5210 – 5216

[49] Q. Wang, G. Wang, J. Jie, X. Han, B. Xu and J.G. Hou, *Thin Solid Films* **492** (2005) 61 – 65

[50] Y. Lai, M. Meng, Y. Yu, X. Wang and T. Ding, *Appl. Catal. B: Enironmental* **105** (2011) 335 – 345

[51] H.B. Zeng. *et al. Adv. Func. Mater.* **20** (2010) 561 – 572

[52] H. Zeng, W. Cai, P. Liu, X. Xu, H. Zhou, C. Klingshirn and H. Kalt, *Acsnano* **2** (2008) 1661 – 1670

[53] T.K. Kundu, N. Karak, P. Barik and S. Saha, *Int. J. Soft. Com. Eng.* **1** (2011) 19 – 24

[54] G. Patwari, B.J. Bodo, R. Singha and P.K. Kalita *Res. J. Chem. Sci.* **3** (2013) 45 – 50

[55] H.Y. Lu, S.Y. Chu and S.S. Tan, *J.Cryst.Growth* **269** (2004) 385 – 391

[56] E.S. Shim, H.S. Kang, S.S. Pang, J.S. Kang, I. Yun and S.Y. Lee, *Mat. Sci. Eng.* B **102** (2003) 366 – 369

[57] S. Xu and Z.L. Wang *Pure Appl. Chem.* **83** (2011) 2171 – 2198

8

Summary and Future Work

Conclusion

In this thesis, the preparation of ZnO nanostructures using a cost-effective, simple and environmentally friendly synthesis technique (chemical bath deposition) was studied successfully. These inorganic semiconductors were prepared at different parameters such as reaction temperature, reaction time, concentration of the precursors and annealing temperature. The whole idea for preparing this material was to optimize growth conditions for ZnO and to investigate its luminescence properties. The salient results are summarized in this chapter and the conclusion is drawn from investigations.

From TGA results $Zn(OH)_2$ decomposed into ZnO and we observed significant weight loss due to removal of adsorbed species and the thermal stability was improved when increasing both reaction and annealing temperatures. In both cases, the degradation process started at ~ 100 ℃ and ceased at ~ 440 ℃, whereby crystallization of ZnO begins. The DSC analysis of the samples attests on the endothermic reaction that took place. The melting temperatures were observed to decrease with the increase in reaction temperature due to crystallization of ZnO.

The XRD spectra of the samples prepared at low reaction temperature, time, precursor concentration and annealing temperature respectively, confirmed the initial formation of $Zn(OH)_2$ structure, and hexagonal wurtzite structure emerged with the increase in reaction temperature, time, precursor concentration and annealing temperature. The formation of hexagonal ZnO is due to decomposition of $Zn(OH)_2$ through nucleation and crystallization mechanism. Too much (increase in) concentration of the precursor resulted into extra peaks which are due to unreacted zinc acetate. During the formation of hexagonal wurtzite structure the particle size was increased and crystallinity of ZnO was improved.

The SEM observations of ZnO nanostructures showed the formation of flakes like morphology. At higher reaction temperature, time, precursor concentration and annealing

temperature respectively, these nanoflakes were highly agglomerated. But the precursor concentration and reaction temperature were shown to have strong influence on diameter of the flakes. EDS results confirmed the presence of Zn and O, and their contents increased as ZnO crystallizes.

The optical properties of the nanostructures were investigated; it was found that the reflectance spectra depict a red shift of the absorption edge when increasing reaction time and the band gap energies decreases due to confinement effects. But for low precursor concentration we observed no appreciable change in absorption edges and band gap energy of the nanoflakes. When evaluating the effect of reaction temperature form 55 – 80 ℃, absorption edges shifts to the high wavelength. The same behaviour was observed with the annealed samples and the direct band gap energy of ZnO nanoflakes was found to be less as compared to their bulk counterpart.

The room temperature PL characteristics were also systematically studied. In the case of reaction time blue symmetric emission at 473 nm was observed while precursor concentration reveals dominant blue asymmetric emission at ~ 450 nm. From temperature dependent PL of the annealed samples and samples prepared at different reaction temperatures we observed strong broad DLE which extends from the ultraviolet region to the visible region. It is illustrated that this emission quenches and shifts to the higher wavelength as $Zn(OH)_2$ decomposes into ZnO. It has been reported that when using chemical methods such as CBD the emission intensity quenches as $Zn(OH)_2$ dehydrates into ZnO. The broadening of the visible emissions in ZnO is attributed to the Purcell effect.

Suggestions for future work

From the results obtained in the current study we managed to obtain new research directions to be continued in future. In the current study Chemical bath deposition (CBD) method showed outstanding results and it is found to be a structure directing technique, thus the future approach is on optimizing properties of ZnO by doping with transition and rear earth metals. It is clear that different morphological structures of ZnO can be obtained using different preparation methods. Thus, research should be conducted to compare different methods of preparation in order to find out which is the most effective and capable of

reproducing desired morphology over large scale. The investigation might also include the ways on how to control the agglomeration of the ZnO nanoparticles. The study could also be extended by incorporating ZnO nanoparticles into polymer nano-composites. This would assist in clarifying whether the polymers can play major role in preventing ZnO from ageing. Lastly, it would be ideal to improve the luminescence properties of ZnO by doping and co-doping with metals and lanthanides for improvement of white light emission.

Publications

1. Molefe F.V, Koao L.F, Dejene B.F, Swart H.C **Phase formation of Hexagonal wurtzite ZnO through decomposition of $Zn(OH)_2$ at various reaction temperatures using CBD method** *Optical materials* (Accepted)
2. Molefe F.V, Koao L.F, Dejene B.F, Swart H.C. **Influence of zinc acetate concentration in the preparation of ZnO nanoparticles via chemical bath deposition** Proceedings of SAIP ISBN: 978-0-620-65391-6 (2015) 79 – 84
3. F.V. Molefe, L.F. Koao, J.J. Dolo, B.F. Dejene. **Effect of reaction time on structural, morphology and optical properties of ZnO nanoflakes prepared by chemical bath deposition method** *Physica B.* **439** (2014) 185 – 188
4. Molefe F.V, Koao L.F, Dejene B.F, Swart H.C **The influence of annealing temperature on luminescence properties of ZnO nanopowders prepared by chemical bath deposition method** *Journal of surface Science* (Submitted)

Research presentations

Articles in this thesis were presented in national and international conferences as listed below.

1. Molefe F.V, Koao L.F, Dejene B.F, Swart H.C. **Influence of zinc acetate concentration in the preparation of ZnO nanoparticles via chemical bath deposition** 59th Annual Conference of the SAIP University of Johannesburg, 7-11 July 2014 (National Conference).

2. F.V. Molefe, L.F. Koao, J.J. Dolo, B.F. Dejene. **Effect of reaction time on structural, morphology and optical properties of ZnO nanoflakes prepared by chemical bath deposition method** *Physica B.* **439** (2014) 185 – 188 5th South African Conference on Photonic Materials (SACMP 2013), Kariega, South Africa, 2013 (International conference)